



Università degli Studi di Catania
Dipartimento di Matematica e Informatica

Dottorato di Ricerca in
Matematica per la Tecnologia - XXIII ciclo

Central Weighted Non-Oscillatory (CWENO) and Operator Splitting Schemes in Computational Astrophysics

STAVRO L. IVANOVSKI

Coordinator

Prof. GIOVANNI RUSSO

Supervisors

Prof. GIOVANNI RUSSO

Dr. ALFIO BONANNO

Settore Scientifico Disciplinare MAT/08

December 2010

*In memory of my father
Lambro Ivanovski*

*I believe in Humanity,
It is a big act of Faith...
I believe in Science,
It is a big act of Hope.*

S.I.

Abstract

High-resolution shock-capturing schemes (HRSC) are known to be the most adequate and advanced technique used for numerical approximation to the solution of hyperbolic systems of conservation laws. Since most of the astrophysical phenomena can be described by means of system of (M)HD conservation equations, finding most accurate, computationally not expensive and robust numerical approaches for their solution is a task of great importance for numerical astrophysics. Based on the Central Weighted Non-Oscillatory (CWENO) reconstruction approach, which relies on the adaptive choice of the smoothest stencil for resolving strong shocks and discontinuities in central framework on staggered grid, we present a new algorithm for systems of conservation laws using the key idea of evolving the intermediate stages in the Runge Kutta time discretization in primitive variables. In this thesis, we introduce a new so-called conservative-primitive variables strategy (CPVS) by integrating the latter into the earlier proposed Central Runge Kutta schemes (Pareschi et al., 2005). The advantages of the new shock-capturing algorithm with respect to the state-of-the-art HRSC schemes used in astrophysics like upwind Godunov-type schemes can be summarized as follows: (i) Riemann-solver-free central approach; (ii) favoring dissipation (especially needed for multidimensional applications in astrophysics) owing to the diffusivity coming from the design of the scheme; (iii) high accuracy and speed of the method. The latter stems from the fact that the advancing in time in the predictor step does not need inversion between the primitive and conservative variables and is essential in applications where the conservative variables are neither trivial to compute nor to invert in the set of primitive ones as it is in relativistic hydrodynamics.

The main objective of the research adopted in the thesis is to outline the promising application of the CWENO (with CPVS) in the problems of the computational astrophysics. We tested the method for one dimensional Euler hydrodynamics equations and we assessed the advantages against the operator splitting and finite-volume

Godunov-type approaches implemented in the widely used astrophysical codes ZEUS-MP/2 (Stone and Norman, 1992) and ATHENA (Stone et al., 2008), respectively. We extended the application of the scheme to one dimensional relativistic hydrodynamics (RHD), which (to the author’s knowledge) is the first successful attempt to approximate the special relativistic hydrodynamics with CWENO method. We demonstrate that strong discontinuities can be captured within two numerical zones and prevent the onset of numerical oscillations.

In the second part of the present thesis, the astrophysical operator-splitting MHD code ZEUS-MP/2 has been used to perform three dimensional nonlinear simulations of MHD instabilities. First, we present global 3D nonlinear simulations of the Tayler instability in the presence of vertical fields. The initial configuration is in equilibrium, which is achieved by balancing a pressure gradient with the Lorentz force. The nonlinear evolution of the system leads to stable equilibrium with current free toroidal field. We find that the presence of a vertical poloidal field stabilizes the system in the range from $B_\phi \approx B_z$ to higher values of B_z (Ivanovski and Bonanno, 2009). Second, the dynamics of the expansion of two colliding plasma plumes in ambient gas has been investigated via hydrodynamical simulations. Experimental observations of a single plume, generated by high power pulsed laser ablation of a solid target in ambient gas with pressure of about 10^{-1} Torr, show possible Rayleigh-Taylor (RT) instability. Our numerical simulations with two plumes show RT instability even in low pressure gas, where single-plume expansion cannot cause instability. In addition, we find that the RT instability is developed for about ten nanoseconds, while the instability in the case of a single plume typically takes thousand of nanoseconds. We show that the theoretically derived density condition for stability, $\rho_{plume} < \rho_{gas}$, is satisfied in all our simulations (Ivanovski et al., 2010).

In the present thesis, we confirm the promising behavior of the conservative-primitive variables strategy with CWENO approach in computational astrophysics. We demonstrated high accuracy and robustness of the method in the essential one dimensional applications, sod-shock tubes and slow-moving shocks. Extending the method to higher dimensions and using the knowledge accumulated by means of direct numerical operator splitting simulations of MHD instabilities motivates building a modern accurate astrophysical code which will be able to resolve a wide range of problems, from ideal (magneto)hydrodynamics to relativistic (magneto)hydrodynamics.

List of Figures

| | | |
|------|--|----|
| 2.1 | Reconstruction and projection | 16 |
| 2.2 | Accuracy constants | 24 |
| 2.3 | Burgers equation and its weights with CRK4 | 32 |
| 2.4 | Sod's Problem. Componentwise application | 35 |
| 2.5 | Sod's problem. Global Smoothness Indicators | 36 |
| 2.6 | Lax's problem. Global Smoothness Indicators | 38 |
| 2.7 | Lax's problem. Projection along the characteristics | 41 |
| 2.8 | Conservative-primitive variables strategy. Sod's problem | 47 |
| 2.9 | ZEUS-MP/2 and CRK4-CPVS numerical tests | 52 |
| 2.10 | Specific energy with ZEUS-MP/2 and CRK4-CPVS | 54 |
| 2.11 | Slow-moving shock with ATHENA and CRK4-CPVS. | 57 |
| 2.12 | Sjögreen problem with ATHENA and CRK4-CPVS | 58 |
| | | |
| 3.1 | Spectral decomposition in RHD | 70 |
| 3.2 | Relativistic shock tube. Density and pressure profiles. FOFV | 72 |
| 3.3 | Relativistic shock tube. Velocity and energy profiles. FOFV | 73 |
| 3.4 | Density and pressure profiles. CRK4-CPVS. 400 cells | 74 |
| 3.5 | Velocity and specific internal energy profiles. CRK4-CPVS. 400 cells . . | 75 |
| 3.6 | Density and pressure profiles. CRK4-CPVS. 800 cells | 76 |
| 3.7 | Velocity and specific internal energy profiles. CRK4-CPVS. 800 cells . . | 77 |
| | | |
| 4.1 | CentaurusA | 83 |
| 4.2 | Cartoon of formation of extragalactic jet | 84 |
| 4.3 | Onset of MHD instability | 87 |
| 4.4 | Toroidal and poloidal magnetic configuration | 88 |

LIST OF FIGURES

| | | |
|------|--|-----|
| 4.5 | Spectrum of the radial magnetic field | 89 |
| 4.6 | Density, toroidal field and final state | 90 |
| 4.7 | The growth rate of velocity and magnetic field | 92 |
| 4.8 | Pure toroidal field case. Vertical cut | 93 |
| 4.9 | Pure toroidal field case. Azimuthal direction cut | 94 |
| 4.10 | Weak poloidal field case. Vertical cut | 95 |
| 4.11 | Weak poloidal field case. Azimuthal direction cut | 96 |
| 4.12 | Strong poloidal field case. Vertical cut | 97 |
| 4.13 | Strong poloidal field case. Azimuthal direction cut | 98 |
| | | |
| 5.1 | Plumes model representation | 102 |
| 5.2 | Seed plasmas and the stagnation layer | 103 |
| 5.3 | Rayleigh-Taylor instability of colliding plumes | 107 |
| 5.4 | Volume rendering of the density of two colliding plumes | 108 |
| 5.5 | Volume rendering of the energy of two colliding plumes | 109 |
| 5.6 | Energy and density of two colliding plumes at time 50 ns | 111 |

List of Tables

| | | |
|-----|---|-----|
| 2.1 | Convergence tests with CRK4 | 31 |
| 4.1 | The growth time for velocity and magnetic field | 91 |
| 4.2 | The growth time for velocity and magnetic field | 91 |
| 5.1 | Numerical simulations of colliding plumes | 106 |

LIST OF TABLES

Chapter 1

Introduction

The ephemeral nature and composite structure of the very fast physical events occurring in the astronomical systems make the universe perfect numerical (magneto) hydrodynamics laboratory. Because of the huge diversity of the timescales in the astrophysical phenomena their evolution is barely observable. Therefore, the astrophysicists must develop models, based on physical assumptions, in order to discover the mechanism, which possibly drives the astrophysical phenomena. Typically, a quality model and its predictions appear as a key tool of understanding the physics of our universe. Then, the more the model is accurate and reflects the complex features of the astrophysical bodies, the better description and true explanation of the sophisticated nature of the astrophysical systems. Developing high resolution numerical approaches, which are able to capture every single aspect in the multi-staged evolution in any astronomical event appears a necessary and essential problem of the computational astrophysics nowadays.

Improvement in the instrumentation, as the wavelength coverage, spatial resolution and sensitivity has been accumulated. Not only can we determine velocities and observe structures, but also the resolution of spacecraft, like Hubble Space Telescope, the X-ray Chandra, the infrared Spitzer, etc. have made it possible to obtain resolutions of order a few kilometers per second for the entire satellite ultraviolet. These new powerful observational facilities have had more than an adequate response from the achievements in the computational capabilities. Publicly available MHD and radiative codes have highly advanced the scientific research in astrophysics. Modern high-resolution shock-capturing algorithms permit modeling of more complex problems, which were thought of being non resolvable for more than two decades. The processor speed has increased

1. INTRODUCTION

and memory has expanded encouraging the scientists to look for better numerical approximations to the outstanding and forthcoming open issues in astrophysics.

The new modern high-resolution shock-capturing schemes are presented in the computational astrophysics from a relatively short time. Since most of the physics of the astronomical systems can be described through the hyperbolic systems of conservation laws, the task of finding a well-approximated numerical solution to such systems is of great importance. The recent high-resolution astrophysical codes examples of which include the new NIRVANA (Ziegler, 2004), versatile advection code (VAC) (Toth, 1996), FLASH (Fryxell et al., 2000), PLUTO (Mignone et al., 2007), BATS-R-US (Powell et al., 1999) and ATHENA (Stone et al., 2008) are based on finite-volume Godunov-type schemes. ZEUS-MP/2 (Stone and Norman, 1992) is one of the most used ideal MHD astrophysical codes based on operator splitting of the equations, with higher-order upwind methods used for the advection terms, centered-differencing for the remaining terms, and artificial viscosity for shock capturing. The operator splitting technique can be summarized as follows. If we consider a partial differential equation,

$$\frac{dx}{dt} = f(x),$$

whose operator, $f(x)$, can be split into parts, $f(x) = D_1(x) + D_2(x) + D_2(x) + \dots$, then each part may be approximated by the preceding term in the splitting, i. e.

$$\begin{aligned}\frac{x^1 - x^0}{dt} &= D_1(x^0), \\ \frac{x^2 - x^1}{dt} &= D_2(x^1), \\ \frac{x^3 - x^2}{dt} &= D_3(x^2) \dots\end{aligned}$$

where D_i are the finite difference equations of the operators x_i . In ZEUS-MP/2 the 'parts' are divided into two steps, the 'source step', which deals with the density and energy and the 'transport' step, which deals with the fluid advection by effectively moving the density, momentum and internal energy across zone boundaries (Stone and Norman, 1992a). Operator splitting methods might lead to errors during the advection step. The difficulty is in constructing an accurate interpolation algorithm to calculate the interpolated value of a quantity or flux at the control volume faces (ZEUS family of codes use staggered grid, i.e. some variables are located at the center of the cell, while the others on the cell edges). By construction, the rate of change of a quantity or flux

in a cell volume is equal to the divergence of the variable through the cell surfaces. The requirements for the interpolation ensuring stability and accuracy include monotonicity (no extrema in the flow), upwinding (to preserve positivity) and being centered in time (to reduce diffusion and preserve accuracy). The operator splitting methods do not solve the dynamical equations in conservation form, and hence codes as ZEUS are inappropriate for use with Adaptive Mesh Refinement (AMR), a technique which matches the advances in the computational facilities and resolves problems of a wide range in length scales. The reason is that operator splitting uses non-conservative form, but in order to prevent spurious reflections, it is important to enforce conservation at internal boundaries between fine and coarse meshes.

Finite-volume schemes do not separate different directions into different steps as it is done in operator splitting methods. The result is a very physical one since each cell in the grid is a control volume, in which the integral form of the conservation laws hold. Consequently, the time rate of change of the average density, for example, in the cell is expressed in terms of flux of density through the faces of the cell. Therefore, the quality of the solution strongly depends on the level of approximation used to compute the fluxes across cell boundaries. In the finite volume approach a coupled system of conservation laws is written in the form

$$\frac{\partial \vec{U}}{\partial t} + \nabla \cdot \vec{F} = 0,$$

where \vec{U} is the vector of conserved quantities and \vec{F} is the flux. Then the computational domain is divided into 'cells' and the the system of the partial differential equations is integrated over each cell in the resulting grid. High resolution upwind schemes are based on the following ingredients: Godunov idea of using the solution to Riemann's initial value problem as a keystone for a first-order numerical method, nonlinearity of the scheme for a higher order introduced by van Leer's and the 'approximate Riemann solvers' approach, proposed by P. Roe, van Leer and S. Osher. Very successful schemes called upwind are based on an update step in which the data is biased toward the upwind direction. The simplest upwind scheme for

$$\frac{\partial u}{\partial t} + a \frac{\partial u}{\partial x} = 0$$

is

$$\frac{u_j^{n+1} - u_j^n}{\Delta t} = \begin{cases} -a \frac{u_j^n - u_{j-1}^n}{\Delta x} & a > 0 \\ -a \frac{u_{j+1}^n - u_j^n}{\Delta x} & a < 0 \end{cases}$$

1. INTRODUCTION

where j and n are the discrete spatial index and discrete temporal index, respectively. The upwinding approach needs some type of characteristic decomposition to determine which way is upwind for each of the waves in the system of conservation laws. Furthermore, it needs a construction of an interface flux based on this characteristic decomposition, using upwind biased data. The characteristic decomposition ensures stability of the scheme, while the characteristic flux construction ensures that the scheme is conservative. The methods in which are used symmetric-centered differences lead to numerical unstable schemes. Before the upwinding approach has been introduced researchers used schemes as Lax-Friedrichs which is very dissipative, or Lax- Wendorff, which is less dissipative but could not capture even weakly discontinuous solutions. The central first-order finite volume scheme can be considered as Lax-Friedrichs and hence is very diffusive. We construct higher order scheme based on Central Weighted Non-Oscillatory idea. Finite volume scheme are based on interpolations of discrete data using polynomials or other simple functions. Traditionally, the finite volume scheme are based on fixed stencil interpolations. It works fine for globally smooth problems, but fixed stencil interpolation of second or higher order accuracy is necessarily oscillatory near a discontinuity. The oscillations do not decay in magnitude when the mesh is refined. Operator splitting finite difference methods avoid the oscillations by adding artificial viscosity. The latter could be large enough near the discontinuity to suppress the oscillations, but small elsewhere to maintain the high-order accuracy. A drawback of using artificial viscosity is that it is problem dependent. The ENO idea was proposed for piecewise smooth functions. Harten, Engquist, Osher and Chakravarthy proposed a hierarchy, that begins with one or two cells, then adds one cell at a time to the stencil in dependence on the Newton divided differences. Thus, ENO schemes are uniformly high accurate and resolve shocks with sharp and monotone transitions. Weighted ENO (WENO) schemes were developed, using a convex combination of all candidate stencil instead of just one (ENO). Central WENO is WENO applied in the central framework. CWENO approach and its Central Runge Kutta application are discussed in the introduction of the first chapter of the thesis.

A new idea in constructing CRK schemes and their application to a system of relativistic hydrodynamics is one of the main objectives in this thesis. The key point is calculating all intermediate stages in Runge-Kutta predictor step in primitive variables and through mapping to calculate the final conservative variables on the staggered grid.

To the author's knowledge, such attempt will be the first reported in the field of central schemes applied to the system of conservation laws. This modification in the algorithm of the CRK schemes improves sufficiently the cost and the accuracy of the schemes.

1.1 Relativistic hydrodynamics context

Relativistic hydrodynamics is an important topic of modern astrophysics in at least three contexts. First context concerns jets emerging at relativistic speed from the core of active galactic nuclei or from microquasars. Second one concerns compact stars and flows around black holes and the third consider cosmology. Special relativity is sufficient for the first astrophysical context, whereas the general relativity is necessary to describe the second and the third one. High velocity outflows can be found in the galactic jets, binary neutron stars or binary white dwarfs. In the galactic jets the material reaches ultrarelativistic regime (Lorentz factor is approximately equal to 10). In the theoretical models for type-II supernovae, the early mechanism of hydrodynamical bounce implies a strong shock wave. To discover the conditions, which trigger the formation of shock and the strength of formed shock is one of the essential numerical problems which one encounters working in this field. The relativistic shocks are a very important phenomena in several fields in physics. Apart from the astrophysics, the relativistic shocks are believed to be common phenomena in plasma physics (fast magnetoacoustic shock waves are achieved in laboratory) and nuclear physics (in collisions among heavy ions). We address the capturing of the strong relativistic shocks through a new algorithm based on CWENO which solve the relativistic hydrodynamic equations accurately. The key advantage is that the evolution in time has been made in primitive variables. The latter is crucial in the case of relativistic approach owing to that the inversion between the conservative variables and primitive variables requires solution of a non-linear equation for one of the primitive variables.

1.2 Objective and structure of the thesis

The main objective of investigation in the thesis is to contribute the field of modern high-resolution shock-capturing schemes used to resolve strong shocks in relativistic hydrodynamics. The CWENO approach shows excellent shock capturing properties,

1. INTRODUCTION

stability and accuracy. One distinct advantage of a new proposed conservative-primitive variables strategy is in its accuracy, robustness and convergence speed in applications where the mapping between the conservative and primitive variables is not trivial. For example, the inversion of the variables in relativistic hydrodynamics needs solving a nonlinear quartic equation of one of the primitive variables (in our case pressure). The second objective of investigation in the thesis concerns nonlinear three dimensional (M)HD instabilities in two different astrophysical scenarios. The numerical simulations of stability properties of toroidal and poloidal magnetic field configuration by means of Tayler instability have been performed. The second astrophysical scenario considers the physical problem of two colliding plasma plumes. Understanding the conditions under which Rayleigh-Taylor instability is triggered and sustained is the research aim of the second group of hydrodynamical three-dimensional simulations.

Structure of the Thesis

Chapter 2 is devoted to the CWENO approach. It examines the basic CWENO reconstruction Levy et al. (1999) and CRK schemes Pareschi et al. (2005). It includes the new CWENO algorithm with conservative-primitive variables strategy. The numerical results for comparison between the operator splitting schemes (ZEUS-MP/2) and CWENO(CRK4-CPVS) are introduced in the end of the same chapter. In the end, the numerical results obtained by finite-volume Godunov-type ATHENA are compared with CWENO approach. Chapter 3 addresses the application of the fourth-order CRK scheme with conservative-primitive variables strategy to special relativistic hydrodynamics, including the benchmark sod shock tube tests. Chapter 4 deals with stability properties of magnetic configuration of toroidal and poloidal field by means of three dimensional nonlinear ideal MHD simulations. Chapter 5 treats the plasma physics problem of Rayleigh-Taylor instability of two colliding plasma plumes. The thesis ends with 6 where we sum up the numerical results of the thesis.

Chapter 2

Shock capturing central WENO (CWENO) schemes for hyperbolic systems of conservation laws

2.1 Introduction

Modern high-resolution methods were originally developed for nonlinear problems in order to accurately capture discontinuous solutions such as shock waves. Shock-capturing methods as a class of high-resolution techniques for computing sharp, discontinuous changes in flow variables appear sufficient tool to approximate solutions of the hyperbolic systems of conservation laws, which is the base of the computational fluid dynamics nowadays. Developing and implementing the shock capturing schemes is very active field of research in more than two decades. Both mathematical and applicational motivation drives these efforts. Solutions of conservation laws may develop finite-time jump discontinuities. To obtain convergent numerical approximations of such solutions is not a trivial task. The formulation of hyperbolic equations through conservation laws is crucial for finding the correct solution if a shock wave is presented in the flow. If the conservative method, i.e. a method in which the equations are written in a conservative form, is convergent, the conservative scheme do converge to one of the *weak solution* of the original system of equations (*Lax-Wendorff theorem*, (Lax

2. CWENO SCHEMES FOR SYSTEMS OF CONSERVATION LAWS

and Wendroff, 1960)). Another motivation is the large number of applications of the shock capturing scheme, for example, the complex flows in (relativistic) gas dynamics and turbulence interaction require efficient schemes, which have the quality to resolve the complex geometry accurately. A review of such numerical methods can be found, for example, in (E.Godlewski and P.-A.Raviart, 1996; LeVeque, 1992; Tadmor, 1997).

Finite difference and finite volumes methods follow two different approaches of discretization of the hyperbolic partial differential equations. Finite difference schemes, in which derivatives are approximated by finite differences could fail near the discontinuities in the solution where the differential equation does not hold. Thus, finite difference can be used only on smoothly varying or on uniform mesh. The basic unknown is the point-wise value of the function and in case of *upwind*-type differencing schemes discretization of the hyperbolic partial differential equations is made by using differencing biased in the direction determined by the sign of the characteristic speeds. In contrast, for finite volume schemes, the conservation laws are integrated in space over each grid cell of the domain, i.e. the equation is transformed of an evolution equation for the cell averages of solution, divided by the volume of the cell. Thus, the basic unknowns are the cell average values, which are modified in each time step by the flux through the edges of the grid cell, and the primary task is in the choice of the proper *numerical flux functions* which correctly approximate the flux. This can be achieved either by evaluation of known numerical flux functions, for example, Godunov, Engquist-Osher or Lax-Friedrichs flux, (Russo, 2008) or by evaluation of *numerical flux functions* at the edge of each cell through extracting information on point values from the knowledge of the cell averages. The latter work is assigned to reconstruction algorithms. Their crucial role is in the precise calculation of the pointwise value of the solution as a function of position, at a given time, using the only data available - the cell average values.

The integration of the conservation laws has initially been introduced by the *upwind* approach. This approach generalize the first-order *upwind Godunov scheme* in which piecewise-constant interpolation evolves exactly the conservation law to the next time step. The numerical flux function is seen to be an approximation to the time-averaged flux across the interface and the flux integral depends on the solution at the numerical interfaces during the time step. Hence, a solution of the *Riemann problem* on the boundaries of each cell is necessary to compute the solution at the numerical interfaces. Such a procedure is considered as *upwinding*, since the difference between the right and

left direction of the outgoing waves should be counted in order to compute the flux in these non-smooth regions. Note that, for nonlinear systems, a general scheme of such type, which requires the (exact or approximate) solution of the Riemann problem is not known, so this may make the use of upwind approach cost and complicated.

To achieve higher accuracy in space with upwind schemes, one must use high order reconstruction of the field variables. Higher order approximation of the field at given time can be obtained by using piecewise polynomial instead of a piecewise constant. A piecewise polynomial reconstruction of degree r should provide spatial accuracy of order $r+1$ in the smooth regions. The wider the stencil, the higher the order of accuracy of the interpolation if the interpolated function is smooth inside the stencil. On the other hand, even a wide stencil but fixed might create oscillations near a discontinuity (Shu, 1998). Such oscillations, called Gibbs phenomena in spectral methods, do not decay in magnitude in a refined mesh and often leads to numerical instability in nonlinear problems containing discontinuities. *ENO (Essentially Non-Oscillatory)* schemes were proposed by (Harten et al., 1987) with the following features: uniformly high order accurate, no mesh size dependent and essentially non-oscillatory interpolation (i.e. the magnitude of the oscillations decays as $O(\Delta x^k)$, where k is the order of accuracy) for piecewise smooth functions. The ENO idea is based on a stencil selection in each cell of the grid, which automatically avoid crossing the discontinuities in the interpolation procedure as much as possible, hence minimizing the spurious oscillations which might appear.

In the *Weighted Essentially Non-Oscillatory (WENO)* reconstruction, suggested in (Liu et al., 1994), a convex combination of all candidate stencils (instead of just one as in the original ENO) is used. The weights of this combination are computed through non-linear procedure based on the local smoothness of the stencil. The advantage of WENO philosophy is in the 'adaptivity' of the stencil, since every stencil is weighted according to the oscillations it might create. Moreover, in smooth regions the linear combination of the different stencils can be considered as a wide stencil, and a higher-order scheme can be constructed without using polynomials of a higher degree in the reconstruction procedure. In discontinuous regions, the weights will favor the stencils in the smoother regions. WENO approach turned to be very efficient in preserving high accuracy of approximation and expanded the area of its applications (see Shu (1998),

2. CWENO SCHEMES FOR SYSTEMS OF CONSERVATION LAWS

and the references therein). The local smoothness criterion of the stencils is presented in (Jiang and Shu, 1996).

In this thesis, the focus is on the construction of high order shock capturing scheme based on the *central* differencing combined with WENO reconstruction. This class of so called *Central WENO schemes* has two main ingredients included: a WENO reconstruction of pointwise values from their given cell averages and central differencing based on a staggered evolution of the reconstructed averages. Naturally, the *central* approach is constructed by using a staggered mesh, but staggering can be avoided by constructing a non-staggered version without losing accuracy in the approximation. Such study is presented in (Jiang et al., 1998). Non-staggered central schemes resemble non-staggered finite volume schemes with local Lax-Friedrichs numerical flux function included (Kurganov and Tadmor, 2000). The origin of such similarity can be searched in the prototype scheme for the *central* approach, namely, first-order Lax-Friedrichs scheme (Friedrichs and Lax, 1971). In its staggered version, the Lax-Friedrichs scheme is a piecewise-constant reconstruction evolved exactly in time and projected on its staggered cell-averages. It is worth noting that the staggering makes the time-update of the approximation of the fluxes to happen in the smooth regions, limited by an appropriate *CFL condition*. Thus, the field-by-field characteristic decomposition part of the Godunov-type upwind scheme is not needed and is replaced by straightforward centered computation of the considered quantities. Hence, no Riemann solvers are required, a quality which is highly evaluated and beneficial, especially in multidimensional problems where no such Riemann-solvers exist. On the other hand, the staggering suffers from excessive numerical dissipation, which favors the use of the less dissipative upwind-based schemes of the same order, but in general is in advantage compared with the corresponding more dissipative non staggered finite volume scheme applied with local Lax-Friedrichs flux. A way to circumvent the excessive dissipation is by using modern, high-resolution, non-oscillatory reconstructions. The study of achieving higher accuracy has began with a higher-order reconstruction and a sufficient accurate quadrature rule for the approximation of the fluxes. The one-dimensional second-order Nessyahu-Tadmor scheme (Nessyahu and Tadmor, 1990) and Sander-Weiser (Sanders and Weiser, 1992)(characteristic tracing) scheme are of the basic works on central approach. In these central schemes, the conservation law is integrated in time and space

on control volumes which are staggered with respect to the cells on which the central averages are performed. Thus, the discontinuities in the reconstructed pointwise solution are center-located and the solution itself remains smooth at the edges of the staggered control volumes. As a result, the method permits a simple construction of the numerical fluxes.

This chapter follows the approach presented in (Levy et al., 1999) and (Pareschi et al., 2005) for constructing high order central schemes. The authors present novel high order reconstructions obtained by WENO technique applied to central schemes. In the first paper, the computation of the integral of the flux on the border of the cell is obtained by using a suitable quadrature formula and the field value at the nodes of the quadrature formula are obtained by using Runge-Kutta method. In the second paper, the emphasize is on the construction of *Central-Runge Kutta schemes* (CRK), which are based on the combination of pointwise computation of the stage values in the Runge-Kutta time discretization at the edge of the cell, followed by computation of the final value of the staggered cell average through a conservative scheme in the framework of cell averages evolution on staggered cells. The CRK schemes are reported of being high efficient and simple and have a quality that there is no need to use a quadrature rule in time for the fluxes. In addition, such a technique enables construction of schemes of any order of accuracy.

Although the CWENO schemes exhibit the best properties of both approaches: on one hand, the simplicity, robustness and Riemann-solver-free approximation thanks to the central formulation, and on the other hand, high-order accuracy due to the non-oscillatory reconstruction, there is still room for improving the efficiency, especially in the application to the system of hyperbolic equations where the well-known *componentwise* approach offers remarkable advantage over the corresponding upwind framework. Not only the natural extension of *Global Smoothness Indicators* in the WENO approximation, i. e. a weighted average of the *Smoothness Indicators* given by each component, but also the projection along the characteristic direction technique in CWENO method seem to be efficient in bypassing the excess of dissipation and the spurious oscillations which might appear in the approximation of the hyperbolic systems (see Pareschi et al. (2005)). The projection along the characteristics is foreign to the central scheme philosophy, because it damages the black-box property of the schemes, i.e. that such schemes can be implemented with a very little knowledge of

2. CWENO SCHEMES FOR SYSTEMS OF CONSERVATION LAWS

the structure of the system of conservation laws. Nevertheless, as we can see from the numerical experiments, applying the characteristic projection to CWENO sufficiently decrease the spurious oscillations. Details on the improvements, when one uses the global smoothness indicators and projection along the characteristics techniques will be discussed in the section 2.6 below.

The *Euler equations*, i.e. the system of inviscid conservation laws, are first-order system of non-linear coupled equations. Since the physical content of the Euler equations is expressed by the conservation laws for mass, momentum and energy, the basic formulation is derived from the integral form of this conservation laws. The vectors of variables formed by density, momentum and total energy, obeying the conservation form of the equations are called *conservative variables*. However, the set of variables, which can be directly controlled experimentally are density, velocity and pressure. These variables can generally be imposed directly by the physical boundary conditions and are called the *primitive variables*. In addition, since the system of Euler equations is hyperbolic in time, quantities that propagate along the characteristics can be defined and the system can be written in so called *characteristic variables*.

Implementing and testing a new idea of the construction of CRK scheme in its application to a system of hyperbolic system is one of the main objectives of this thesis. The key point is in calculating all intermediate stages of Runge-Kutta evolution in primitive variables and through mapping to calculate the final value of the staggered cell average with the corresponding conservative variables in the conservative scheme. To the author's knowledge, such attempt will be the first reported in the field of central schemes applied to system of conservation laws. This modification in the algorithm of the CRK schemes should improve sufficiently the cost and the accuracy of the schemes. In fact, the numerical experiments in this thesis justifies the expected improvement of such approximation.

The chapter is organized as follows. In the next section, a short overview on central schemes for one- dimensional hyperbolic systems of conservation laws is presented. Then the section is completed with the basic knowledge for the time evolution of the approximation to the hyperbolic systems in the Runge-Kutta framework. The central WENO (CWENO)reconstruction algorithm, suggested in (Levy et al., 1999), is shown in Section 2.3. The latter ends with the construction of higher order CRK schemes.

2.2 Central Schemes with Runge-Kutta time evolution (CRK scheme)

We present numerical results for the scalar equation and for a system (Gas Dynamics) in Sections 2.5 and 2.6, respectively. The improvements of applying the global smoothness indicators and the projection along the characteristics are shown in the gas dynamical case. The algorithm based on the new *conservative-primitive variables* concept is described in the same section. The chapter ends with a comparison between shock-capturing CRK schemes and the operator-splitting schemes or with Godunov-type schemes which have been implemented in established astrophysical codes, for example, in ZEUSMP2 (Stone and Norman, 1992) and the finite-volume ATHENA (Stone et al., 2008). The aim of such a comparison is to outline the quality of the proposed one-dimensional schemes in resolving shocks and discontinuities, and to reveal the motivation in expanding our technique to higher dimensions.

This chapter provides the necessary knowledge of applying the CRK to the more complicated hyperbolic systems of equations, for instance, the physical systems as relativistic hydrodynamics or magnetohydrodynamics.

2.2 Central Schemes with Runge-Kutta time evolution (CRK scheme)

We want to solve the hyperbolic system of conservation laws,

$$u_t + f(u)_x = 0, \quad u \in \mathbb{R}^d, d \geq 1, \quad (2.1)$$

with $f: \mathbb{R}^d \rightarrow \mathbb{R}^d$ continuously differentiable. Hence, the Jacobian of f , $\tilde{A}(u) = f'(u)$ has real eigenvalues and a complete set of eigenvectors. Let the system is subject to the initial conditions, $u(x, t = 0) = u_0(x)$. We assume uniform (not necessary for finite volume schemes) mesh widths in space and time, $h := \Delta x$ and Δt , respectively. We denote the spatial grid points by $x_j = j\Delta x$ and the time steps by $t^n = n\Delta t$. The standard mesh ratio is defined by $\lambda := \Delta t/\Delta x$. The quantities that will be used in the numerical approximation are cell averages. Such choice is implied by the specifics of the solution of (2.1), which can develop shocks even for smooth initial data. We introduce the cell averages in the cell $I_j := [x_{j-1/2}, x_{j+1/2}]$ centered around x_j at time t^n , denoted by \bar{u}_j^n , as follows:

$$\bar{u}_j^n = \frac{1}{h} \int_{x_{j-1/2}}^{x_{j+1/2}} u(x, t^n) dx. \quad (2.2)$$

2. CWENO SCHEMES FOR SYSTEMS OF CONSERVATION LAWS

Integrating the conservation law (2.1) on a cell in space-time $I_j \times [t^n, t^{n+1}]$ and dividing by h afterwards, one has

$$\int_{x_{j-1/2}}^{x_{j+1/2}} u(x, t^{n+1}) dx = \int_{x_{j-1/2}}^{x_{j+1/2}} u(x, t^n) dx - \frac{1}{h} \int_{t^n}^{t^{n+1}} (f(u(x_{j+1/2}, t)) - f(u(x_{j-1/2}, t))) dt. \quad (2.3)$$

This (exact) equation gives the evolution in time of the cell averages and suggests the use of numerical scheme of the form:

$$\bar{u}_j^{n+1} = \bar{u}_j^n - \frac{\Delta t}{h} (F_{j+1/2} - F_{j-1/2}), \quad (2.4)$$

where $F_{j+1/2}$ approximates the integral of the flux on the boundary of the cell, is the so called *numerical flux*, and depends on the cell averages of the cell surrounding the point $x_{j+1/2}$. The simplest one has the form $F_{j+1/2} = F(\bar{u}_j, \bar{u}_{j+1})$, with $F(u, u) = f(u)$. Such schemes, called *conservative*, have the property to obey the conservation property at a discrete level, providing the correct propagation speed for the discontinuities. Finite volume schemes are based on the discretization (2.3). Since the numerical flux in these schemes depends on the cell averages, the system (2.3) is a system of ordinary differential equations for the evolution of cell averages. Such system may be solved by a suitable ODE solver, for example a Runge-Kutta method, which retains the accuracy of the spatial discretization (see Shu (1998)). The overview of Runge-Kutta method is presented in the end of this section.

A key step in both upwind and central schemes is the reconstruction procedure. At each step, the solution, i.e. the initial non-averaged data $u^n(x)$, which is needed to evaluate the right hand side of (2.3) is reconstructed from the cell averages \bar{u}^n by computing a piecewise polynomial function of the form:

$$u^n(x) = R(x; \{\bar{u}^n\}) = \sum_j P_j^d(x) \chi_{I_j}(x), \quad (2.5)$$

where $P_j^d(x)$ is polynomial of degree d , and $\chi_{I_j}(x)$ is the characteristic function of the interval I_j .

Now let us use a piecewise polynomial reconstruction to approximate the exact formula derived by the integration of the conservation law (2.1) on *staggered grid*. The

2.2 Central Schemes with Runge-Kutta time evolution (CRK scheme)

exact relation due to the staggering has the form:

$$\int_{x_j}^{x_{j+1}} u(x, t^{n+1}) dx = \int_{x_j}^{x_{j+1}} u(x, t^n) dx - \frac{1}{h} \int_{t^n}^{t^{n+1}} (f(u(x_{j+1}, t)) - f(u(x_j, t))) dt. \quad (2.6)$$

To obtain a numerical scheme from the upper expression (2.6) one has to approximate the staggered cell average at time t^n and time integral of the flux on the border of the cells.

If the reconstruction is done, then the solution is smooth at the center of the cell and its discontinuities are at the edge of the cell. Integrating the conservation law on a staggered cell gives a fan of characteristics propagating from the center of the staggered cell. In addition, the solution on the edge (dashed vertical lines in the Figure 2.1) will remain smooth, provided the fan of the characteristics does not intersect the edge of the cell, i.e. if a suitable CFL condition of the form

$$\Delta t < \frac{\Delta x}{2\rho(\tilde{A})} \quad (2.7)$$

is satisfied. Here, the $\rho(\tilde{A}) = \max_{1 \leq i \leq d} |\lambda_i(\tilde{A})|$ is the spectral radius of the Jacobian matrix of f , $\tilde{A}(u) = f'(u)$, and λ_i is the i -th eigenvalue. The Figure (2.1) shows two features: first, the characteristic fan and the smoothness of the solution on the edges and second, the time evolution on a staggered cell through a piecewise polynomial reconstruction.

The simplest central scheme is obtained by a piecewise constant reconstruction of the function $u^n(x)$, and by using a first order quadrature rule in the evolution of the integrals. It is just Lax-Friedrichs scheme on a staggered grid and has the form:

$$\bar{u}_{j+1/2}^{n+1} = \frac{1}{2}(\bar{u}_j^n + \bar{u}_{j+1}^n) - \lambda(f(\bar{u}_{j+1}^n) - f(\bar{u}_j^n)), \quad (2.8)$$

where $\lambda = \Delta t/\Delta x$ is the mesh ratio. No knowledge is required of the characteristic structure of the system, which makes the Lax-Friedrich scheme simpler to apply in comparison with the upwind-type scheme, but its disadvantage over the upwind one is the excess of the dissipation. In the case of finite volume schemes with Lax-Friedrichs numerical flux included, such drawback can be circumvented for high order schemes and smooth solution.

2. CWENO SCHEMES FOR SYSTEMS OF CONSERVATION LAWS

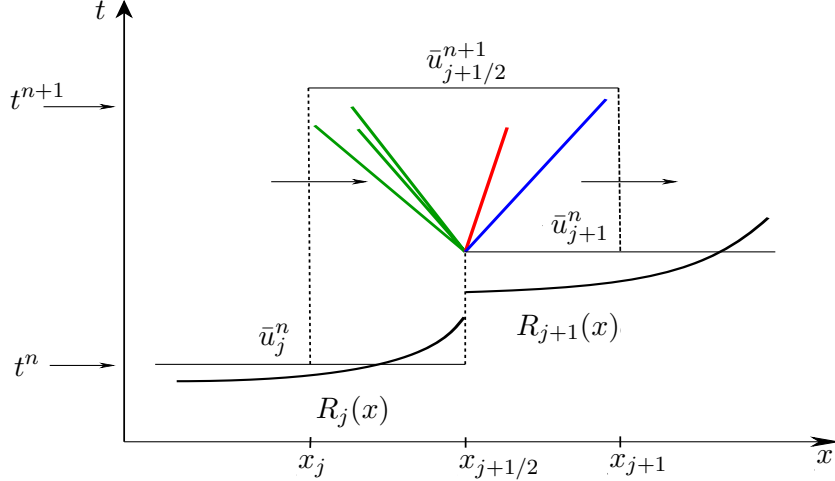


Figure 2.1: Reconstruction and projection. The typical solution to the Riemann problem for the Euler equations: rarefaction(green), contact discontinuity(red) and shock(blue).

Dividing (2.6) on h , one finds the conservation law integrated in space and time on the staggered control volume $V_{j+1/2}^n = [x_j, x_{j+1}] \times [t^n, t^n + \Delta t]$:

$$\bar{u}_{j+1/2}^{n+1} = \bar{u}_{j+1/2}^n - \frac{1}{h} \int_{t^n}^{t^{n+1}} [f(u(x_{j+1}, t)) - f(u(x_j, t))] dt, \quad (2.9)$$

Applying a given reconstruction $P_j^d(x)$, the staggered cell averages at time t^n , $\bar{u}_{j+1/2}^n$, can be explicitly computed by the exact integrals on the RHS of the following relation:

$$\bar{u}_{j+1/2}^n = \frac{1}{h} \int_{x_j}^{x_{j+1}} u^n(x) dx = \frac{1}{h} \int_{x_j}^{x_{j+1/2}} P_j^d(x) dx + \frac{1}{h} \int_{x_{j+1/2}}^{x_{j+1}} P_{j+1}^d(x) dx \quad (2.10)$$

Note that due to the staggering, u is smooth at x_j and x_{j+1} (see the discussion above and Figure 2.1) and therefore the integral in time in (2.6) can be accurately approximated by a quadrature formula for a sufficiently small time step. A prediction on the values of u at the nodes of the quadrature formula can be obtained by integrating the following ODE's system:

$$\left. \frac{du}{dt} \right|_{x_j} = -f(u)_x|_{x_j} \quad (2.11)$$

using the smoothness of u at x_j .

Before we proceed with an overview of Runge-Kutta method, let introduce the second order Nessyahu-Tadmor scheme. The construction of the scheme is based on

2.2 Central Schemes with Runge-Kutta time evolution (CRK scheme)

a piecewise linear reconstruction. A second order quadrature rule (the midpoint rule) is used for the integration of the flux on the edges of the cell. The value of u at the midpoint is computed by first order Taylor expansion. The scheme can be summarized in a predictor-corrector framework as follows:

- **Reconstruction from cell averages**

$$\begin{aligned}\bar{u}_{j+1/2}^n &= \frac{1}{h} \int_{x_j}^{x_{j+1}} u^n(x) dx = \frac{1}{h} \int_{x_j}^{x_{j+1/2}} L_j(x) dx + \frac{1}{h} \int_{x_{j+1/2}}^{x_{j+1}} L_{j+1}(x) dx \\ &= \frac{1}{2}(\bar{u}_j^n + \bar{u}_{j+1}^n) - \frac{1}{8}(u'_{j+1} - u'_j)\end{aligned}\tag{2.12}$$

where $L_j(x) = \bar{u}_j^n + u'_j(x - x_j)/h$ is the linear reconstruction in the cell I_j . Here, the second term on RHS is a first order approximation of the derivative of the function of the cell. Forward Euler scheme, equivalent to a first order Taylor expansion, can be used for computing u at the node of the midpoint rule, $u_j^{n+1/2}$ and yields:

- **Predictor step**

$$u_j^{n+1/2} = \bar{u}_j^n - \frac{\lambda}{2} f(u)'_j\tag{2.13}$$

where $f(u)'_j/h$ denotes a first order approximation of the space derivative of the flux, followed by the second-order

- **Corrector step**

$$\bar{u}_{j+1/2}^{n+1} = \frac{1}{2}(\bar{u}_j^n + \bar{u}_{j+1}^n) - \frac{1}{8}(u'_{j+1} - u'_j) - \lambda[f(u_j^{n+1/2}) - f(u_{j+1}^{n+1/2})].\tag{2.14}$$

A suitable slope limiter has to be used for avoiding onset of spurious oscillations. The simplest one is the MinMod limiter, defined by a MM function in the form:

$$MM\{x_1, x_2, \dots\} = \begin{cases} \min_i\{x_i\} & \text{if } x_i > 0, \forall i \\ \max_i\{x_i\} & \text{if } x_i < 0, \forall i \\ 0 & \text{otherwise} \end{cases}$$

Such limiter, however, degrades the accuracy of the scheme near extrema, because once an extrema cell is detected by the limiter, it sets a zero slope, $u'_j = 0$ in which case the second order scheme is reduced back to standard first-order Lax-Friedrichs one. A Uniform Non Oscillatory (UNO) limiter, proposed by (Harten et al., 1987) maintain

2. CWENO SCHEMES FOR SYSTEMS OF CONSERVATION LAWS

the accuracy of the scheme near the extrema. Later in this section we rewrite the second-order NT scheme in the Central Runge Kutta framework.

Now, we introduce a suitable notation of the Runge Kutta method, convenient for describing the central approach in constructing the CRK schemes(see (Pareschi et al., 2005)). We are concerned with the following initial value problem

$$\begin{cases} y' &= g(y), \\ y(t_0) &= y_0. \end{cases}$$

An explicit Runge-Kutta scheme with ν stages applied to the problem above gives the form:

$$y^{n+1} = y^n + \Delta t \sum_{i=1}^{\nu} b_i K^{(i)}$$

The $K^{(i)}$ are called *Runge-Kutta fluxes* and are defined by:

$$\begin{aligned} K^{(i)} &= g(y^{(i-1)}), & y^{(0)} &= y^n, & i &= 1, \dots, \nu \\ y^{(i)} &= y^n + \Delta t \sum_{l=1}^i a_{i,l} K^{(l)}, & i &= 1, \dots, \nu - 1, \end{aligned}$$

where $y^{(i)}$ are called *intermediate values* and for an explicit scheme are given above. The new key point in the formulation of CRK schemes presented in the thesis is how we calculate these intermediate values. Note, that the RK scheme is uniquely defined by the vector b and the matrix $A = (a_{i,l})$, which is a $\nu - 1 \times \nu - 1$ lower triangular matrix, with non zero elements on the diagonal for explicit schemes. For the fourth-order CRK method, implemented in the thesis, the coefficients are:

$$b = \begin{pmatrix} 1/6 \\ 1/3 \\ 1/3 \\ 1/6 \end{pmatrix}, \quad A = \begin{pmatrix} 0 & 0 & 0 & 0 \\ 1/2 & 0 & 0 & 0 \\ 0 & 1/2 & 0 & 0 \\ 0 & 0 & 1 & 0 \end{pmatrix} \quad (2.15)$$

In the Central Runge Kutta (CRK) schemes, proposed by (Pareschi et al., 2005), the conservation law is integrated on the staggered grid over the interval $I_{j+1/2} = [x_j, x_{j+1}]$ and has the form of the exact equation (2.6). Being discretized in time with Runge Kutta scheme, the updated solution becomes:

$$\bar{u}_{j+1/2}^{n+1} = \bar{u}_{j+1/2}^n - \lambda \sum_{i=1}^{\nu} b_i K_{j+1/2}^{(i)}, \quad (2.16)$$

2.2 Central Schemes with Runge-Kutta time evolution (CRK scheme)

where:

$$K_{j+1/2}^{(i)} = f(u_{j+1}^{(i-1)}) - f(u_j^{(i-1)}), \quad u_j^{(0)} = u^n(x_j) \quad (2.17)$$

Taking into account that the reconstruction $u^n(x)$ is smooth everywhere, but at the cell edges, $x_{j\pm 1/2}$, and therefore, $u(x_j, t)$ remains smooth in the time interval $[t^n, t^{n+1}]$ if the time step is small enough, one can calculate the intermediate states, $u_j^{(i)}$, integrating the conservation law in its differential form, $u_t = -f_x(u)$.

$$u_j^{(i)} = u_j^{(1)} - \Delta t \sum_{l=1}^{i-1} a_{i,l} \hat{K}_j^{(l)}, \quad i = 2, \dots, \nu, \quad (2.18)$$

where the Runge-Kutta fluxes are:

$$\hat{K}_j^{(l)} = -\left. \frac{\partial f(u^{(l)})}{\partial x} \right|_j, \quad u_j^{(1)} = u^n(x_j) \quad l = 2, \dots, \nu. \quad (2.19)$$

If we want to avoid the reconstruction of the fluxes, one can compute them by

$$\frac{\partial f(u)}{\partial x} = \tilde{A}(u) \frac{\partial u}{\partial x},$$

using the reconstruction of the field u to approximate $\partial u / \partial x$. This approach, however, requires the computation of the Jacobian matrix \tilde{A} .

The process, we have just gone through, is the time discretization of the scheme. To discretize in space, we use the reconstruction techniques. From the cell averages $\{\bar{u}_j^n\}$, we compute:

- the staggered cell averages $\{\bar{u}_{j+1/2}^n\}$ in the updated solution (2.16) as it is defined in (2.10).
- the point values $\{u_j^n = u^n(x_j)\}$, which are needed to compute the start-up values $u_j^{(0)}$ in (2.18).

From the intermediate values $\{u_j^{(i)}\}$, we compute the derivative of the fluxes $\{f_x(u^{(i)})|_j\}$, which form the Runge-Kutta fluxes in (2.19). The crucial step in the algorithm is the reconstruction of the cell averages $\{\bar{u}_{j+1/2}^n\}$ (see Pareschi et al. (2005) and the references therein).

For the purposes of this thesis, as a first step, the algorithm of CRK schemes, proposed by (Pareschi et al., 2005), has been implemented. It can be written as a three step method, as follows:

2. CWENO SCHEMES FOR SYSTEMS OF CONSERVATION LAWS

1. Reconstruction step: from the cell averages $\{\bar{u}_j^n\}$, compute the reconstruction point values $u^n(x)$. Once the reconstruction is done, compute the $u_j^{(1)} = u^n(x_j)$ and the staggered cell averages $\{\bar{u}_{j+1/2}^n\}$.
2. Predictor step: Compute the intermediate states (stage values) $\{u_j^{(i)}\}$ from the point values $\{u_j^n = u^n(x_j)\}$:
For $i = 2, \dots, \nu$:
 - Compute $f(u_j^{(i)})$, for $\forall j$;
 - Calculate the Runge-Kutta fluxes, $\hat{K}_j^{(i)} = f_x(u^{(i)})_j$, applying an appropriate non-oscillatory interpolation;
 - Compute $u_j^{(i)} = u_j^{(1)} - \Delta t \sum_{l=1}^{i-1} a_{i,l} \hat{K}_j^{(l)}$;
3. Corrector step: Using the fluxes $K_{j+1/2}^{(i)}$, defined in 2.17, update the numerical solution (the cell averages) on the staggered grid:

$$\bar{u}_{j+1/2}^{n+1} = \bar{u}_{j+1/2}^n - \lambda \sum_{i=1}^{\nu} b_i (f(u_{j+1}^{(i-1)}) - f(u_j^{(i-1)}))$$

Note that, in the corrector step, no additional flux evaluation is needed, i.e. since the $\nu - 1$ of the stage values used in this step have already been computed in the predictor step. Thus, one interpolation less per time step is required, which improves the efficiency of the scheme in the comparison with the previously proposed high order Central WENO scheme (Levy et al., 1999). In the thesis, we introduce even further improvement of the latter technique by calculating the stage values in the primitive variables. Additional improvements, as global smooth indicators and projection along the characteristics increase the accuracy and the efficiency in the performance of the scheme.

This CRK method offers fourth order accuracy of the Central WENO scheme, that we describe in the next sections, when a fourth order RK predictor is used. Such high order schemes provide sharp resolution of the discontinuities and high accuracy of the solution in the smooth regions. However, near the nonlinear discontinuities, these schemes add the right amount of numerical dissipation to counterweight the formation and amplification of spurious oscillations. Although such schemes are more dissipative than the standard Riemann-based schemes, the difference in the capturing

2.3 The Central-WENO (CWENO) Reconstruction

of the shock is sensible in the low (first and second) order schemes, while the difference appears negligible for higher order. In this context, we outline the construction of the higher order CRK scheme, namely, fourth (CRK4) scheme and comment on a third (CRK3) and a fifth (CRK5) schemes. The second order CRK2 schemes are formulated in (Pareschi et al., 2005). The higher order CRK schemes are built with Central WENO reconstructions. The CWENO technique is fundamental for the CRK schemes and it is discussed in detail in the next section.

2.3 The Central-WENO (CWENO) Reconstruction

Levy et al. (1999) proposed Central-WENO(CWENO) reconstruction piecewise-parabolic reconstruction, which was utilized for constructing a fourth-order method. For the aims of this thesis we will take advantage of this CWENO reconstruction and will use it as a skeleton for developing a new improvement to the family of CRK schemes.

Let us assume that the cell averages at time t^n are known. We apply the reconstruction scheme, to obtain the function $R(x; \bar{u}^n)$. By construction, $R(x; \bar{u}^n) = \sum_j R_j(x) \chi_j(x)$, where in this case $R_j(x)$ is a polynomial of degree two. The reconstruction must obey the following properties:

- **Accuracy**

In order to have a high order accurate approximation of the staggered cell averages at time t^n , implying that the polynomial reconstruction must satisfy:

$$\begin{aligned} \frac{1}{2h} \int_{x_{j-1/2}}^{x_j} R(x; \bar{u}^n) dx &= \frac{1}{2h} \int_{x_{j-1/2}}^{x_j} u(x, t^n) dx + O(h^p), \\ \frac{1}{2h} \int_{x_j}^{x_{j+1/2}} R(x; \bar{u}^n) dx &= \frac{1}{2h} \int_{x_j}^{x_{j+1/2}} u(x, t^n) dx + O(h^p), \end{aligned} \tag{2.20}$$

where p is the the spatial order of the method and u is the exact solution at time t^n . Thus we require that the three separate reconstructions, i.e. $R(x_j; \bar{u}^n)$, $\tilde{R}(x_j; \bar{u}^n)$ and $\hat{R}(x_j; \bar{u}^n)$ satisfy the following accuracy:

1. Cell averages

$$\bar{u}_{j+1/2}^n = \frac{1}{h} \int_{x_j}^{x_{j+1}} u(x, t^n) dx + O(h^p), \tag{2.21}$$

2. CWENO SCHEMES FOR SYSTEMS OF CONSERVATION LAWS

2. Pointwise values

$$\tilde{R}(x_j; \bar{u}^n) dx = u(x_j, t^n) dx + O(h^p). \quad (2.22)$$

3. Space derivatives of the flux, $f'(u(x, t))$

$$\hat{R}'(x_j; \bar{f}^n) dx = f'(u(x_j, t^n)) dx + O(h^{p-1}). \quad (2.23)$$

• **Conservation**

$$\frac{1}{h} \int_{I_j} R_j(x) dx = \bar{u}_j. \quad (2.24)$$

- **Non-oscillatory Reconstruction**, i.e. vanishing of the spurious oscillations near the discontinuities in the sense of ENO/WENO reconstruction philosophy.

In every cell, I_j , we shall construct polynomial of degree 2, $P_j(x)$, and let it satisfies the following interpolation requirements:

$$\frac{1}{h} \int_{I_k} P_j(x) dx = \bar{u}_k, \quad k = j - 1, j, j + 1 \quad (2.25)$$

A convex combination of the polynomials $P_{j-1}(x), P_j(x), P_{j+1}(x)$, used in each cell, builds up the reconstruction polynomial:

$$R_j(x) = \omega_{j-1}^j P_{j-1}(x) + \omega_j^j P_j(x) + \omega_{j+1}^j P_{j+1}(x), \quad (2.26)$$

where the weights $\omega_k^j, k = j - 1, j, j + 1$, satisfy $\omega_k^j \geq 0$, and $\sum_{k=j-1}^{j+1} \omega_k^j = 1$.

Each polynomial $P_k, k = j - 1, j, j + 1$, is uniformly third order accurate in the cell j . Thus in any convex combination of these three polynomials we have two more degrees of freedom, which may be used to impose more order conditions. For example, classical WENO schemes are based on imposing fifth order accuracy at the edge of the cell (Jiang and Shu, 1996).

The stencil used in the reconstruction of the second degree polynomial $R_j(x)$ contains five points. In addition, the conservation property (2.24) holds for this convex combination for $R_j(x)$ in I_j , but does not any for other interpolation requirements in the neighboring cells.

Since $deg(P_k(x)) = 2, k = j - 1, j, j + 1$, one can rewrite:

$$P_k(x) = \tilde{u}_k + \tilde{u}'_k(x - x_k) + \frac{1}{2} \tilde{u}''_k(x - x_k)^2, \quad k = j - 1, j, j + 1. \quad (2.27)$$

2.3 The Central-WENO (CWENO) Reconstruction

where $\tilde{u}_k, \tilde{u}'_k, \tilde{u}''_k$ are the reconstructed point values, reconstructed discrete first and second derivatives, respectively. These values are uniquely determined by the interpolation requirements (2.25), as

$$\begin{aligned}\tilde{u}_k &= \bar{u}_k - \frac{\bar{u}_{k-1} - 2\bar{u}_k + \bar{u}_{k+1}}{24}, \\ \tilde{u}'_k &= \frac{\bar{u}_{k+1} - \bar{u}_{k-1}}{2h}, \\ \tilde{u}''_k &= \frac{\bar{u}_{k+1} - 2\bar{u}_k + \bar{u}_{k-1}}{h^2}.\end{aligned}\quad k = j-1, j, j+1 \quad (2.28)$$

For the sake of completeness and make the implementation of the scheme straightforward we rewrite the interpolant $R_j(x)$ considering the relations above:

$$R_j(x) = u_j + u'_j(x - x_j) + \frac{1}{2}u''_j(x - x_j)^2. \quad (2.29)$$

where its reconstructed point values u_j , and its reconstructed derivatives, u'_j, u''_j , are given by

$$\begin{aligned}u_j &= \omega_{j-1}^j(\tilde{u}_{j-1} + h\tilde{u}'_{j-1} + \frac{1}{2}h^2\tilde{u}''_{j-1}) + \omega_j^j\tilde{u}_j + \omega_{j+1}^j(\tilde{u}_{j+1} - h\tilde{u}'_{j+1} + \frac{1}{2}h^2\tilde{u}''_{j+1}), \\ u'_j &= \omega_{j-1}^j(\tilde{u}'_{j-1} + h\tilde{u}''_{j-1}) + \omega_j^j\tilde{u}'_j + \omega_{j+1}^j(\tilde{u}'_{j+1} - h\tilde{u}''_{j+1}), \\ u''_j &= \omega_{j-1}^j\tilde{u}''_{j-1} + \omega_j^j\tilde{u}''_j + \omega_{j+1}^j\tilde{u}''_{j+1}.\end{aligned}\quad (2.30)$$

To complete the reconstruction, we need to determine the weights, ω_k^j , $k = j-1, j, j+1$. Two requirements must hold: (i) maximal accuracy in the smooth regions and (ii) prevent the onset of spurious oscillations. In order to guarantee the convexity, $\sum_{k=j-1}^{j+1} \omega_k^j = 1$, we define the weights as follows:

$$\omega_k^j = \frac{\alpha_k^j}{\alpha_{j-1}^j + \alpha_j^j + \alpha_{j+1}^j}, \quad k = j-1, j, j+1 \quad (2.31)$$

where

$$\alpha_k^j = \frac{C_k}{(\epsilon + IS_k^j)^s}, \quad k = j-1, j, j+1. \quad (2.32)$$

The constants, C_k, ϵ, s will be defined below. Here, IS_k^j are called smoothness indicators and their role is of avoiding automatically the information coming from the non-smooth regions which are the cause of spurious oscillations.

2. CWENO SCHEMES FOR SYSTEMS OF CONSERVATION LAWS

| Scheme | C^{-1} | C^0 | C^{+1} | Accuracy |
|---|----------|-------|----------|----------|
| <i>Reconstruction of $\bar{u}_{j+1/2}^n$</i> | | | | |
| CRK3 | 1/4 | 1/2 | 1/4 | h^3 |
| CRK4 | 3/16 | 5/8 | 3/16 | h^5 |
| CRK5 | 3/16 | 5/8 | 3/16 | h^5 |
| <i>Reconstruction of $u^n(x_j)$</i> | | | | |
| CRK3 | 1/4 | 1/2 | 1/4 | h^3 |
| CRK4 | 3/16 | 5/8 | 3/16 | h^4 |
| CRK5 | -9/80 | 49/40 | -9/80 | h^5 |
| <i>Reconstruction of $f_x(u(x, \cdot)) _{x_j}$</i> | | | | |
| CRK3 | 1/4 | 1/2 | 1/4 | h^2 |
| CRK4 | 1/6 | 2/3 | 1/6 | h^4 |
| CRK5 | 1/6 | 2/3 | 1/6 | h^4 |

Figure 2.2: Accuracy constants. Taken from (Pareschi et al., 2005).

The so-called accuracy constants, C_k introduced here, are computed such that they are symmetric around the center of each cell, which determines the *central* character of the scheme and, hence, the name *Central-WENO* (CWENO) (Levy et al., 1999).

Since the accuracy requirements can not be fulfilled simultaneously, we need to split the computation, which leads to two different sets of constants C_k . Thus, the first set is used in the reconstruction of the cell averages, (2.20), while the second set of constants meets the accuracy requirements in the computation of the flux derivatives (2.37). In order to compute the flux derivatives, we need first to reconstruct pointwise values. Due to the cancellation, any symmetric choice of coefficients will result in a fourth-order approximation of the point- values in the center of the cells ($p = 4$ in (2.22)). In order to achieve higher accuracy $p = 5$ for the reconstructed point values, one has to use non-positive constants, namely a *non-convex* combination of the stencils (see Shi et al. (2002)). In Table 2.2 from the paper of (Pareschi et al., 2005) are summarized the sets of the constants needed for obtaining the desired accuracy. Since in the reconstruction of the pointwise values any symmetric combination of accuracy constants will satisfy the accuracy requirements, the authors have picked the same set used for the reconstruction of the cell averages. In the thesis, the accuracy tests of the improvements of the scheme have been done mostly with the fourth order CWENO (precisely, CRK4) scheme. If one sets the $\alpha_j^k = C_k$, it would result in a linear high order scheme with high accuracy in smooth regions, but with spurious oscillations near the

2.3 The Central-WENO (CWENO) Reconstruction

discontinuities. Here, enters the role of the nonlinear weights. By using the weights, one aims to use only stencils in the reconstruction procedure, which do not contain discontinuity. One weights the stencil by suitable smoothness indicators, which are a quantitative measure of the local roughness of the solution. In order to determine the smoothness indicator, we use the measure proposed by (Jiang and Shu, 1996). IS_j^k is a measure of the regularity of the polynomial P_k on the interval I_j and it is a rescaled measure on the L^2 -norms of the derivatives:

$$IS_k^j = \sum_{l=1}^2 \int_{x_{j-1/2}}^{x_{j+1/2}} h_{2l-1} (P_k(l))^2 dx, \quad k = j-1, j, j+1, \quad (2.33)$$

where $P_k(l)$ denotes the l -th derivative of $P_k(x)$. An explicit integration of (2.33) gives:

$$\begin{aligned} IS_{j-1}^j &= \frac{13}{12} (\bar{u}_{j-2} - 2\bar{u}_{j-1} + \bar{u}_j)^2 + \frac{1}{4} (\bar{u}_{j-2} - 4\bar{u}_{j-1} + 3\bar{u}_j)^2, \\ IS_j^j &= \frac{13}{12} (\bar{u}_{j-1} - 2\bar{u}_j + \bar{u}_{j+1})^2 + \frac{1}{4} (\bar{u}_{j-1} - \bar{u}_{j+1})^2, \\ IS_{j+1}^j &= \frac{13}{12} (\bar{u}_j - 2\bar{u}_{j+1} + \bar{u}_{j+2})^2 + \frac{1}{4} (3\bar{u}_j - 4\bar{u}_{j+1} + \bar{u}_{j+2})^2, \end{aligned} \quad (2.34)$$

In smooth regions, a Taylor expansion of (2.34) is

$$IS_k^j = (\tilde{u}'h)^2 + \frac{13}{12} (\tilde{u}''h^2)^2 + O(h^6), \quad k = j-1, j, j+1, \quad (2.35)$$

Thus, $IS_k^j = O(h^2)$. In non-smooth regions, $IS_k^j = O(1)$, and the normalized weight of the corresponding stencil will be insignificant. Therefore, our reconstruction is in accordance with WENO concept of automatically avoiding the information coming from the non-smooth regions, which is responsible for the onset of spurious oscillations. The parameter ϵ prevents a denominator from vanishing. The empirically selected value ϵ for third order scheme is $\epsilon = 10^{(-4)}$, while $\epsilon = 10^{(-6)}$ is used for the 4-th and 5-th order scheme. The value of ϵ depends on the order of the magnitude of the solution and on the value h . This dependence can be avoid by an appropriate rescaling of the smoothness indicators (see Levy et al. (1999) and therein). We use the parameter $s = 2$, as earlier proposed by the same authors.

To summarize, following Levy et al. (Levy et al., 1999) our reconstruction is a routine which starting from the cell averages values $\{\bar{u}_j\}$ at time t^n , returns as an output the point values u_j, u'_j, u''_j , which completely determine the reconstruction polynomial $R_j(x)$, (2.29).

2. CWENO SCHEMES FOR SYSTEMS OF CONSERVATION LAWS

In order to compute the reconstruction from the point values for the flux $f_j = f(u_j)$, necessary in the intermediate stages in Runge-Kutta step, the candidate polynomials P_{j-1} , P_j , P_{j+1} for each cell must satisfy the following interpolation requirements:

$$P_j(x_k) = f_k, \quad k = j - 1, j, j + 1 \quad (2.36)$$

Then the reconstruction yields the following reconstructed point values \tilde{f}_k and the reconstructed first and second derivatives \tilde{f}'_k and \tilde{f}''_k :

$$\tilde{f}_k = f_k, \quad \tilde{f}'_k = \frac{f_{k+1} - f_{k-1}}{2h}, \quad \tilde{f}''_k = \frac{f_{k+1} - 2f_k + f_{k-1}}{h^2}, \quad k = j - 1, j, j + 1. \quad (2.37)$$

Therefore, the pointwise reconstruction of the space derivative f'_j is given by:

$$f'_j = \omega_{j-1}^j (\tilde{f}'_{j-1} + h\tilde{f}''_{j-1}) + \omega_j^j \tilde{f}'_j + \omega_{j+1}^j (\tilde{f}'_{j+1} - h\tilde{f}''_{j+1}). \quad (2.38)$$

The computation of the weights in (2.38) is the same as above (2.31) - (2.35), where the second set of constants C_k 's are taken from Table 2.2. The computation of the smoothness indicators IS_k^j in (2.34), have the point values f_j included, instead of the cell averages.

We use periodic and transmitting boundary in dependance on the numerical test problems.

In practice, three different families of smoothness indicators have to be computed during the reconstruction routine: one for the cell averages, one for the pointwise values and one for the flux derivatives. In addition, the ones for the flux derivatives have to be computed at each intermediate stage in the Runge- Kutta method. We confirm the finding of (Levy et al., 1999) that it is sufficient to compute all the indicators only once per time step, at the beginning of each time step. Here, only the construction of a fourth order scheme is presented. Once we have the established CRK4 working, we utilize it for applying the conservative-primitive variables concept in the case of systems. Since only fourth order scheme is considered, all the weights are positive. Using the same set of constants for calculating both the cell averages and the pointwise values further simplify the calculation as only two families of smooth indicators have to be computed.

To conclude, we outline the novel advantage of the proposed *Central*- WENO reconstruction, namely, the coupling of two approaches: the WENO approach, which

by using an adaptive stencil increase the over-all order accuracy but retain the non-oscillatory properties of the scheme and the central framework approach, in which no use of characteristic decomposition is needed and, hence, appears as a simple and robust approximation machinery.

2.4 The algorithm (Scalar)

In this section we summarize the CRK method, in order to provide a straightforward implementation of the scheme. The derivation of the CRK schemes are discussed in details in (Pareschi et al., 2005) and our objective here is to present the complete algorithm, containing the CRK predictor-corrector structure described in Section 2.2 with the CWENO reconstruction described in the previous section. The following algorithm is applicable to the scalar case. Applying a componentwise idea to the scheme constructs a generalization of this algorithm for the case of systems.

The Algorithm (Scalar case). Given the cell averages \bar{u}_j^n , at time t^n , compute the staggered cell averages at the next time step $\bar{u}_{j+1/2}^{n+1}$ as follows:

Step 1: Compute the coefficients of the parabolic interpolant $R_j(x) \forall j$, (2.29)

$$R_j(x) = u_j + u'_j(x - x_j) + \frac{1}{2}u''_j(x - x_j)^2.$$

The point values u_j and the derivatives, u'_j and u''_j , are given by (2.30). The weights ω_k , required in (2.30) and the smooth indicators are computed by means of (2.31)-(2.32) and (2.34). The constants C_k are the first set of constants appearing in Table 2.2. Once the point values are calculated, utilize them to evaluate $u_j^{(0)} = u^n(x_j)$.

Step 2: Computation of the intermediate states $u_j^{(i)}$.

For $i = 1, \dots, \nu - 1$:

- Compute the point values of the flux $f(u_j^{(i-1)}) \forall j$, where the point values $u_j^{(0)}$ are given from the reconstruction **Step 1** and any successive intermediate states would have been obtained in the former calculations in this step.
- Use these point values to reconstruct the first derivative of the flux $f'(u_j^{(i-1)})$, following the flux reconstruction procedure (2.37)-(2.38).

$$f'_j = \omega_{j-1}^j(\tilde{f}'_{j-1} + h\tilde{f}''_{j-1}) + \omega_j^j\tilde{f}'_j + \omega_{j+1}^j(\tilde{f}'_{j+1} - h\tilde{f}''_{j+1})$$

2. CWENO SCHEMES FOR SYSTEMS OF CONSERVATION LAWS

The weights in (2.38) are defined by (2.32), and the constants C_k are the second set in Table 2.2. The formulas for the smooth indicators are given with (2.34), but \bar{u}_k is replaced by f_k , $k = j - 2, \dots, j + 2$.

- Compute the predicted values $u_j^{(i)} = u_j^{(0)} - \Delta t \sum_{l=1}^{i-1} a_{i,l} f'(u_j^{(l-1)})$. The values of the coefficients $a_{i,l}$ are given in 2.15 (Pareschi et al., 2005).

Step 3: Compute the staggered cell averages $\bar{u}_{j+1/2}^{n+1}$ according to (2.16)-(2.17) on the staggered grid:

$$\bar{u}_{j+1/2}^{n+1} = \bar{u}_{j+1/2}^n - \lambda \sum_{i=1}^{\nu} b_i (f(u_{j+1}^{(i-1)}) - f(u_j^{(i-1)})) := \Xi_1 + \Xi_2. \quad (2.39)$$

The coefficients b_i are given in 2.15 (Pareschi et al., 2005).

Here, on the RHS of (2.39), the two terms can be explicitly written as follows:

1. The staggered cell averages are given in (2.10) and (2.29), thus:

$$\begin{aligned} \Xi_1 = \bar{u}_{j+1/2}^n &= \frac{1}{h} \int_{x_j}^{x_{j+1}} u^n(x) dx = \frac{1}{h} \int_{x_j}^{x_{j+1/2}} R_j(x) dx + \frac{1}{h} \int_{x_{j+1/2}}^{x_{j+1}} R_{j+1}(x) dx \\ &= \frac{u_j + u_{j+1}}{2} + \frac{u'_j - u'_{j+1}}{8} h + \frac{u''_j + u''_{j+1}}{48} h^2. \end{aligned}$$

The point values and the derivatives, u_j, u'_j, u''_j , have been computed in **Step 1**.

2. For the third and fourth order schemes, the second term can be written as Simpson's rule:

$$\begin{aligned} \Xi_2 = -\frac{\lambda}{6} &\{ [f(u_{j+1}^n) + 4f(u_{j+1}^{n+1/2}) + f(u_{j+1}^{n+1})] \\ &- [f(u_j^n) + 4f(u_j^{n+1/2}) + f(u_j^{n+1})] \} \end{aligned}$$

In our fourth order scheme, it yields:

$$\begin{aligned} \Xi_2 = -\frac{\lambda}{6} &\{ [f(u_{j+1}^{(3)}) + 2f(u_{j+1}^{(2)}) + 2f(u_{j+1}^{(1)}) + f(u_{j+1}^{(0)})] \\ &- [f(u_j^{(3)}) + 2f(u_j^{(2)}) + 2f(u_j^{(1)}) + f(u_j^{(0)})] \} \end{aligned}$$

where the predicted point values $f(u_j^{(i-1)})$, $i = 1, \dots, \nu - 1$ have been calculated in **Step 2**.

Note that after one time step, one finds the solution $\{\bar{u}_{j+1/2}^{n+1}\}$ on the staggered cells. Then a similar step must be repeated in order to obtain the solution $\{\bar{u}_j^{n+1}\}$ on the original grid. In any of these two half-time steps, the appropriate CFL condition have to be satisfied. Obeying the CFL condition allows the fundamental assumption in the central framework, namely, that the solution remains smooth at the boundaries of the staggered cell $[x_j, x_{j+1}]$. Then the discontinuities arising from the generalized Riemann problems defined at $x_{j+1/2}$ do not have time to reach the cell boundaries, which implies that one can assume that the degree of the smoothness of the solution at the edge of the cell will not be violated within one time step. Therefore the smoothness indicators can be computed only once per time step. Thus once the smooth indicators are computed from the cell averages (**Step 1** in the Algorithm 2.4) we can utilize the same values in any of the intermediate stages of the Runge-Kutta step.

The CFL condition for all central staggered schemes is:

$$\lambda \leq n_{CFL} \frac{1}{\max(|f'(u)|)} \leq \frac{1}{2} \frac{1}{\max(|f'(u)|)}$$

where n_{CFL} determines the maximum CFL number allowed for each CRK scheme. It is derived by the means of von Neuman stability analysis and it is very close to the actual CFL limit of these schemes, i.e. 0.5. Let $\rho(\xi)$ be the amplification factor of a data of the form $\bar{u}_j = \exp(ijh\xi)$ in the scheme applied to the linear advection equation. Then for $\lambda \leq n_{CFL}, \rho(\xi) \leq 1$ for all wave numbers ξ (see (Pareschi et al., 2005)) we have:

$$\begin{aligned} \text{CRK2 :} \quad & \lambda = \frac{1}{2} = 0.5 \\ \text{CRK3 :} \quad & \lambda = \frac{3}{7} \simeq 0.42 \\ \text{CRK4 :} \quad & \lambda = \frac{12}{25} = 0.48 \\ \text{CRK5 :} \quad & \lambda = \frac{60}{149} \simeq 0.40 \end{aligned} \tag{2.40}$$

We do not perform an algorithm version for the systems here. Such algorithm is presented in (Levy et al., 1999). It is based on component by component application to each equation of the systems of conservation laws. (Pareschi et al., 2005) improves the algorithm by discretizing first in time and after that in space. Our numerical results for systems are calculated with a new version of the algorithm for the systems, which is presented in Section 2.6. In our new algorithm, not only the componentwise

extension and projection along the characteristic directions are considered, but also a novel approach with a mapping between the conservative and the primitive variables in the intermediate stages is introduced, which improves the efficiency of the algorithm.

2.5 Scalar Equation Test

In this section we test the fourth order scheme for the single scalar equation. We demonstrate the numerically computed order of accuracy of the CRK schemes, which is in agreement with the pioneer results of (Levy et al., 1999) and (Pareschi et al., 2005). We show accuracy results on two classical scalar test problems: the linear advection equation and the nonlinear Burgers' equation.

We study the following test problems:

- **Linear advection equation**

$$\begin{aligned}
 u_t + u_x &= 0, \\
 u(x, t = 0) &= \sin^4(\pi x), \\
 \lambda &= 0.9\lambda_0 \text{ (given in (2.40))}, \quad \epsilon = 10^{(-6)}, \quad s = 2, \\
 &\text{periodic boundary conditions on } [-1, 1], \\
 &\text{computational time : } T = 1.
 \end{aligned}$$

- **Burgers' equation**

$$\begin{aligned}
 u_t + \left(\frac{1}{2}u^2\right)_x &= 0, \\
 u(x, t = 0) &= 1 + \frac{1}{2}\sin(\pi x), \\
 \lambda &= 0.66\lambda_0, \quad \epsilon = 10^{(-6)}, \quad s = 2, \\
 &\text{periodic boundary conditions on } [-1, 1], \\
 &\text{computational times : } T = 0.33 \text{ and } T = 1.6.
 \end{aligned}$$

Here, the first computation time is used for convergence tests, and the second computational time for the the shock capturing test. The shock develops at $T = 2/\pi$.

The accuracy tests are performed by the following norms of the error:

$$\begin{aligned}
 L^1 - error : \|\sigma\|_1 &= \sum_{j=1}^N |u(x_j, t^n) - u_j^n| h, \\
 L^\infty - error : \|\sigma\|_\infty &= \max_{1 \leq j \leq N} |u(x_j, t^n) - u_j^n|,
 \end{aligned}$$

2.5 Scalar Equation Test

| | Linear advection | | Burgers equation | |
|------|------------------|------------------|------------------|------------------|
| N | L^1 error | L^1 order | L^1 error | L^1 order |
| 40 | 0.7372e-02 | 3.6140 | 0.2260e-03 | 3.5280 |
| 80 | 0.7984e-03 | 3.2069 | 0.1050e-04 | 4.4744 |
| 160 | 0.2934e-04 | 4.7663 | 0.5148e-06 | 4.3688 |
| 320 | 0.1110e-05 | 4.7247 | 0.2222e-07 | 4.5415 |
| 640 | 0.6044e-07 | 4.1985 | 0.1190e-08 | 4.2223 |
| 1280 | 0.3745e-08 | 4.0009 | 0.7103e-10 | 4.0667 |
| N | L^∞ error | L^∞ order | L^∞ error | L^∞ order |
| 40 | 0.9231e-02 | 3.4072 | 0.1160e-02 | 3.5651 |
| 80 | 0.1407e-02 | 2.7135 | 0.6340e-04 | 4.5907 |
| 160 | 0.7995e-04 | 4.1377 | 0.3524e-05 | 4.2667 |
| 320 | 0.2185e-05 | 5.1933 | 0.1695e-06 | 4.4073 |
| 640 | 0.6140e-07 | 5.1534 | 0.9196e-08 | 4.2073 |
| 1280 | 0.3228e-08 | 4.0124 | 0.5402e-09 | 4.0895 |

Table 2.1: Convergence tests with fourth-order CRK scheme for the linear advection equation $u = \sin^4(\pi x)$ and Burgers equation, $u_0 = 1 + 1/2 \sin(\pi x)$.

where, $u(x_j, t^n)$ and u_j^n are the exact and the reconstructed solution at (x_j, t^n) , respectively. Note that for the Burgers' equation the exact solution is unknown and in order to evaluate the error one has to evaluate the difference not with the exact solution, but with a series of difference between the approximate solutions calculated with the higher number of points.

In Table 2.1 are shown the accuracy results for L_1 and L_∞ norms for CRK4 scheme for the both scalar tests. N is the number of grid points. The table summarize the order of accuracy of the scheme by refining the grid. In the nonlinear case (Burgers') the order of accuracy is computed far before the shock formation time $T = 2/\pi$. For brevity, the computations for all higher order CRK scheme are not presented in Table 2.1, but the results show that all higher order schemes studied here have the full accuracy in both L^1 and L_∞ norms. The more refining the grid, the smaller errors of the higher order CRK than those of the low-order schemes for a given number of points N . Only the CRK4 gives better results: its errors are smaller than those obtained with lower order schemes on all grids considered (Pareschi et al., 2005). This exception motivates

2. CWENO SCHEMES FOR SYSTEMS OF CONSERVATION LAWS

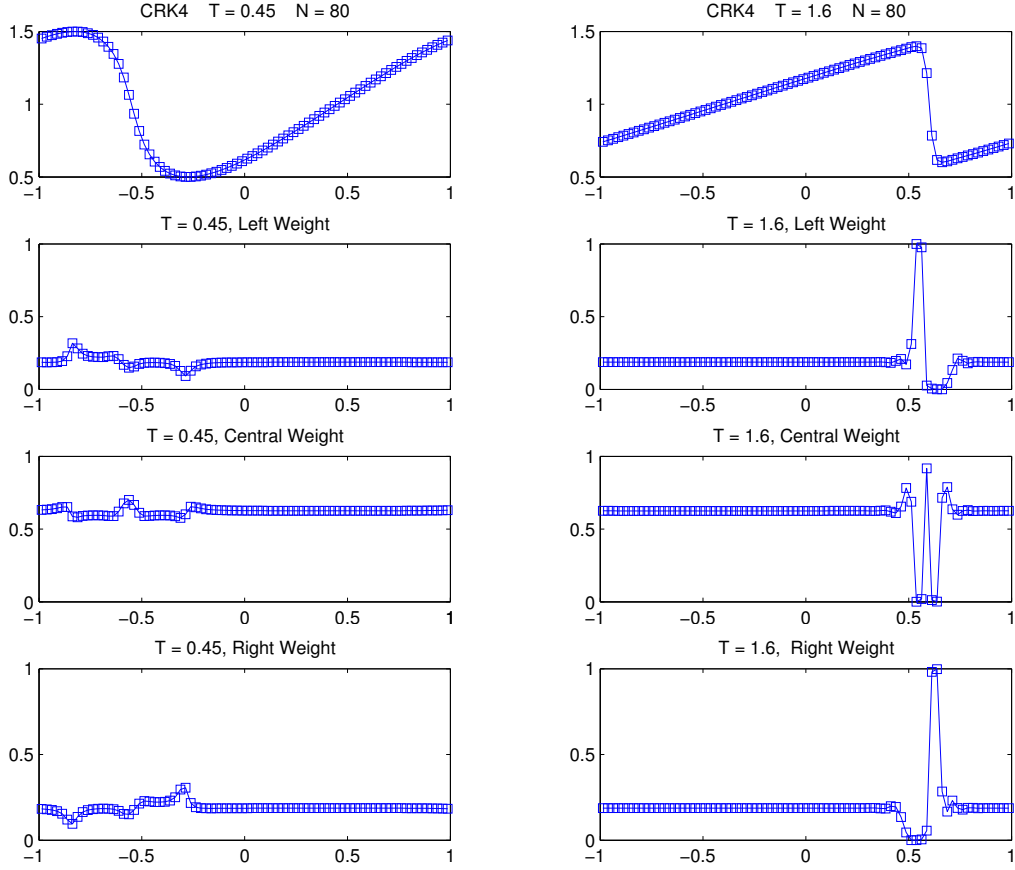


Figure 2.3: Burgers equation. All the weights are computed from the cell averages.

our choice of using the fourth-order CRK scheme from the variety of all higher order schemes as a test scheme for applying our new modification of the Algorithm 2.4 for systems.

On one hand, the convergence tests for a nonlinear scheme are used to check the correctness of the code. On the other hand, one can check whether the nonlinear weights do not destroy the accuracy. Further, if the expected accuracy is not reached, then one should check on the smooth solution with a linear scheme, where the weights are equal to the constants C_k . Doing so, it is verified whether the lack of the accuracy is due to the nonlinear weights or to a programming error. Our results show the expected correct order of accuracy.

The illustration of the shock-capturing behavior of the CRK scheme for the Burgers equation is presented in Figure 2.3. The snapshots on the left show the solution before

the shock formation ($T = 0.4$) and those on the right exhibit the solution after the shock formation ($T = 1.6$). The shock transition occurs within two cells. The complete set of weights ω_j^k , computed during the reconstruction step from the cell averages are shown below the solutions in the figure. Before the shock formation, the weights retain their equilibrium values. The sharp change, seen after the shock formation is due to excluding the stencils which would yield oscillations by assigning a zero weight value. Thus, the solution remains non-oscillatory once the shock has been formed.

2.6 Gas Dynamics Tests

In this section we show the application of CRK schemes to systems of conservation laws. In particular, we apply the schemes to the system of Euler equations of gas dynamics for a polytropic gas with a constant $\gamma = 1.4$. Such equations are have the vector of unknowns u and flux $f(u)$ determined as follows:

$$u = \begin{pmatrix} \rho \\ m \\ E \end{pmatrix}, \quad f = \begin{pmatrix} m \\ m^2/\rho + p \\ m(E + p)/\rho \end{pmatrix}, \quad (2.41)$$

where ρ is the density, $m = \rho v$ is the momentum, v is the velocity, p is the pressure and E is the total energy per unit volume, given by $E = \frac{1}{2}\rho v^2 + \rho e$, with e the internal energy, which is linked to the pressure through the equation of state $p = p(\rho, e)$, needed to close the system. For a polytropic gas $p = \rho e(\gamma - 1)$, i.e. p takes the form $p = (\gamma - 1)(E - \frac{1}{2}\rho v^2)$, where $\gamma = c_p/c_v$ denote the specific heat at constant pressure and volume, respectively.

We will consider typical test problems for gas dynamics, namely, the Sod and Lax tests defined by the initial data as follows:

- Shock tube problem with Sod's initial data (Sod, 1978)

$$\begin{cases} (\rho_l, m_l, E_l) = (1, 0, 2.5), & x < 0.5, \\ (\rho_r, m_r, E_r) = (0.125, 0, 0.25), & x > 0.5, \end{cases} \quad \text{Sod problem} \quad (2.42)$$

- Shock tube problem with Lax's initial data (Lax, 1954)

$$\begin{cases} (\rho_l, m_l, E_l) = (0.445, 0.311, 8.928), & x < 0.5, \\ (\rho_r, m_r, E_r) = (0.5, 0, 1.4275), & x > 0.5, \end{cases} \quad \text{Lax problem} \quad (2.43)$$

2. CWENO SCHEMES FOR SYSTEMS OF CONSERVATION LAWS

In both cases the computational domain is $[0,1]$. The time integration has been done up to $T_{max}=0.15$, i.e. before the perturbations reach the boundary of the computational domain. The mesh ratio is the optimal one for the Lax initial data, i.e. $\lambda = 0.1$; the number of points is $N = 240$ and $N = 480$.

In this section, we study three different approaches of approximation to the gas dynamics system. First we consider the straightforward componentwise application with the CRK schemes. This procedure is fast and economic, since only the flux function and an evaluation of the characteristic speeds are needed to perform the computations. Refining the grid improves the converges of the solution and decrease the amplitude of the possible spurious oscillations.

The second approach is based on *projection along the characteristic directions* at the beginning of each time step. This technique have been introduced by (Qui and Shu, 2002) and used by (Pareschi et al., 2005). The method is costly, because needs the flux function, and the matrix of the right eigenvalues for the Jacobian of the flux, together with its inverse. Such projection decomposition is a drawback with respect to the simplicity of the central scheme framework, but the results justify the huge benefit of using this approach. The improvement of the numerical solution, achieved by the projection along the characteristics are illustrated in the subsection 2.6.2.

The third approach considered in this section is a novel approach in the central schemes applied to systems. In particular, it is based on the calculation of the intermediate stages in primitive variables, while the CRK scheme retain its conservative properties. It implies a mapping between the conservative and the primitive variables in the implementation of the algorithm. Such approach appears quite useful in the case of relativistic hydrodynamics, where the computation of the numerical solution in the primitive variables is essential for solving the system of equations. We perform this new idea in the application of CRK schemes to relativistic hydrodynamics in Chapter 3.

2.6.1 Componentwise application and Global Smoothness Indicators

The component by component application of the CRK schemes is the most straightforward approach to the integration of systems of conservation laws. In (Levy et al., 1999), it was demonstrated that using the same Smoothness Indicators for all components amounts the robustness of the CRK scheme. Consequently, a Global Smoothness

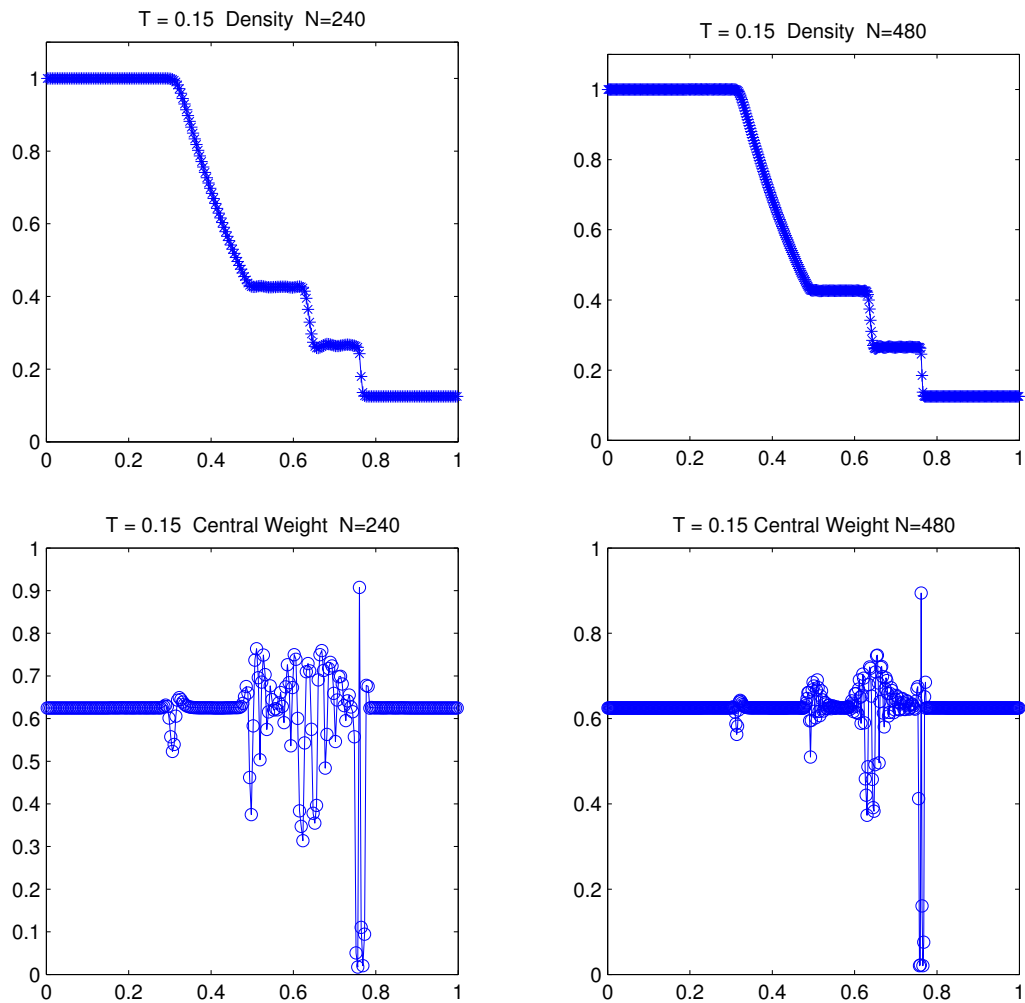


Figure 2.4: Density (top) and Central Weight (bottom) for Sod's Problem $\lambda = 0.1$. The weight is computed in the reconstruction of the cell averages.

2. CWENO SCHEMES FOR SYSTEMS OF CONSERVATION LAWS

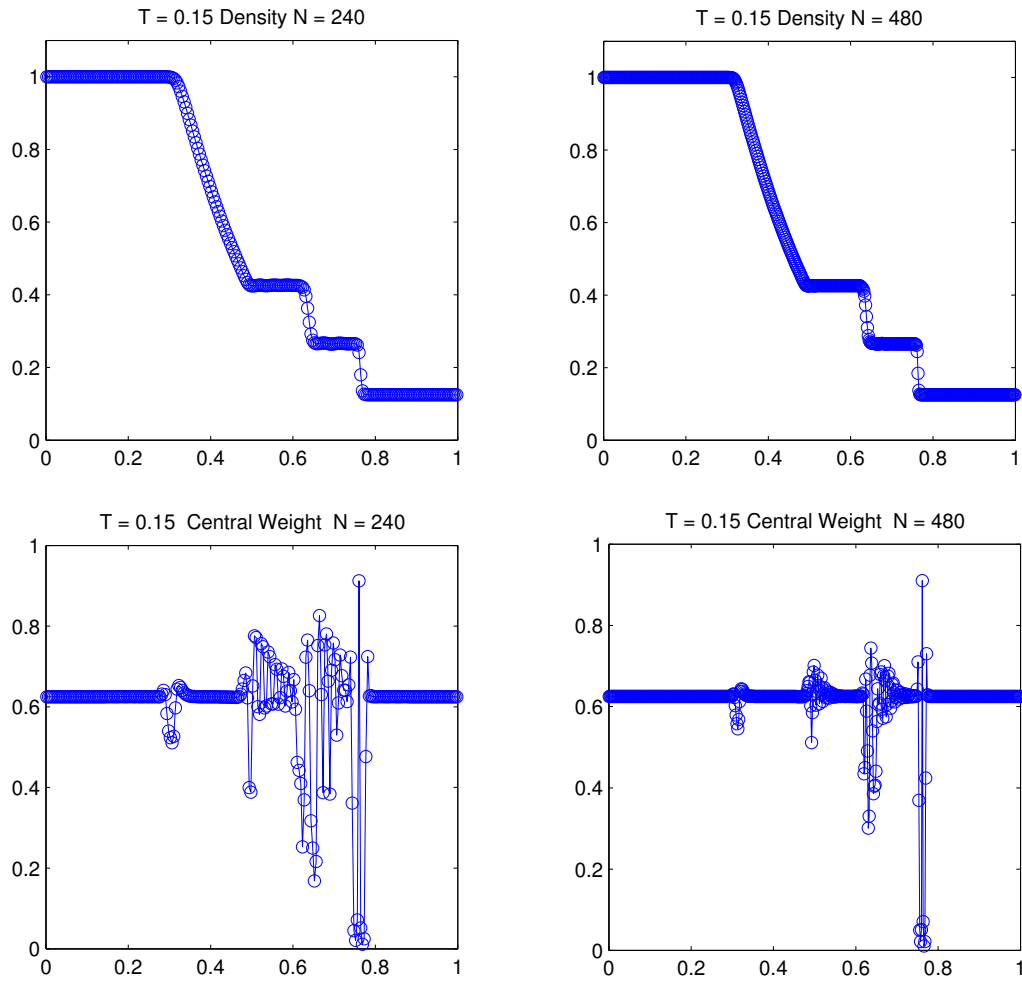


Figure 2.5: Density (top) and Central Weight (bottom) for Sod's Problem $\lambda = 0.1$. The weight is computed in the reconstruction of the cell averages.

Indicator was proposed in the following form:

$$IS_k^j = \frac{1}{d} \sum_{r=1}^d \frac{1}{\|\bar{u}_r\|_2} \sum_{l=1}^2 \int_{x_{j-1/2}}^{x_{j+1/2}} h_{2l-1}(P_{k,r}(l))^2 dx, \quad k = j-1, j, j+1, \quad (2.44)$$

where d is the number of equations, and $P_{k,r}$ denotes the k -th polynomial for the r -th component. The quantity $\|\bar{u}_r\|_2 = (\sum_{\text{all } j} |\bar{u}_r|^2 h)^{1/2}$ stands for a scaling factor, defined as the L^2 norm of the cell averages of the r -th component of u and can be exactly integrated analogous to (2.34). It was found by (Levy et al., 1999) that this strategy is effective even in the case of computing the Smooth Indicators only once per time step, at the beginning. The illustration of the improvement, achieved by the Global Smoothness Indicators strategy is more evident in Lax problem and can be observed in Figure 2.6. In brief, the Global Smoothness Indicator is just a weighted average of the Smoothness Indicators collected along each component. The weights are chosen to provide a dimensionless quantity. Such technique is less expensive and advances the Smoothness Indicators strategy in means of the accuracy of the numerical approximation with CRK schemes.

A series of figures, applied to both Sod's and Lax's problems review the benefit of Global Smoothness Indicators strategy. Figure 2.4 shows the results of applying the CRK4 scheme to Sod's problem with componentwise Smoothness Indicators and a fixed mesh ratio value $\lambda = 0.1$ for a different number of grid points, namely, $N = 240$ and $N = 480$. The small amplitude oscillations close to the contact discontinuity can be noticed. By refining the grid, $N = 480$, the amplitude of these ENO-type oscillations decreases. The results with the same setup but with Global Smoothness Indicators are presented in Figure 2.5. The central weights plotted in both figures are calculated at the last time step. The solution is oscillation-free close to the shock where the weights are set to almost zero by the Smoothness Indicators eliminating the "unsuitable" stencils. Vice versa, close to the contact discontinuity the weights do not vanish because the contact discontinuity is spread on several cells and the scheme does not recognize it as a discontinuity. Analogous tests have been done with Lax's initial data, where again the Global Smoothness Indicators approach slightly decrease the amplitude of the small spurious oscillations and where the oscillations in the weights are concentrated close to the discontinuity regions (see Figure 2.6). In short, following the pioneer work of (Levy et al., 1999) we tested our implementation of the CRK4 scheme with Global

2. CWENO SCHEMES FOR SYSTEMS OF CONSERVATION LAWS

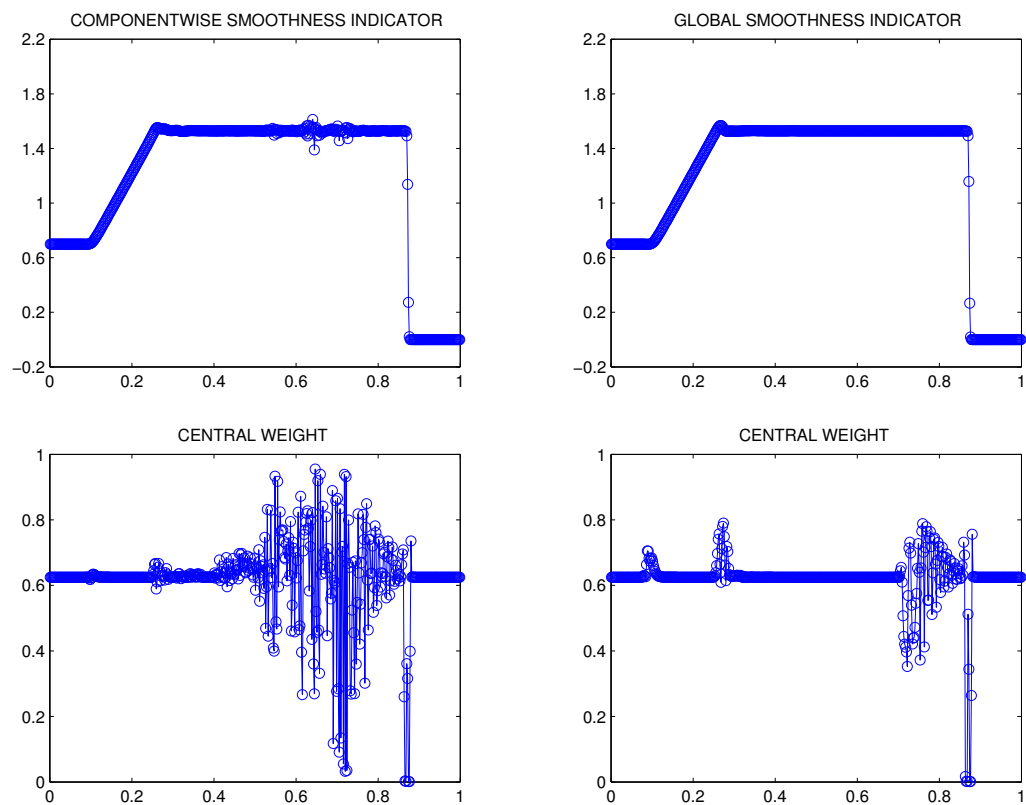


Figure 2.6: Velocity (top) and Central Weight (bottom) for Lax's Problem $\lambda = 0.1$. $T = 0.15$ and $N = 480$. The weight is computed in the reconstruction of the cell averages.

Smoothness Indicators strategy and we demonstrated the established improvement of the numerical solution close to the shock.

2.6.2 Projection along characteristics

Projection along the characteristic directions strategy has been proposed by (Pareschi et al., 2005). First, we review the algorithm of this strategy and after that we compare the numerical results for the Lax's problem applying the standard componentwise application of CRK schemes and the projection strategy to CRK4 scheme. The authors (Pareschi et al., 2005) emphasize that the best performance of the CRK family have the CRK2 and CRK4 schemes. The reasons for that are several, for example, the highest CFL numbers, which these schemes enjoy and the higher order of the reconstruction of the cell averages they have. In particular, the reconstruction of the cell averages for CRK4 and CRK5 are the same, but there are no negative constants in the reconstruction of the point values in the CRK4 scheme, which favors the robustness of the CRK4 scheme in comparison with the higher order schemes. Here, we apply the projection along the characteristic directions only to the CRK4 scheme.

Let us suppose that the Jacobian matrix $A(u)$ of the flux function $f(u)$ has a complete set of right eigenvectors, and let $R(u)$ be the non-singular matrix, whose columns are the right eigenvectors of $A(u)$. Let $\{\bar{u}_k^n\}$ be the data in the stencil of the j th cell. Then for the CRK4, the stencil consists of five points: $k = j - 2, j - 1, j, j + 1, j + 2$. The algorithm can be sketched as follows:

Algorithm(projection along the characteristic directions):

1. At each grid point j , compute $R(\bar{u}_j^n)$.
2. Map each cell average in the stencil of the j th cell along the characteristic directions, i.e. compute the vectors:

$$\bar{v}_k = R^{-1}(\bar{u}_j^n)\bar{u}_k^n, \quad k = j - 2, j - 1, j, j + 1, j + 2.$$

3. Construct a conservative interpolant Π_v^j for the cell averages $\{\bar{v}_k^n\}$ by means of:

$$\frac{1}{h} \int_{x_{k-1/2}}^{x_{k+1/2}} \Pi_v^j(x - x_j) dx = \bar{v}_k, \quad k = j - 1, j, j + 1.$$

2. CWENO SCHEMES FOR SYSTEMS OF CONSERVATION LAWS

4. Use the CWENO procedure from the Section 2.3 to compute the nonlinear weights, needed to construct the Π_v^j and map the interpolant to be in the conserved variables through the equation:

$$\Pi_u^j(x - x_j) = R(\bar{u}_j^n)\Pi_v^j(x - x_j).$$

5. Finally, use the last relation to evaluate the staggered cell average:

$$\bar{u}_{j+1/2}^n = \frac{1}{h} \int_{x_{j-1/2}}^{x_j} \Pi_u^j(x - x_j) dx + \frac{1}{h} \int_{x_{j-1/2}}^{x_j} \Pi_u^j(x - x_j) dx,$$

where the point value $u(x_j, t^n) = \Pi_u^j(0)$.

The algorithm is clearly conservative:

$$\begin{aligned} \frac{1}{h} \int_{x_{k-1/2}}^{x_{k+1/2}} \Pi_u^j(x - x_j) dx &= R(\bar{u}_j^n) \frac{1}{h} \int_{x_{k-1/2}}^{x_{k+1/2}} \Pi_v^j(x - x_j) dx \\ &= R(\bar{u}_j^n) \bar{v}_k = \bar{v}_k, \quad k = j - 1, j, j + 1. \end{aligned}$$

The matrices R and its inverse R^{-1} for the gas dynamics (see Tadmor (1997)) are given by:

$$R(u) = \begin{pmatrix} 1 & 1 & 1 \\ v - c & v & v + c \\ H - vc & H - \frac{c^2}{\gamma-1} & H + vc \end{pmatrix}, R^{-1}(u) = \begin{pmatrix} 1 + \frac{v}{c} - Z & -vY - \frac{1}{c} & Y \\ 2Z & 2vY & -2Y \\ 1 - \frac{v}{c} - Z & -vY + \frac{1}{c} & H + vc \end{pmatrix}$$

where v is the velocity, $H = (E + p)/\rho$ is the enthalpy per unit volume, $c = \sqrt{\gamma p/\rho}$ is the sound speed and $Y = (\gamma - 1)/c^2$, $Z = (H - v^2)Y$.

Now we consider the Lax's problem with fixed mesh ratio $\lambda = 0.2\lambda_{max}$. We apply the fourth-order CRK and plot only a zoom on the region containing spurious oscillations. On the right side we have contact wave and on the left one - a shock wave. If we apply first the simple componentwise strategy without projection along the characteristic direction one can clearly observe small amplitude of spurious oscillations, especially in the higher order schemes (the solutions obtained by up-to fifth order CRK schemes are presented in (Pareschi et al., 2005)). Note that the oscillations decay with refining the grid and, as expected, the shock wave is better captured than the contact wave by the scheme. If we apply the projection strategy the observed oscillations disappear. This convincing result has the disadvantage of not being economic, although more robust than the componentwise application, provided with being performed only once per time step. The results are presented in Figure 2.7.

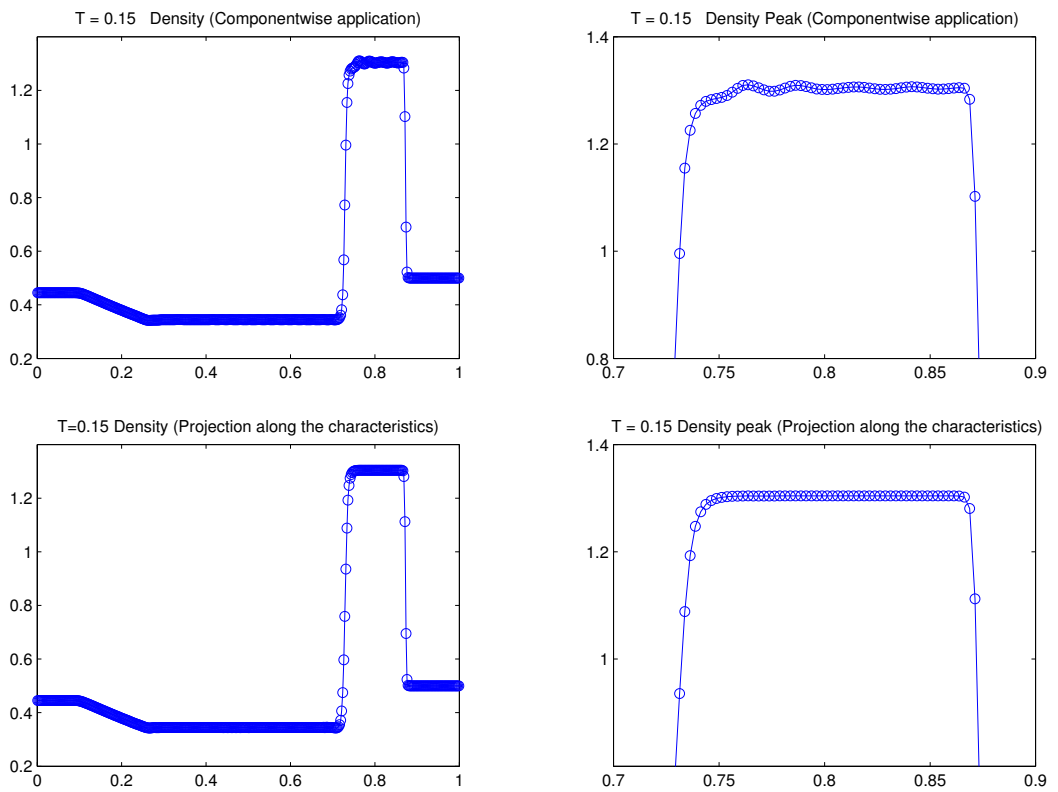


Figure 2.7: Lax's Problem $\lambda = 0.2\lambda_{max}$. The solution is given for $N = 400$

2.7 The new conservative-primitive variables strategy in the CRK schemes

Here we introduce a new concept in building the CRK schemes. It is based on the use of the primitive variables in the intermediate stages in the Runge-Kutta step. The primitive variables are the variables which express straightforward measurable physical quantities, for example, in gas dynamics such are density, velocity and pressure. On the other hand, the conservative variables are those which are used to have the system of conservation laws written in conservative form, i.e. for the gas dynamics case, such are density, momentum and total energy. In order to representing the system of conservation laws in primitive variables one should map the conservative ones into the primitive variables by 'mapping' equivalences. For the gas dynamics system, the 'mapping' is explicit and there is no need of solving an equation of high order for any of the variables. For the relativistic hydrodynamics, the mapping relations lead to the fourth-degree polynomial equation for one of the primitive variables and most likely a numerical solution has to be resolved at each time step. Still, polynomials of orders one to four are solvable using only rational operations and finite root extractions. Nevertheless, even analytical treatment of a quartic equation requires updating of the solution at every time step, hence, the efficiency of any conservative numerical scheme applied to the relativistic hydrodynamics is determined by the speed of solving the mapping equivalences between the conservative and the primitive variables. In the predictor-corrector framework of the CRK schemes family discussed in Section 2.2, the predictor step is the iterative step in which the intermediate stages of the Runge-Kutta are calculated. Therefore, a sufficient improvement of the scheme would be if there is no need of computing any mapping relations between the conservative and primitive variables at every iteration within the predictor step. Moreover, calculating the intermediate stages in primitive variables does not affect the conservative property of the scheme since the reconstruction and the corrector steps are calculated in the conservative variables. As a result, computationally, we obtain less expensive CRK scheme, and preserve the property of the scheme to be conservative. We refer to this new approach in the CRK schemes as *conservative-primitive variables* strategy.

2.7 The new conservative-primitive variables strategy in the CRK schemes

2.7.1 The algorithm (Systems)

The CRK algorithm, presented in Section 2.4 refers to the application of the CRK scheme to the scalar case. In this section, we present an algorithm for systems, based on the CRK algorithm for the scalar case with the conservative-primitive variables strategy integrated in the predictor step. In order to perform the predictor step in terms of primitive variables, a transformation matrix between the conservative and primitive variables for the flux must be considered. The Jacobian matrix of the transformation from the conservative to the non-conservative variables is defined by

$$Q = \frac{\partial u}{\partial w} \quad (2.45)$$

where w is the vector of the non-conservative variables. It is important to notice that this matrix requires explicit formulation of the constitutive fluid relations in gas dynamics (Hirsch, 1998). The definition of the non-conservative Jacobian does not require an explicit definition of the fluid relations, for example for the gas dynamics, it is not connected to a perfect gas assumption, which is involved explicitly in the conservative Jacobian. Therefore, the non-conservative matrix remains valid in a wide range of applications. In practice, computing the predictor step in primitive variables, requires calculating the non-conservative matrix of the primitive values at each iteration. The non-conservative Jacobian matrix $C(w)$:

$$\frac{\partial w}{\partial t} + C \frac{\partial w}{\partial x} = 0$$

is related with the conservative Jacobian matrix as follows:

$$C = Q^{-1} \tilde{A} Q$$

Here, \tilde{A} is the conservative Jacobian. In fact, introducing the transformation matrix Q in equation 2.1 leads to

$$Q \frac{\partial w}{\partial t} + \tilde{A} Q \frac{\partial w}{\partial x} = 0$$

or, after multiplication by Q^{-1} ,

$$\frac{\partial w}{\partial t} + (Q^{-1} \tilde{A} Q) \frac{\partial w}{\partial x} = 0 \quad (2.46)$$

Since we exchange the set of variables for the predictor step and the calculation of the intermediate stages is done in primitive variables, we need to recompute the CFL

2. CWENO SCHEMES FOR SYSTEMS OF CONSERVATION LAWS

condition 2.7 for the non-conservative Jacobian. If the characteristic speeds change wildly with time, we used an adaptive evaluation of the time step. In order to determine which of the characteristic speeds leads to the maximum eigenvalue of the non-conservative Jacobian, one has to evaluate its spectral radius from both sides at the center of the staggered cell, $x_{j+1/2}$. Therefore, first we evaluate the approximate solution in the conservative variables u^n at the both sides of the edge $x_{j+1/2}$ via the reconstruction polynomial $R_j(x)$, defined in 2.29:

$$\begin{aligned} u^n(x_{j+1/2} - 0) &= R_j(x_{j+1/2}) = u_{j+1/2}^- = u_j - \frac{1}{2}u'_j h + \frac{1}{8}u''_j h^2 \\ u^n(x_{j+1/2} + 0) &= R_{j+1}(x_{j+1/2}) = u_{j+1/2}^+ = u_j + \frac{1}{2}u'_j h + \frac{1}{8}u''_j h^2 \end{aligned} \quad (2.47)$$

and second we map the conservative pointwise values $u_{j+1/2}^-$ and $u_{j+1/2}^+$ into primitive pointwise values $w_{j+1/2}^-$ and $w_{j+1/2}^+$. Then we evaluate the spectral radius of the non-conservative Jacobian for the two edge values. In practice, one needs to evaluate only the characteristic speeds with the mapped primitive pointwise values. In any of the considered tests for systems in the thesis, the gas dynamics and the relativistic hydrodynamics, the spectral decomposition for the non-conservative matrix is well known. Details on the spectral decomposition of the non-conservative Jacobians of both systems are presented in the Subsection 2.7.2 and Section 3.3, respectively.

We end this subsection describing a new algorithm for the case of dxd systems of conservation laws. In the algorithm, \mathbf{u} denotes a d -dimensional vector with components $\mathbf{u} = (u^1, u^2, \dots, u^d)$.

The Algorithm (conservative-primitive variables strategy for systems).

Given the cell averages $\bar{\mathbf{u}}_j^n$, at time t^n , compute the staggered cell averages at the next time step $\bar{\mathbf{u}}_{j+1/2}^{n+1}$ as follows:

Step 1: Compute the coefficients of the parabolic interpolant $R_j(x) \forall j$, (2.29) from the scalar case:

$$R_j(x) = u_j + u'_j(x - x_j) + \frac{1}{2}u''_j(x - x_j)^2,$$

applying **Step 1** of **Algorithm 2.4** at each component of the vector $\bar{\mathbf{u}}_j^n$. The coefficients of the interpolant are now d component vectors. For the computation of the smoothness indicators one can apply (2.31)-(2.32) and (2.34) obtaining different smoothness indicators for each component or one can apply the global smoothness indicators strategy 2.44, defined in 2.6.1. The constants C_k are the first set of constants

2.7 The new conservative-primitive variables strategy in the CRK schemes

appearing in Table 2.2. Once the point values are calculated, we use them to evaluate $u_j^{(0)} = u^n(x_j)$. As a result, the pointwise conservative variables \mathbf{u}_j^n from the cell averages $\bar{\mathbf{u}}_j^n$ have been obtained.

Step 2: Evaluate the approximated pointwise value solution \mathbf{u}_j^n with the reconstruction polynomial $R_j(x)$ at both sides of the cell edge of the unstaggered cell, $x_{j+1/2}$, by using the relations 2.47 . As a result, the approximated solution $\{\mathbf{u}_{j+1/2}^-, \mathbf{u}_{j+1/2}^+\}$ has been obtained at the center of the staggered cell, where the discontinuities might arise from the generalized Riemann problems.

Step 3: Compute the primitive pointwise values $\mathbf{w}_j^n, \{\mathbf{w}_{j+1/2}^-, \mathbf{w}_{j+1/2}^+\}$ from the conserved pointwise values $\mathbf{u}_j^n, \{\mathbf{u}_{j+1/2}^-, \mathbf{u}_{j+1/2}^+\}$. The mapping between the two sets of variables is unique for every system and depends on the choice of the physical quantities one chooses as a set of primitive variables. For more details, see the mapping relations for the gas dynamics in Subsection 2.7.2 and for the relativistic hydrodynamics in Section 3.3.

Step 4: By using 2.7, compute the new time step. For the spectral radius in the 2.7 use the maximum value

$$\max_j \max \{ \rho(\tilde{A}(w_{j+1/2}^-)), \rho(\tilde{A}(w_{j+1/2}^+)) \}$$

Step 5: Computation of the intermediate states $\mathbf{w}_j^{(i)}$.

For $i = 1, \dots, \nu - 1$:

- Utilize the pointwise values $\mathbf{w}_j^{(i-1)} = (w_j^1, \dots, w_j^d) \quad \forall j$ to reconstruct the first derivative of $\mathbf{w}_j^{(i)}$:

$$\mathbf{w}_{x_j}^{(i-1)} = - \frac{\partial \mathbf{w}^{(i-1)}}{\partial x} \Big|_{x_j}, \quad (2.48)$$

following the CWENO reconstruction procedure in (2.30) for the derivative of the solution:

$$\mathbf{w}'_j = \omega_{j-1}^j (\tilde{\mathbf{w}}'_{j-1} + h \tilde{\mathbf{w}}''_{j-1}) + \omega_j^j \tilde{\mathbf{w}}'_j + \omega_{j+1}^j (\tilde{\mathbf{w}}'_{j+1} - h \tilde{\mathbf{w}}''_{j+1})$$

The point values $\mathbf{w}_j^{(0)}$ are given from the reconstruction **Step 1** after applying the mapping procedure from **Step 3**. The weights in (2.30) are defined by (2.32),

2. CWENO SCHEMES FOR SYSTEMS OF CONSERVATION LAWS

and the constants C_k are the second set in Table 2.2. As in **Step 1**, the smoothness indicators can be computed either by a componentwise or a global strategy. Again, the derivative reconstruction is applied at each component of \mathbf{w}_j^n .

- Compute the point-values non-conservative Jacobians $C(\mathbf{w}^{(i-1)}) = \mathbf{f}'(\mathbf{w}^{(i-1)})$. The matrices C can be calculated by using (2.46) at each component of \mathbf{w} .
- Compute the predicted values $\mathbf{w}_j^{(i)} = \mathbf{w}_j^{(0)} - \Delta t \sum_{l=1}^{i-1} a_{i,l} \mathbf{C}(\mathbf{w}_j^{(l-1)}) \mathbf{w}_{x_j}^{(i-1)}$. The values of the coefficients $a_{i,l}$ are given in 2.15.

As a result the intermediate states as pointwise values have been calculated by using the set of the primitive variables.

Step 6: Obtain the intermediate point-value states in conservative variables by using the reverse mapping from the primitive into conservative variables, i. e. compute $\mathbf{u}_j^{(i-1)} = (u_j^1, \dots, u_j^d)$ from $\mathbf{w}_j^{(i-1)} = (w_j^1, \dots, w_j^d) \quad \forall j$. Such a transformation is specific for every single system, hence, the form of the matrix transformation is strongly connected with the physics of the problem.

Step 7: For $i = 1, \dots, \nu - 1$, compute the point values of the flux,

$$\mathbf{f}^{(i-1)} = \mathbf{f}(\mathbf{u}_j^{(i-1)}, \mathbf{w}_j^{(i-1)}) \quad \forall j,$$

for each component of the flux function $\mathbf{f}(\mathbf{u}_j^n)$.

Step 8: Apply **Step 3** of **Algorithm 2.4** to each component of the conservation law.

The requirement to compute non-conservative Jacobians during the intermediate stages implies that the code is computationally more expensive than one that calculates the predictor step in conservative variables. Nevertheless, the numerical tests show that the time consuming of updating the non-conservative Jacobian in each intermediate stage is much less in comparison with the time needed for updating the approximate solution in conservative variables. Moreover, in the special relativistic hydrodynamics, for example, the reconstruction has to be done in primitive variables since reconstructing the conserved variables can produce unphysical values.

2.7 The new conservative-primitive variables strategy in the CRK schemes

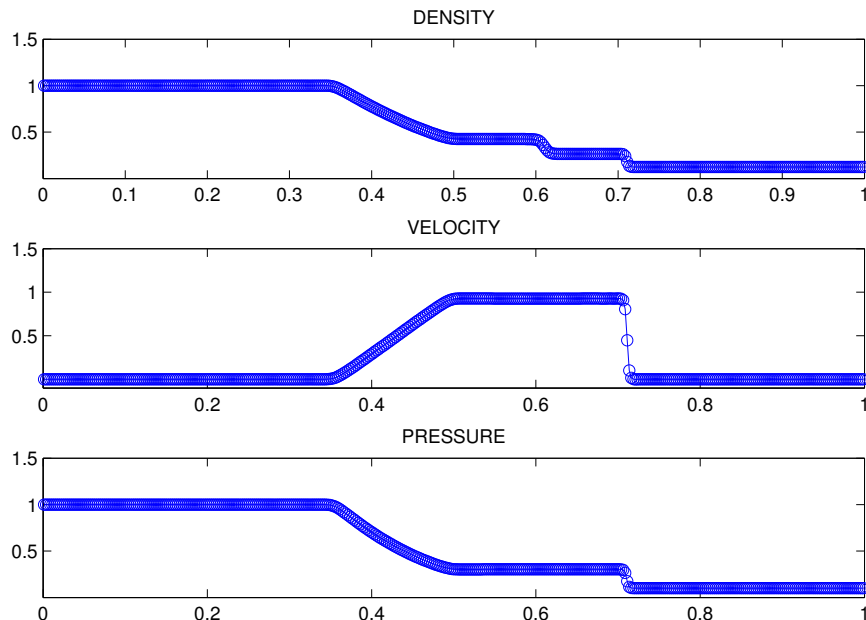


Figure 2.8: The density (top), velocity (middle) and the pressure (bottom) profiles for Sod's Problem, computed by the conservative-primitive variables strategy and projection along the characteristics approach. $T = 0.12$ and $N = 400$.

2.7.2 Gas dynamics test

The one-dimensional Euler equations in conservation form are given by (2.41). The conservative variables are the density ρ , the momentum, $m = \rho v$, and the total energy per unit volume, $E = \frac{1}{2}\rho v^2 + \rho e$, where e is the internal energy. Then the Jacobian for the system with the conservative variables (Hirsch, 1998) is

$$\tilde{A} = \begin{pmatrix} 0 & 1 & 0 \\ -(3-\gamma)\frac{v^2}{2} & (3-\gamma)v & \gamma-1 \\ (\gamma-1)v^3 - \frac{\gamma v E}{\rho} & \frac{\gamma E}{\rho} - \frac{3}{2}(\gamma-1)v^2 & \gamma v \end{pmatrix}$$

By writing the system in the set of primitive variables $(\rho, v, p)^T$, where ρ is the density, v is the velocity and p is the pressure, one has the non-conservative Jacobian for the Euler equations

$$C = \begin{pmatrix} v & \rho & 0 \\ 0 & v & 1/\rho \\ 0 & \rho c^2 & v \end{pmatrix}$$

2. CWENO SCHEMES FOR SYSTEMS OF CONSERVATION LAWS

where c stands for sound speed and has the form $c^2 = \gamma p / \rho$ for ideal equation of state. The non-conservative Jacobian is much simpler than the conservative one and does not include γ explicitly, hence, has a larger validity range. For a polytropic gas the pressure is given by $p = \rho e(\gamma - 1)$, i.e. $p = (\gamma - 1)(E - \frac{1}{2}\rho v^2)$, where $\gamma = c_p/c_v$ denote the specific heat at constant pressure and volume, respectively. Hence, for converting the conservative to the primitive variables in gas dynamics, one has the following mapping equivalences

$$\begin{pmatrix} \rho \\ m \\ E \end{pmatrix} \longrightarrow \begin{matrix} \rho \\ v = m/\rho \\ p = (\gamma - 1)(E - \frac{1}{2}\rho v^2) \end{matrix} \longrightarrow \begin{pmatrix} \rho \\ v \\ p \end{pmatrix} \quad (2.49)$$

The spectral radius of the non-conservative Jacobian is defined by $\max_{1 \leq i \leq d} |\lambda_i(C)|$, where $\lambda_i(C)$ is the i -th eigenvalue of the Jacobian C . For Euler equations is given by $\lambda(C) = v + c$. In Figure 2.8 are shown the density, the velocity and the pressure computed with the Algorithm 2.7.1 for the Sod shock tube problem, discussed already in Section 2.6. The test is computed with the projection along the characteristic direction strategy, introduced in Subsection 2.6.2. The computational time with the Algorithm 2.7.1 is similar to the computational time achieved by the Algorithm 2.4 applied to systems. By comparing the results obtained by applying the algorithms to the Sod test, we checked the validity and the robustness of the new conservative-primitive variables strategy in the CRK schemes. The calculation of the non-conservative Jacobian does not increase the computational cost of the Algorithm 2.4 applied to system while enjoys the feature of using the primitive variables for intermediate states, which plays important role in avoiding the unphysical solutions in the application to the more intricate systems as the special relativistic hydrodynamics.

2.8 The CRK schemes versus established astrophysical codes

Numerical simulations based on the so-called high-resolution shock-capturing (HRSC) schemes enjoy an increasing amount of scientific attention in astrophysical community because these schemes used in the simulations have the ability to model highly supersonic flows while preserving the accuracy and robustness. The reconstruction technique, implemented in most of the HRSC algorithms together with the proper Godunov-type upwinding, which requires an exact or approximate solution of a Riemann problem are

2.8 The CRK schemes versus established astrophysical codes

the basic features highly employed in the recent high-resolution astrophysical codes examples of which include the new NIRVANA (Ziegler, 2004), versatile advection code (VAC) (Toth, 1996), FLASH (Fryxell et al., 2000), PLUTO (Mignone et al., 2007), BATS-R-US (Powell et al., 1999) and ATHENA (Stone et al., 2008). The new family of CRK schemes, which are considered in the thesis is the further step of improving the shock capturing feature of the modern high resolution methods. In the following two subsections we review some shock tube tests made by two of the widely used free available MHD codes, namely, ZEUSMP2 (Stone and Norman, 1992) and ATHENA (Stone et al., 2008). The latter does not employ operator-split finite-difference method as it does its predecessor, ZEUS, but utilize second-order Godunov methods for fully conservative updates of the MHD equations.

2.8.1 The ZEUS-MP/2 code

The 3D astrophysical MHD code ZEUS-MP/2 (Stone and Norman, 1992) is still probably the most used member of the ZEUS family of codes. The first ZEUS code was developed by (Stone and Norman, 1992a), (Stone and Norman, 1992b), (Stone et al., 1992) and was extended to 2D and 3D (Jim Stone's ZEUS-2D and ZEUS-3D releases) and further to the Robert Fiedler's parallelized version ZEUSMP which has been used in this thesis. As the authors note the "MP" suffix stands for "multi-physics," "massively parallel," and "message passing" aspects of the code. ZEUS-MP/2 is a time-explicit three-dimensional computational fluid dynamics code for the simulation of astrophysical phenomena, based on the method of finite-differences already used in ZEUS-3D and parallelized using the MPI message-passing library. The algorithms in ZEUS are utilized for simulations on 1, 2, or 3-dimensional grids and can be divided in three areas: hydrodynamics (HD), magnetohydrodynamics (MHD) and radiation hydrodynamics (RHD). The HD and MHD modules have been used for the aims of the present work. The advantages of the ZEUS algorithm have been and remain the high degree of robustness and speed and its ability to accommodate additional physics such as viscosity, radiation, self-gravity etc., without harming the numerics in its underlying MHD algorithm. Overview on the numerical scheme adopted by ZEUS-MP/2 reads an *operator-split* scheme characterized by: (1) *source step*, in which fluid velocities and internal energies are updated due to the effects of body forces, artificial viscosity, local heating/cooling/transport due to radiation diffusion (if applicable), and the subsequent

2. CWENO SCHEMES FOR SYSTEMS OF CONSERVATION LAWS

(2) *transport step*, whereby these fluid velocities are used to advect the field variables (density, internal energies, composition) through the computational mesh. The ZEUS family of codes is not conservative, and hence generated error at shocks cannot be reduced by increasing the resolution. In order to capture possible shocks ZEUS relies on stabilization accomplished by von Neumann-Richtmyer artificial viscosity (von Neumann and Richtmyer, 1950). The stabilization is needed only for the compressional (fast and slow) waves, since the entropy and the Alfvén waves are upwinded in the ZEUS codes. The artificial viscosity is utilized by dual means: (1) the first so-called *quadratic term* is responsible for the regions of strong compression and effectively captures shocks, and (2) the linear term is applied throughout the grid and stabilizes continuous structures such as magneto-acoustical and rarefaction waves. The typical values in all applications for the quadratic term are 1-2 and 0.1- 0.2 in one-dimensional shock-tube problems. For MHD applications one has to combine the isothermal equation of state with linear artificial viscosity in order to reach the accurate treating of shocks. Recently, a new record on the reliability of ZEUS-3D (Clarke, 2010) has been published as a response of long dated critiques of ZEUS-3D. (Balsara, 2001), (Falle, 2002), (Tasker et al., 2008) suggest that the MHD algorithms in ZEUS can result in significant shock and rarefaction error. The conclusions made by (Falle, 2002) are that results obtained by ZEUS are acceptable for pure gas dynamics if the linear artificial viscosity is multiplied by the smallest local CFL since the shock errors are small in this case. However, for adiabatic MHD, the tests are not satisfactory. The shock error disappear for isothermal equation of gas, but the rarefaction shocks arise and still ZEUS can not be trusted. Instead, increasing the linear artificial viscosity, one can add artificial resistivity to cope with the onset of the rarefaction shocks. By their origin, the rarefaction shocks are steady structures whose size do not increase with time. Due to the nonlinearity these structures have being spread, and hence, the code truncation error must contain antidiffusive term. (Falle, 2002) explain this fact with the second-order in space and first-order in time for ZEUS and supports this statement with the analogous result for upwind scheme. He compares HD and MHD shock tube tests done with ZEUS and with his own conservative upwind code. On the other hand, (Clarke, 2010) claim that such rarefaction waves arising in some one dimensional Riemann problem are unlikely to occur in multi-dimensional astrophysical applications. Moreover, comparing the results of a non-conservative algorithm with analytical solutions of the

2.8 The CRK schemes versus established astrophysical codes

conservative equations it is hardly to be adequate for the conclusions on the integrity of the underlying HD methods. Since ZEUS is one of the established MHD code for astrophysical computations such a discussion appears of great importance to validate the great amount of published results, obtained with ZEUS. This thesis can be considered as an attempt to address these concerns and to contribute the field of the computation astrophysics with introducing the novel robust CRK algorithm as improving even further the need of high-resolution shock-capturing methods in astrophysics. On one hand, CWENO schemes overcome the lack of shock-capturing feature in the operator-splitting schemes. On the other hand, the CRK enjoys the free-Riemann-problem central approach, which is expected to be very efficient especially for high dimensions, where the upwind schemes require exact or approximate solution of the Riemann problem. ZEUS family of codes are staggered-cell MHD codes. Hence the results of one dimensional hydrodynamical Riemann test problems done with our conservative-primitive variables strategy CRK scheme (CRK-CPVS) and ZEUS-MP/2 appear to be good candidates to check the accuracy, the speed and the robustness of two different designs of the applied CWENO and operator-splitting numerical schemes. Figure 2.9 show the density profile calculated with ZEUS-MP/2 and CRK4 with conservative-primitive variables strategy included at time $T = 0.4$ for the following Sod's shock tube test problem:

$$\begin{cases} (\rho_l, v_l, p_l) = (10, 0, 100), & x < 2, \\ (\rho_r, v_r, p_r) = (1, 0, 1), & x > 2, \end{cases} \quad (2.50)$$

The stronger discontinuities across the shock interface and the narrow density peak that forms behind the shock in this Sod's problem justify its important role as a first test for hydrodynamical codes. Initially the discontinuity is located at position $x = 2$. Both approaches represent efficiently, though, the operator-splitting finite-difference nonconservative ZEUS-MP/2 show small oscillations near the density peak and seem less accurate than the CRK scheme. Surely, the key role of capturing the shock in ZEUS is played by the artificial viscosity. In the original work of von Neumann-Richtmyer (von Neumann and Richtmyer, 1950) it is given by

$$Q = \begin{cases} -\alpha \frac{\partial v}{\partial x} & \text{if } \frac{\partial v}{\partial x} < 0, \text{ or } \frac{\partial \rho}{\partial x} > 0 \\ 0 & \text{otherwise,} \end{cases}$$

with $\alpha = \rho(kh)^2 \partial v / \partial x$, where k is the parameter which value has to be chosen in every numerical experiment and controls the number of zones in which the shock is spread.

2. CWENO SCHEMES FOR SYSTEMS OF CONSERVATION LAWS

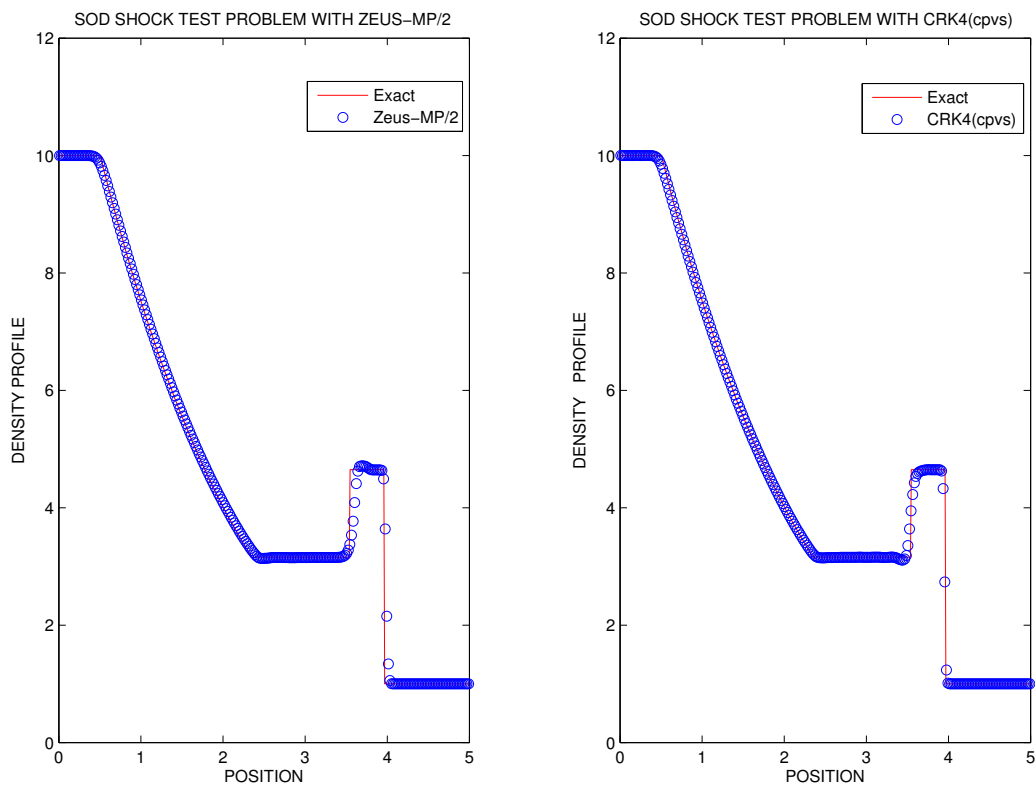


Figure 2.9: Comparison between ZEUS-MP/2 code(*Left*) and CRK4(with conservative-primitive variables strategy)(*Right*) for Sod's problem 2.50. The solution is given at time $T = 0.4$ for $N = 256$ points.

2.8 The CRK schemes versus established astrophysical codes

The artificial viscosity approach was widely used mainly because of its simplicity, resulting in high computational efficiency. A drawback for using artificial viscosity is that is problem dependent and hides ambiguity of finding the exact form of Q sufficient to reduce the spurious oscillations by adding the necessary amount of dissipation, without introducing excessive smearing in the discontinuities. Satisfying both of these properties simultaneously might be a tricky task in various astrophysical applications.

Figure 2.10 shows the specific energy of the Sod shock-tube problem as computed by ZEUS-MP.2 and CRK4(CPVS) scheme using 256 grid cells. The analytic solution (solid line) shows: (1) the shock wave at far right, (2) a contact discontinuity and (3) the rarefaction fan at left. The shock and the contact discontinuity are resolved by about 4 grid cells for ZEUS-MP/2 and 2 grid cells for CRK4, consistent with the artificial viscosity used in the second-order van Leer advection algorithm and the CWENO algorithm 2.7.1, respectively. Due to the diffusivity of both schemes, the foot and head of the rarefaction fan are slightly smeared. Nevertheless, the weak point in the central approach is in its diffusivity and we note that in the discontinuity this drawback of CRK schemes is successfully overcome. As (Stone and Norman, 1992a) noted the amplitude of the specific energy is incorrect behind the shock front. The authors address this effect to the use of density and specific internal energy as the fundamental variables, being evolved with ZEUS-MP/2 with using consistent transport scheme, while the fundamental variables in the shock-tube problem are density and pressure. To summarize, the hydrodynamic equations as a nonlinear hyperbolic system might produce discontinuous data from smooth initial in a finite time during the evolution. Classical difference-schemed codes as ZEUS might exhibit non accuracy when dealing with such system. The second order (or higher) schemes produce spurious oscillations near discontinuities, which do not disappear as the grid is refined. In ZEUS-MP/2 is used as artificial viscosity approach to ensure high-order, oscillation-free accurate representations of discontinuous solutions. The basic idea is to introduce a purely artificial dissipative mechanism which function is to smooth the shock transition while by extending over a small number of grid cells. Finding the appropriate form and strength for the artificial viscosity term might appears difficult task. In comparison, the CRK4-CPVS as high-resolution shock -capturing conservative method offers accurate and efficient method for solution of the system of nonlinear hyperbolic conservation laws.

2. CWENO SCHEMES FOR SYSTEMS OF CONSERVATION LAWS

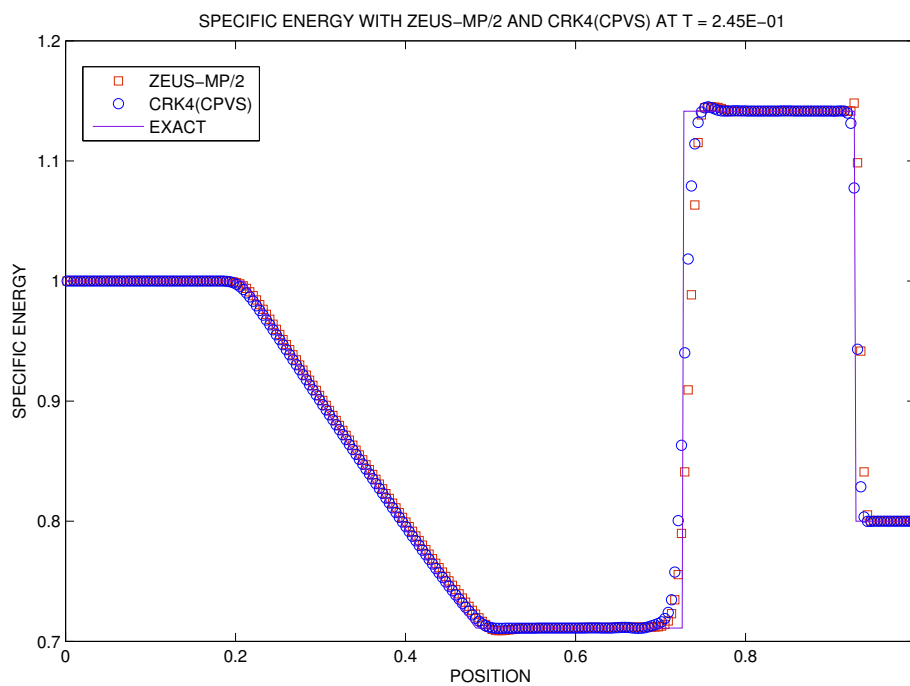


Figure 2.10: Specific energy as computed by ZEUS-MP/2(open squares) and CRK4-CPVS(open circles) for the Sod shock-tube problem 2.42 at time $T = 0.245$. The analytic solution is plotted as a solid line. The number of grid cells are 256.

2.8.2 The ATHENA code

The ATHENA code (Gardiner and Stone, 2005),(Gardiner and Stone, 2008),(Stone et al., 2008) is the ancestor of ZEUS family of code, but employing new high-resolution shock-capturing second-order Godunov algorithms. It is created for solving the equations of ideal magnetohydrodynamics (MHD) by preserving the divergence-free constraint, $\nabla \cdot B = 0$, via unsplit evolution of magnetic field. ATHENA is fully conservative code and utilized directionally-unsplit higher-order Godunov methods which not only are ideal for implementation on modern parallel computer systems with adaptive mesh refinement(AMR), but also are superior for shock capturing and evolving contact discontinuities that are typical for astrophysical flows. The ATHENA authors emphasized that their primary motivation was to develop modern conservative ideal MHD code, adequate for nested grid (AMR) computations. Here, our aim is to comment on the performance of CRK4-CPVS scheme in comparison with one of the established modern astrophysical codes. We discuss two one-dimensional hydrodynamic examples to benchmark the numerical hydrodynamical algorithms. As a further step, ATHENA use piecewise parabolic Godunov algorithm for HD which requires solution of a Riemann problem. As a central approach, i.e. more diffusive than the Godunov upwind one, the CRK4 scheme can be superior mainly in its speed and robustness due to its Riemann-solver-free construction.

The first numerical test is of slow-moving shock. In particular oscillations are frequently seen if the shock is moving slowly, i.e. the shock speed is very small relative to the fastest characteristic speeds in the problem. Then it takes several time steps to cross a single grid cell even when CFL is close to one. Hence it is likely to arise oscillations when Godunov's method based on the exact Riemann solver is being used because the numerical viscosity is vanished when the solution is a single shock with speed close to zero. For scalar problems this allows nearly stationary shocks to be captured sharply. Vice versa, for nonlinear systems the same situation lead to onset of oscillations. As an example we use the one proposed by (LeVeque, 2002):

$$\begin{cases} (\rho_l, v_l, p_l) = (1.0, 3.44, 1.0), & x < 0, \\ (\rho_r, v_r, p_r) = (3.86, 0.81, 10.33), & x > 0, \end{cases} \quad (2.51)$$

Initially, the discontinuity is located at $x = 0$ at a cell interface. The number of points is 256 grid cells. Figure 2.11 shows the results of slow moving shock as computed by

2. CWENO SCHEMES FOR SYSTEMS OF CONSERVATION LAWS

ATHENA code (*Left*) and as computed by CRK4-CPVS (*Right*). The vertical sequence of plots includes the density, the velocity and the pressure profiles calculated at time $T = 0.8$. As we see the spurious oscillations, which do not disappear with refining the grid, do not arise in the solution computed by CRK4-CPVS. The shock is resolved in 2 grid cells for CRK4 scheme, consistent with CWENO method. If one uses higher than second order Godunov method the oscillations in the solution remain. Applying even limiters do not reduce the spurious oscillations. The success of the CRK4 method to the slow-moving shock test it is likely to be due to the fact of the more dissipative characteristics of the central approach. In addition, the main advantage of CRK4-CPVS scheme of preventing the onset of oscillations it is more evident, particularly for multidimensional computations in regions where strong shocks are nearly aligned with the grid. The lack of dissipation in Godunov-type methods can lead to cross-flow instability and hence to the appearance of unphysical structures from the shock.

The second numerical which we present in this subsection is the so-called Sjögren problem (Sigalotti et al., 2006). It deals with a Riemann problem with the following initial data:

$$\begin{cases} (\rho_l, v_l, p_l) = (1.0, -2.0, 0.4), & x < 0, \\ (\rho_r, v_r, p_r) = (1.0, 2.0, 0.4), & x > 0, \end{cases} \quad (2.52)$$

Here $\gamma = 1.4$. This test is consist of states that are mirror each to the other and hence reflected boundary conditions is the obvious choice at $x = 0$. The problem is discussed by (Einfeldt et al., 1991) where it was used to check whether the internal energy and density remain positive during the computational process, i.e. the scheme is so-called positively conservative. The test consists of two strong rarefaction waves, one travelling to the left and the other to the right. Since the fluid moves outward from the origin, a region of very low density and pressure forms within the rarefactions. the importance of such numerical test is the fact that most Godunov-type schemes whose interface fluxes are derived from a linearized Riemann solution(for example, Roe's scheme) are not positively conservative and fail on this test problem (Einfeldt et al., 1991). A typical example of representing the considered problem is when the reflecting boundary conditions are used at a solid wall and the fluid flow is directed away from the wall, for instance, the external flow behind an obstacle. Both ATHENA and CRK4-CPVS perform best on this test. Then the less expensive CRK scheme could be considered as a sufficient method for resolving physical situations with fluid

2.8 The CRK schemes versus established astrophysical codes

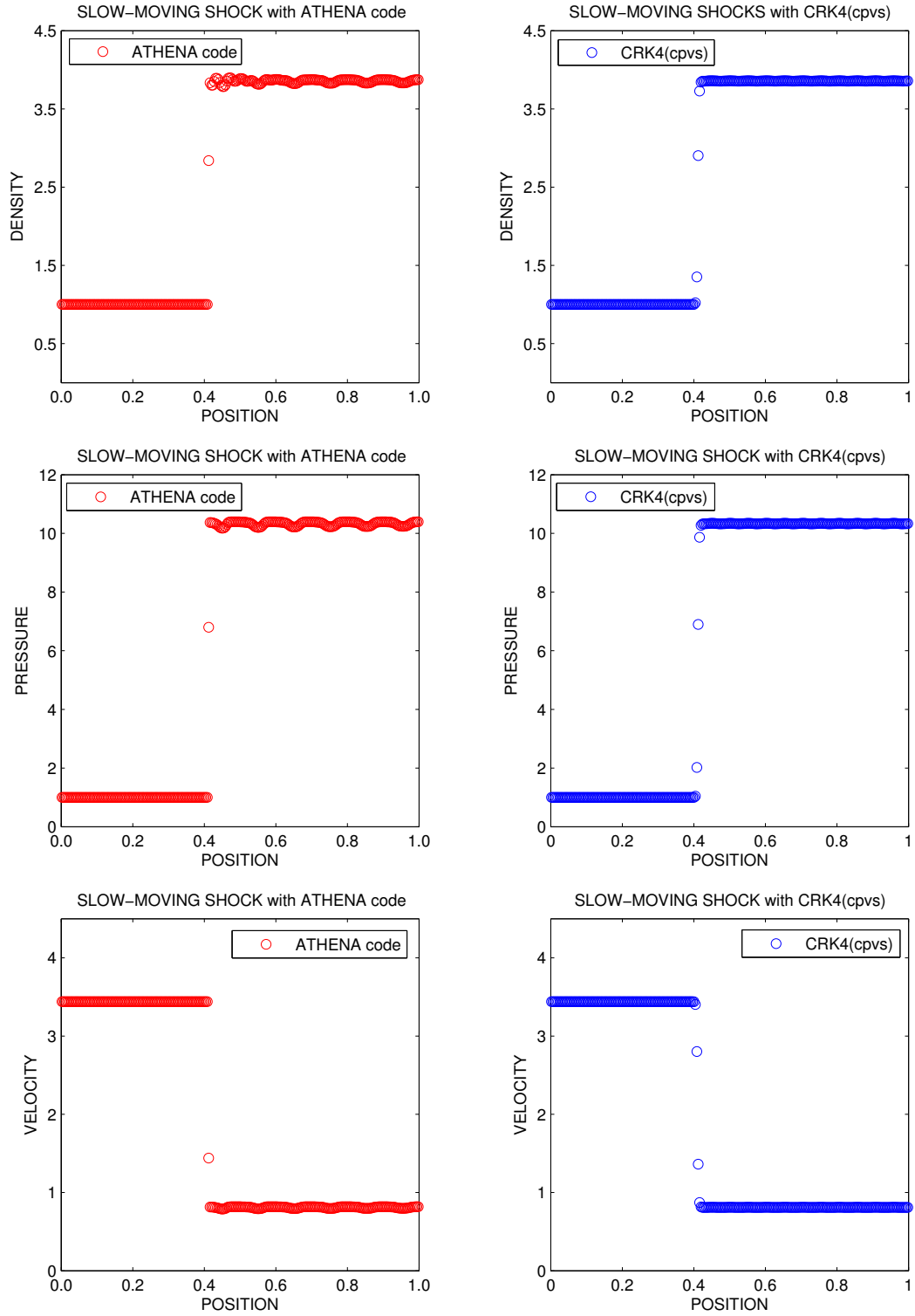


Figure 2.11: Slow-moving shock computed by ATHENA code (Left) and CRK4-CPVS (Right) at time $T = 0.8$ with $N = 256$ grid cells.

2. CWENO SCHEMES FOR SYSTEMS OF CONSERVATION LAWS

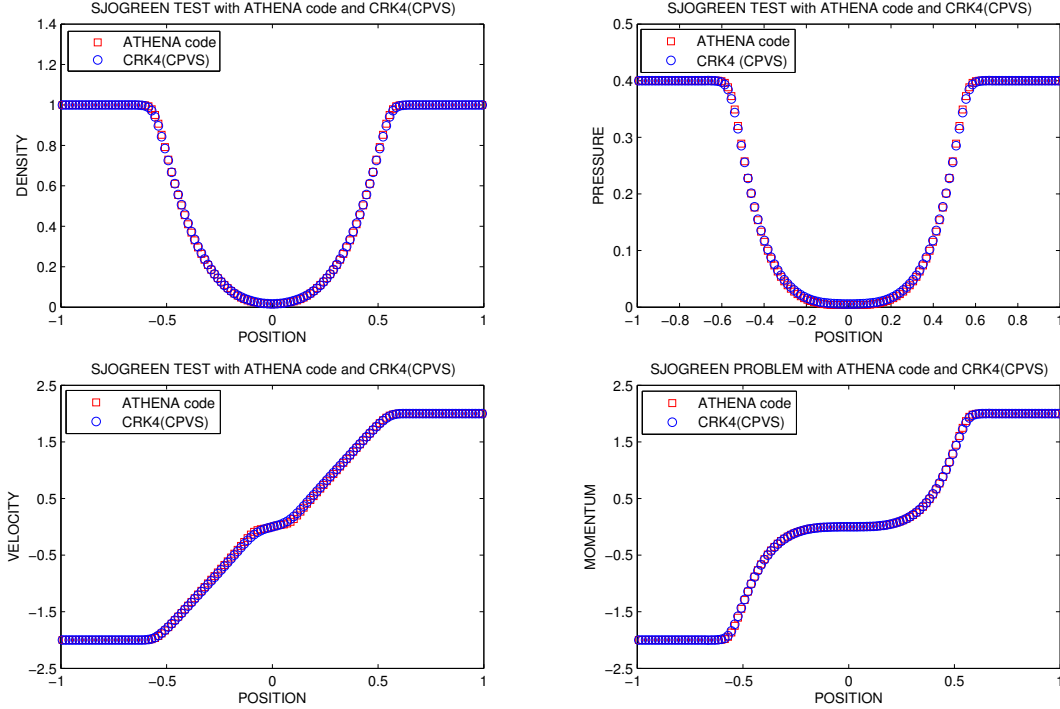


Figure 2.12: Results for the density (*top left*), pressure (*top right*), velocity (*bottom left*) and momentum (*bottom right left*) for the Sjögreen problem of two rarefaction waves traveling outward from the origin, computed using ATHENA code (*Left*) and CRK4-CPVS (*Right*) at time $T = 0.2$. A grid of $N = 128$ points is used.

outflow from the origin, which are typical in many astrophysical systems. To conclude, CRK4-CPVS appears as a competitive approach to resolve the nonlinear hyperbolic system together with the modern widely used astrophysical codes. As we have shown the CWENO high-resolution shock-capturing CRK scheme resolves one dimensional hydrodynamics benchmark test with the same or better accuracy than the integrated finite-volume Godunov-type ATHENA schemes. CRK-CPVS does not require solution of a Riemann problem and its diffusivity due to the central approach, does not affect too much the better performance and does not lead to excess of smearing of the approximated solutions. Most likely such scheme is a very good candidate to be a base of the hydrodynamical algorithms in powerful astrophysical codes, where the scheme has an advantage in the multidimensional applications because of its Riemann-solution-free nature.

2.9 Conclusions

A new strategy of computing the intermediate stages of CRK algorithm in primitive variables has been introduced. The algorithm 2.7.1 represents the new idea integrated in the CRK schemes proposed by (Pareschi et al., 2005). The new method is more efficient than previously developed CWENO (Levy et al., 1999) and CRK especially when it is applied to the nonlinear hyperbolic systems in which the transformation between the primitive and the conservative variables needs solving a high degree transformation equation. The numerical results with the new strategy together with the projection along the characteristic directions reveal oscillation-free and quite efficient method. One of the most successful astrophysical ideal MHD code ZEUS is based on operator splitting of the equations, with higher- order upwind methods used for the advection terms, centered- differencing for the remaining terms, and artificial viscosity for shock capturing. The operator-splitting approach is not conservative. Comparing the results obtained with ZEUS and the new implemented CRK4-CPVS scheme show the advantages of the latter, namely accurate shock-capturing and high-resolution treatment of the discontinuities by full conservative updates of the hydrodynamical variables. The simplicity and the easy implementation of ZEUS algorithms are comparable with the same properties of the adaptive stencil approach in CWENO, however the CWENO scheme enjoy the conservative and accurate properties essential in solving the system of nonlinear conservation laws, for example, (M)HD equations. The numerical tests with ATHENA and CRK4-CPVS are demonstration of the oscillation-free solution in the case of slow moving shocks and two rarefactions moving outward of the origin. The PPM high-order Godunov type algorithm implemented in ATHENA is still not sufficient to reduce the spurious oscillations which arise in the approximate solution of the slow-moving shock, whilst the CRK is capable to achieve oscillation-free solution. Moreover, the excellent performance of the both schemes in positively conservative resolving the configuration of two rarefaction waves, moving outward of the origin, implies that the CRK4-CPVS scheme appears as a reliable candidate for building a new CWENO-type modern astrophysical code in the future.

2. CWENO SCHEMES FOR SYSTEMS OF CONSERVATION LAWS

Chapter 3

Relativistic Hydrodynamics with CWENO schemes

3.1 Introduction

Relativistic hydrodynamics (RHD hereafter) plays a major role in high-energy astrophysical phenomena, for example, in the extragalactic jets from active galactic nuclei (AGN) (see Zensus (1997) for review), in relativistic jets from Galactic micro-Quasars (see Mirabel and Rodríguez (1999) for review), and gamma-ray bursts (see Mészáros (2002) for review) where the relativistic effects are essential and the modeling of such flows involve solution of full relativistic equations of hydrodynamics. Classical fluid dynamics is unable to capture all the physics phenomena produced by the coupling of the space and time in the special and general theory of relativity. Recently, high-resolution shock-capturing finite volume schemes based on the solution of Riemann problem have been applied to the field of special relativistic fluid hydrodynamics (e.g. see Martí and Müller (2003) and Font (2007) for review, Tchekhovskoy et al. (2007) and references therein). Such schemes have been successfully applied in ultra-relativistic regimes where the relativistic effects are mainly presented because of the fundamental relativistic fluid properties such as transformation of the internal energy in relativistic due to the comparable values of the fluid pressure and the mass density, the values of the fluid bulk velocity approaches the speed of light and also the location of the fluid dynamics, which occurs in the vicinity of a compact object like a black hole or neutron star. A variety of numerical codes for special RHD codes have been proposed to the scientific

3. RELATIVISTIC HYDRODYNAMICS WITH CWENO SCHEMES

community, most of them, based on explicit upwind schemes which were originally developed for classical hydrodynamics. These schemes utilize approximate or exact Riemann solvers and the characteristic decomposition of the hyperbolic system of conservation equations and are able to resolve sharp discontinuities robustly in complex flows. Examples of such codes include the van Leer scheme implementation in RHD by Falle and Komissarov (1996) ; Martí and Müller (1996)(hereafter MM),Aloy et al. (1999),Mignone et al. (2005) codes based on the piece-wise parabolic method (PPM) scheme; Sokolov et al. (2001) based on the Godunov scheme; Choi and Ryu (2005) based on the TVD scheme; Dolezal and M.Wong (1995),Donat (1998), Del Zanna and Bucciantini (2002), Rahman and Moore (2005) based on the essentially non-oscillatory (ENO) scheme; and Mignone and Bodo (2005) based on the Harten, Lax, and van Leer (HLL) scheme. Reviews of some numerical approaches and test problems can be found in Martí and Müller (2003) and Wilson and Mathews (2003). The first code to solve the RHD equations on an Eulerian grid was developed by Wilson (1972) and is based on the artificial viscosity and was unable to cope with such ultra-relativistic flows. It coupled explicit finite differencing with a monotonic transport algorithm for the advection terms of the RHD equations. Analogously of ZEUS, the stabilization of the code across shocks is accomplished by means of a von Neumann and Richtmyer artificial viscosity. The strongly relativistic flow (flow Lorentz factor greater than 2) decreases the accuracy of the code. The necessity of capturing the strong shocks involved in the relativistic flows, lead to the increasing scientist's interest of developing modern relativistic HRSC-based hydro-codes. By fully explicit treatment of the equations, Norman and Winkler (1986) overcome the numerical difficulties in ultra-relativistic limit (Lorentz factor much greater than 1). In the last released methods which are trying to resolve the RHD make use of the *conservation form* of the RHD equations. The advantage of using this form of RHD is that all valid numerical techniques designed to solve nonlinear hyperbolic systems of equations can be used in modeling the relativistic hydrodynamic flow. Martí and Müller (1996) discussed that accurate description of ultra-relativistic flows with strong shock waves can be accomplished by writing the system of the RHD in conservation form and using Riemann solvers. Indeed, the authors extended the well-known higher-order Godunov-type piecewise parabolic method Colella and Woodward (1984). The accuracy in PPM method is achieved a parabolic interpolation of variables inside numerical cells and discontinuity steepeners for keeping

the discontinuity sharp and oscillation-free. The use of an exact Riemann solver for averaging over the domain of dependence of the interfaces makes PPM second-order accurate in time. MM extended the PPM in its Eulerian version to one-dimensional RHD. Our aim is by following the formulation of the RHD system of equations used by MM to apply the new conservative-primitive variables strategy CRK algorithm for resolving the nonlinear hyperbolic systems of RHD equations. Our approach enjoys several important advantages in RHD application, which sufficiently could improve the speed and the accuracy for the approximated solution of the RHD system.

- The central approach used in CRK scheme is Riemann-problem-free which results in higher speed of the numerical method, especially in relativistic hydrodynamics, where the solution of Riemann problems multidimensional applications.
- The conversion of the conservative variables into primitive ones in the modeling of relativistic flow is not straightforward as in the system of the classical Euler equations, and hence an algorithm based on advancing in time (precisely, the intermediate stages of the RK method) based on primitive variables is strongly recommended in order to achieve high accuracy and speed. The conservative-primitive variables strategy (CPVS) advances RK steps in primitive variables, and hence there is no need to solve a high-degree equation for one of the primitive quantities expressed by the conservative ones in order to perform the conversion of the conserved variables, at every time step. This strategy speed-up the calculations and to some extent decrease the effect of the expensive mapping between the variables in RHD system of equations.
- One can construct WENO-type schemes of an arbitrary high order that deliver an even higher order when the lower order derivatives vanish; CRK4 is fourth-order CWENO scheme (PPM is based on the second-order Godunov scheme) and is easy to extend to higher order. In addition, the CPVS ensures that in all the intermediate stages of the Runge-Kutta predictor step are calculated in primitive variables without conversion between the variables within the iterations. Therefore, by constructing higher order CRK scheme (i.e. the number of the iteration in the predictor step) we keep the property of no conversion between the conservative and primitive variables. The latter does not increase the complexity and the robustness of the CRK scheme.

3. RELATIVISTIC HYDRODYNAMICS WITH CWENO SCHEMES

The chapter is organized as follows. In Section 3.2 a brief overview of the relativity concept and comment on the computational difficulties, which one can face when solve the relativistic hydrodynamics equations has been done. We define the RHD equations in an Eulerian reference frame in conservation form and describe the transformation of the quantities from the Eulerian frame to the rest (proper) frame of a fluid element. We end the section, introducing the characteristic decomposition needed to determine the characteristic speeds for updating the time step in the CRK4-CPVS algorithm and for the projection along the characteristic directions 2.6.2 strategy. Further, Section 3.3 describe the application of CRK4-CPVS algorithm 2.7.1 to the RHD equations. Results obtained by applying the first-order finite-volume scheme to RHD are presented in the beginning of Section 3.4. The same section contains the results of several quintessential numerical test calculations, including the relativistic shock-tube problems, which were used to benchmark the RHD algorithm. A Section 3.5 of conclusions and future work ends this chapter.

3.2 The equations of relativistic hydrodynamics (RHD)

Albert Einstein with his special theory of relativity changed the way in which the scientists think about space and time. The Newtonian definition of absolute time is replaced with a concept of the relative passage of time. Two different observers in spacetime need not agree on the passage of time between the same events. The special theory of relativity is based on two principles: (1) no experiment can measure the absolute speed of a spacetime observer and (2) the speed of light is universal constant. Special relativity it is inconsistent with a Newtonian theory of gravity in which the field propagates with infinite speed. With the general theory of relativity, introduced by Einstein in 1915, insures local consistency with the special theory of relativity with the so-called equivalence principle, which says that in a neighborhood of each event in spacetime, physical laws take on their special relativistic form. The latter enables to solve general relativistic Riemann problems using locally special relativistic frames. The Einstein equations governing the dynamics of the gravitational field in the presence of matter can be written in the following elegant form

$$G_{\mu\nu} = 8\pi T_{\mu\nu}. \quad (3.1)$$

3.2 The equations of relativistic hydrodynamics (RHD)

Both the Einstein tensor, $G_{\mu\nu}$, and the energy momentum tensor $T_{\mu\nu}$ are a second rank symmetric tensor in four dimensions (one time-like and three space-like) and the Einstein one determines the spacetime metric and its derivatives, while $T_{\mu\nu}$ contains information about the electrodynamic and hydrodynamic fields. The equations (3.1) are a system of ten nonlinear partial differential equations in one time-like variable, and three spatial variables and describe the mechanism of how the matter generates the spacetime curvature and how the latter modifies the flow of matter. In order to solve the Einstein system of equations, one must turn to the numerical approximations.

The motion of a relativistic fluid is governed by the local conservation of both matter and energy-momentum. Using the Einstein summation convention these five conservation laws are given by the following equations:

$$\begin{aligned}(\rho v^\mu)_{;\mu} &= 0, \\ T^{\mu\nu}_{;\nu} &= 0,\end{aligned}$$

where $\mu, \nu = 0, \dots, 3$ and where $;\mu$ denotes the covariant derivative with respect to coordinate x^μ . The other quantities are the proper rest mass density of the fluid, ρ , the four-component velocity, v_μ , and the stress-energy tensor, $T^{\mu\nu}$, which for a perfect fluid has the form

$$T^{\mu\nu} = \rho h v^\mu v^\nu + p g^{\mu\nu}.$$

Here, $g_{\mu\nu}$ is the metric tensor, p the fluid pressure and h the specific enthalpy of the flow is defined by

$$h = 1 + \varepsilon + \frac{p}{\rho}, \tag{3.2}$$

where ε is the specific internal energy. The speed of light is $c=1$, since the natural units are considered. These equations are closed by the normalization of the four velocity $v^\mu v_\mu = -1$. Here, we do not derive the conservations form of these equations, but nevertheless it is worth noting one of difficulties which one can avoid by the proper choice of the conservative variables. The mass and energy are proportional in the relativity theory (Einstein's famous $E = mc^2$) with the very large constant $c^2 \sim 10^{17} m^2/s^2$. Therefore, the energy is dominated by the rest mass contribution. The relative size of the mass contribution makes very difficult to determine the contribution of the fluid's

3. RELATIVISTIC HYDRODYNAMICS WITH CWENO SCHEMES

thermodynamic energy at a given moment. Then, numerically, is more reasonable to consider an energy perturbation (hereafter denoted by $\tau = E - D$, with E for the relativistic energy and D is the relativistic mass density) as a conservative relativistic variable when we write the RHD in conservation form than the energy itself, provided with the use of the natural units, $c = 1$. It means that the rest mass energy as measured by the observer has being removed.

In the following we review the formulation of the one-dimensional RHD as it is presented in MM and use this formulation of the RHD equations in the implementation of our CRK4-CPVS scheme. We consider Eulerian reference frame and perfect fluid. The equations of RHD of a perfect fluid in one spatial(Cartesian) coordinate x , can be written in conservative form as

$$\begin{aligned}\frac{\partial D}{\partial t} + \frac{\partial Dv}{\partial x} &= 0 \\ \frac{\partial S}{\partial t} + \frac{\partial(Sv + p)}{\partial x} &= 0 \\ \frac{\partial \tau}{\partial t} + \frac{\partial(S - Dv)}{\partial x} &= 0\end{aligned}\tag{3.3}$$

where D , S and τ are the rest-mass density, the momentum density, and the energy density in a fixed frame, respectively. The relationship between the conserved and the primitive variables, i. e. the quantities in local rest frame for this system, is

$$\begin{aligned}D &= \rho W \\ S &= \rho h W^2 v \\ \tau &= \rho h W^2 v - p - D,\end{aligned}\tag{3.4}$$

where ρ , p , h , W and v are the proper rest-mass density, the pressure, the specific enthalpy 3.2, the fluid Lorentz factor, and the fluid velocity, respectively. The speed of light is set equal to zero and the Lorentz factor is given by

$$W = \frac{1}{\sqrt{1 - v^2}}.\tag{3.5}$$

In the non-relativistic limit ($v \ll 0$, $h \rightarrow 1$) D , S , and τ approach their Newtonian counterparts, ρ , ρv , and E and the system is reduced to the classical gas dynamics one 2.41. In the relativistic case, however, the equations of system 3.3 are nonlinearly

3.2 The equations of relativistic hydrodynamics (RHD)

coupled via the Lorentz factor and the specific enthalpy, which lead to numerical difficulties, especially when $W > 1$. In fact, the solution of Riemann problems in most hydrodynamical codes involves using primitive variables of the system, for example, the natural ones we used, ρ, v, p . The algebraic relationship for a classical inviscid perfect gas has the simple form, given in (2.49). It is trivially inverted. This can not be said for the case of the relativistic hydrodynamics. An iterative procedure is needed to obtain one of the primitive variables (usually, the velocity or the pressure) performed at each time step. We follow the procedure proposed by MM for an equation of state for a perfect gas, which close the system (3.3), i. e. in the form

$$p = (\gamma - 1)\rho\varepsilon,$$

where γ is the adiabatic index. Then the sound speed c can be defined through

$$c^2 = \frac{\gamma p}{\rho h}.$$

Evolving the conserved variables $\{D, S, \tau\}$ in time requires the variables $\{\rho, v, \varepsilon, p\}$ to be computed from the conservative variables once per time step. Martí and Müller (1996) use the following procedure:

(1) Define a function for the pressure

$$f(\tilde{p}) = \tilde{p} - (\gamma - 1)\rho_*(\tilde{p})\varepsilon_*(\tilde{p}), \quad (3.6)$$

(2) Using the equations for the variables (3.4) one has the velocity in the following form:

$$v = \frac{S}{\tau + D + p}, \quad (3.7)$$

Then one can compute a W_* based on the velocity

$$W_* = \frac{1}{\sqrt{1 - (S/(\tau + D + p))^2}},$$

(3) Use W_* to compute

$$\begin{aligned} \rho_* &= \frac{D}{W_*}, \\ \varepsilon_* &= \frac{\tau + D(1 - W_*^2) + \tilde{p}(1 - W_*^2)}{DW_*}. \end{aligned}$$

3. RELATIVISTIC HYDRODYNAMICS WITH CWENO SCHEMES

Some remarks on finding the zero of $f(\tilde{p})$ worth being mentioned. Note that since the velocity in our units is $|v| \leq 1$ one can evaluate the lower bound of the physically allowed domain $p \in (p_{min}, \infty)$

$$p_{min} = |S| - \tau - D.$$

The monotonicity of the function $f(\tilde{p})$ in that domain ensure the uniqueness of the solution. The root of the above function can be obtained by means of a nonlinear root-finder (e.g. a Newton-Raphson method, bisection method or false-position method). Solving this pressure equation at each time step sufficiently increase the computational time of our algorithm 2.7.1. Even the advantage of the conservative-primitive variables strategy of no need of inversion of the variables in the intermediate stages does not compensate the time-consuming and necessary computation of the pressure equation at least one time per time step. In our CRK algorithm it has to be done twice per time step: once for inverting the reconstructed conservative pointwise values into the primitive ones and second solving the pressure equation (3.6) is needed in the evaluation of the characteristic speeds (i.e. the eigenvalues) used in the calculation of the time step. Further discussion on the performance of the algorithm (2.7.1) can be found in the next section.

Another approach has been proposed by Ryu et al. (2006) based on the estimations on the analytical solution of an quartic equation for velocity Schneider et al. (1993). In his study on the proper equation of state (EOS), Ryu et al. (2006) use the approach introduced by Schneider et al. (1993), namely, that the one-dimensional RHD with EOS for the perfect gas is reduced to a single quartic equation for u . This quartic equation can be solved numerically or analytically. The general form of analytical roots for quartic equations can be found in Abramowitz and Stegun (1972). The roots can be found using software such as Mathematica or MATLAB. In the consequent discussion the authors exclude the complex roots and among the real ones only one satisfies the upper and lower limits imposed by Schneider et al. (1993). Then, the relations of the others quantities in 3.3 can be expressed trivially.

In the present work, we have made tests with both strategies for converting the conservative variables, i.e. one by solving an a quartic equation for velocity and the other by solving a quartic equation for the pressure. The choice of solving an quartic

3.3 CRK scheme in relativistic hydrodynamics

equation for the pressure provide us the same framework, which most of the one-dimensional upwind-based RHD codes nowadays follow, and hence, any improvement of the numerical tests can be considered mainly due to the design of the scheme than of the diversity in the modeling of the RHD equations.

The first relation in 3.4 together with the Lorentz factor expression and the ideal EOS (3.6) can be plugged in the second and the third and the fourth relation in 3.4. Using simple algebraic transformations it is possible to eliminate one of the two unknown variables in the modified coupled third and fourth relations in 3.4, yielding a fourth-order polynomial for the remaining variables. Thus, we solve analytically a quartic equation for pressure.

Excluding the complex roots and checking the relativistic velocity condition $|v| \leq 1$ to be fulfilled we determine the pressure. We used Mathematica software to calculate the roots of the quartic pressure equation.

3.3 CRK scheme in relativistic hydrodynamics

In Section 2.7.1 we introduced the CRK algorithm with conservative-primitive variables strategy included for the systems of hyperbolic conservation laws. In order to apply the algorithm to the relativistic hydrodynamics, one must implement the inversion relations between the conservative and primitive variables for the RHD equations, given in 3.4. The implementation of the mapping from conservative to primitive is done in the following simple procedure:

- (1) Compute the pressure from the pressure equation, 3.6, i.e. use the analytical solution p computed in the conserved variables $\{D, S, \tau\}$.
- (2) Compute the velocity u through the relation 3.7.
- (3) Use velocity to compute the Lorentz factor W (3.5).
- (4) Use the Lorentz factor to compute the density, i.e. $\rho = D/W$.
- (5) Form the vector of the primitive variables $(\rho, v, p)^T$. The reverse inversion, from primitive to conservative needed in the corrector step (see Step 8 in the algorithm 2.7.1) for updating the staggered cell averages in conservative variables is trivial and is given by the relationship 3.4 and the Lorentz factor W (3.5).

Non-conservative Jacobian in relativistic hydrodynamics The computation of

3. RELATIVISTIC HYDRODYNAMICS WITH CWENO SCHEMES

| Eigenvalues | Left eigenvectors | Right eigenvectors |
|------------------------------------|--|---|
| $\lambda_- = \frac{v - c}{1 - vc}$ | $\mathbf{l}_- = \left(0, \frac{1}{2}, -\frac{1}{2\rho h W^2 c}\right)$ | $\mathbf{r}_- = \left(-\frac{\rho W^2}{c}, 1, -\rho h W^2 c\right)$ |
| $\lambda_0 = v$ | $\mathbf{l}_0 = \left(1, 0, -\frac{1}{hc^2}\right)$ | $\mathbf{r}_0 = (1, 0, 0)$ |
| $\lambda_+ = \frac{v + c}{1 + vc}$ | $\mathbf{l}_+ = \left(0, \frac{1}{2}, \frac{1}{2\rho h W^2 c}\right)$ | $\mathbf{r}_+ = \left(\frac{\rho W^2}{c}, 1, \rho h W^2 c\right)$ |

Figure 3.1: Spectral decomposition of the non-conservative Jacobian J in relativistic hydrodynamics. Taken from Martí and Müller (1996)

the intermediate states in the predictor step (Step 5) of the algorithm 2.7.1 requires computation of the non-conservative Jacobian of the RHD system. The latter can be written in the following form (Martí and Müller (1996))

$$J = \begin{pmatrix} v & \frac{\rho}{1 - v^2 c^2} & \frac{-v}{h W^2 (1 - v^2 c^2)} \\ 0 & \frac{v(1 - c^2)}{1 - v^2 c^2} & \frac{1}{\rho h W^4 (1 - v^2 c^2)} \\ 0 & \frac{\rho h c^2}{1 - v^2 c^2} & \frac{v(1 - c^2)}{1 - v^2 c^2} \end{pmatrix} \quad (3.8)$$

For the sake of completeness and simplicity in the notation for the characteristic speeds, the local sound speed c has explicitly been introduced in the matrix J . Besides the use of the matrix in the computation of the intermediate stages, the non-conservative Jacobian serves to calculate the eigenvalues sets $\{\lambda_-, \lambda_0, \lambda_+\}$. The spectral decomposition of J is given in Figure 3.1. Therefore, the evaluation of the eigenvalues which is necessary in Step 2 - 4 in the algorithm 2.7.1 is based on the calculation of the maximum value of λ among

$$\lambda_- = \frac{v - c}{1 - vc}, \quad \lambda_0 = v, \quad \lambda_+ = \frac{v + c}{1 + vc}.$$

Dolezal and M.Wong (1995) commented that the last in the line, λ_+ , has the maximum size. Hence, the computation of the spectral radius is reduced to the computation of the latter value at each time step. Two remarks of the application the CRK4-CPVS method to the relativistic approach worth noting:

Remark 1 In the algorithm 2.7.1 nowhere is needed the computation of the non-conservative Jacobian J separately, i.e. J is updated in the intermediate stages always in the combination of the derivative of the primitive variables. Then, a component-by-component multiplication of the coupled terms is sufficient to be implemented in the code. This property of CPVS results in higher speed of the CRK4-CPVS algorithm.

Remark 2 Our numerical tests show that the most expensive part of the algorithm is the inversion between the conservative and primitive variables and the computation of the adaptive time step, which involves evaluation of the characteristic speeds at each time step of the algorithm. We found that for the relativistic test problems where the characteristic speed do not change abruptly with time(e. g. the first Sod shock-tube problem), a fixed mesh ratio provided with the stability conditions for the scheme can be used. For the the fourth-order CRK scheme linear stability analysis gives the value $\lambda_0 = 0.48$ (see 2.40 ,Section 2.4).

3.4 Numerical results

Shock tubes problems are among the traditional numerical tests which have been used to benchmark the RHD code. The reason of their popularity is based on their evolution in time. As it has been shown in the case of gas dynamics in Section 2.6 and 2.8, shock tubes problem give rise not only of strong shock waves, but also of rarefaction waves. The shock tubes represent special class of Riemann problems with piecewise constant fluid states on each side of imaginary membrane. The membrane is removed at time $T = 0$ and the initial data decays into waves, propagating away from the surface. We have simulated a particular shock tube problem with the following initial state:

Relativistic shock-tube problem

(a high-pressure, dense gas on the left expands into a less dense gas at low pressure)

$$\begin{aligned} (\rho_l, v_l, p_l) &= (10.0, 0, 13.3) & x < 0.5 \\ (\rho_r, v_r, p_r) &= (1.0, 0, 0.0) & x > 0.5 \end{aligned} \tag{3.9}$$

First, we test this two problems against the first-order CRK scheme, which can be

3. RELATIVISTIC HYDRODYNAMICS WITH CWENO SCHEMES

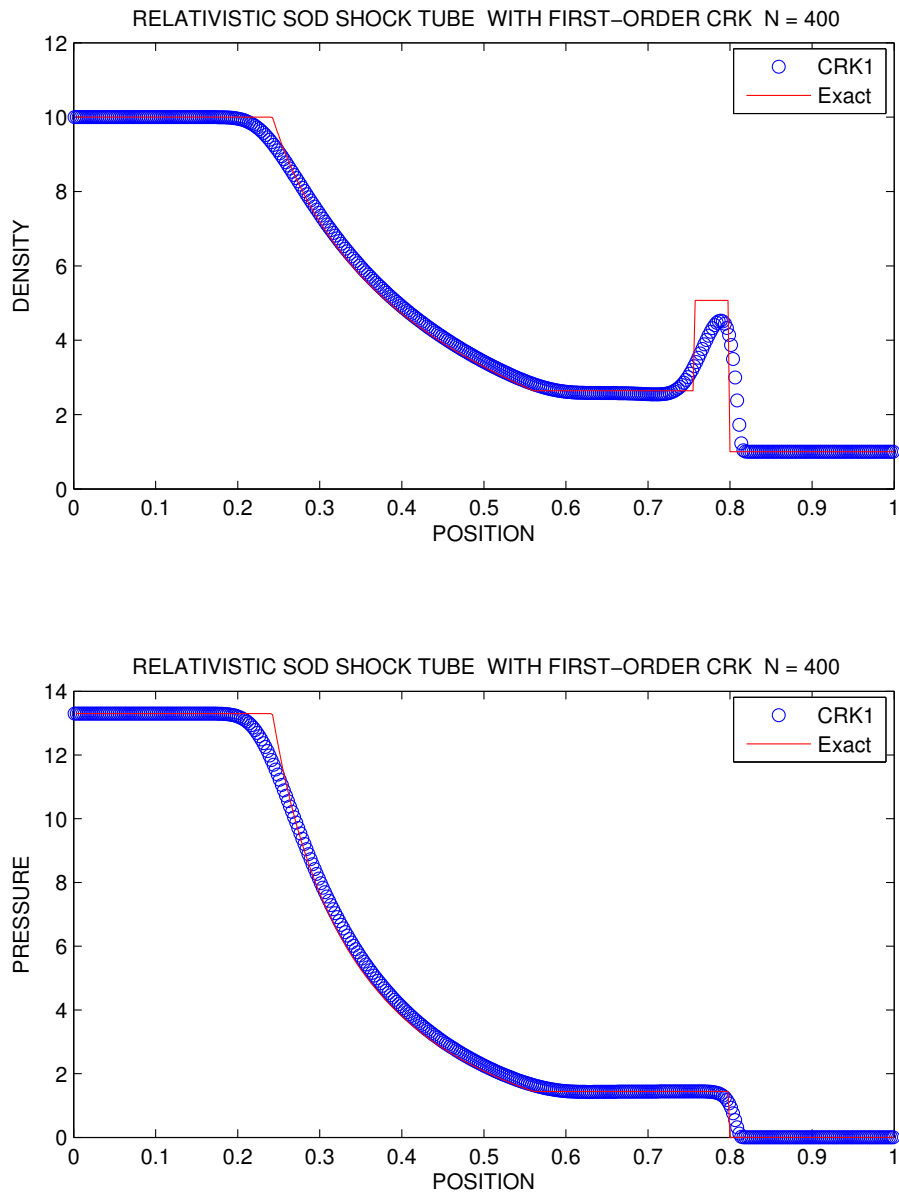


Figure 3.2: Exact and numerical profiles of density (top) and pressure (bottom) of a relativistic shock-tube problem, performed at uniform grid of $N = 400$ cells.

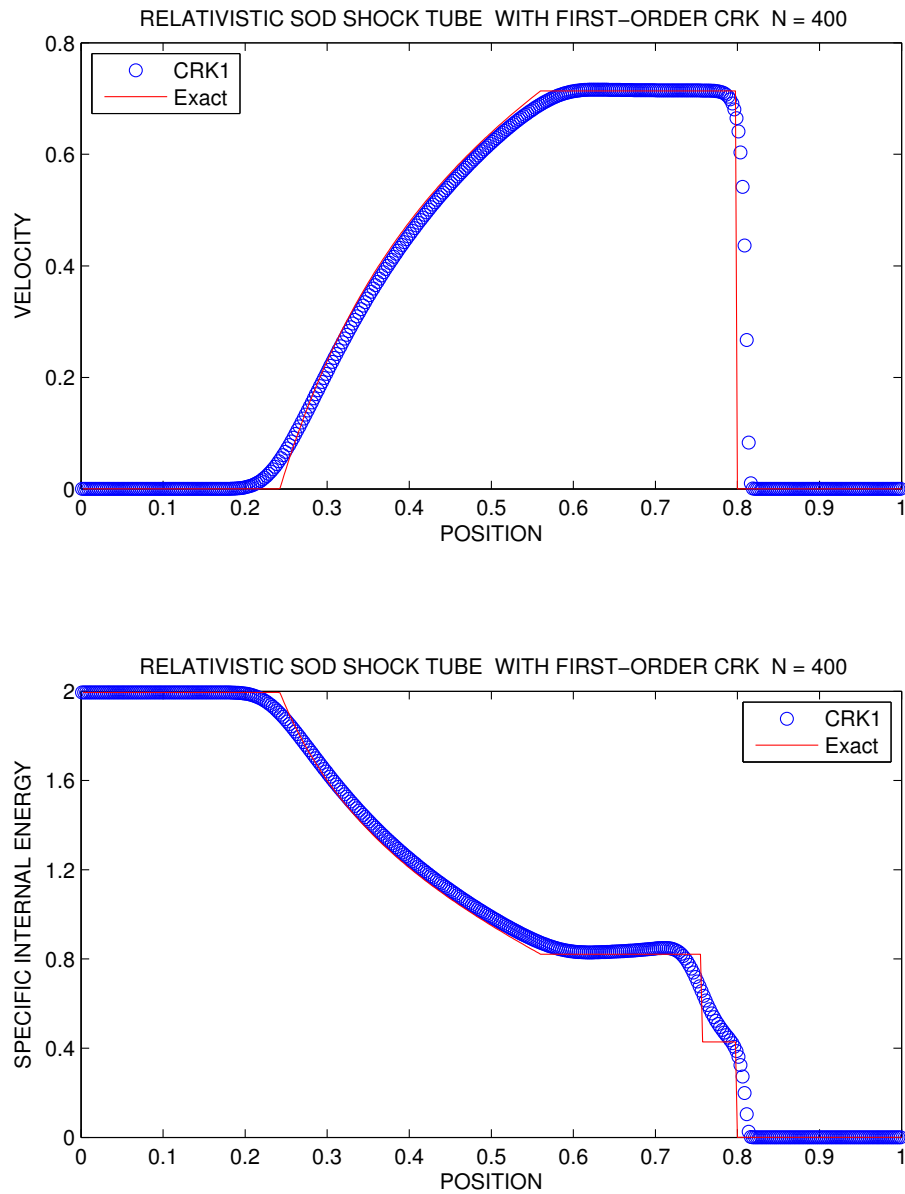


Figure 3.3: Exact and numerical profiles of flow velocity (top) and specific internal energy (bottom) of a relativistic shock-tube problem, performed at uniform grid of $N = 400$ cells.

3. RELATIVISTIC HYDRODYNAMICS WITH CWENO SCHEMES

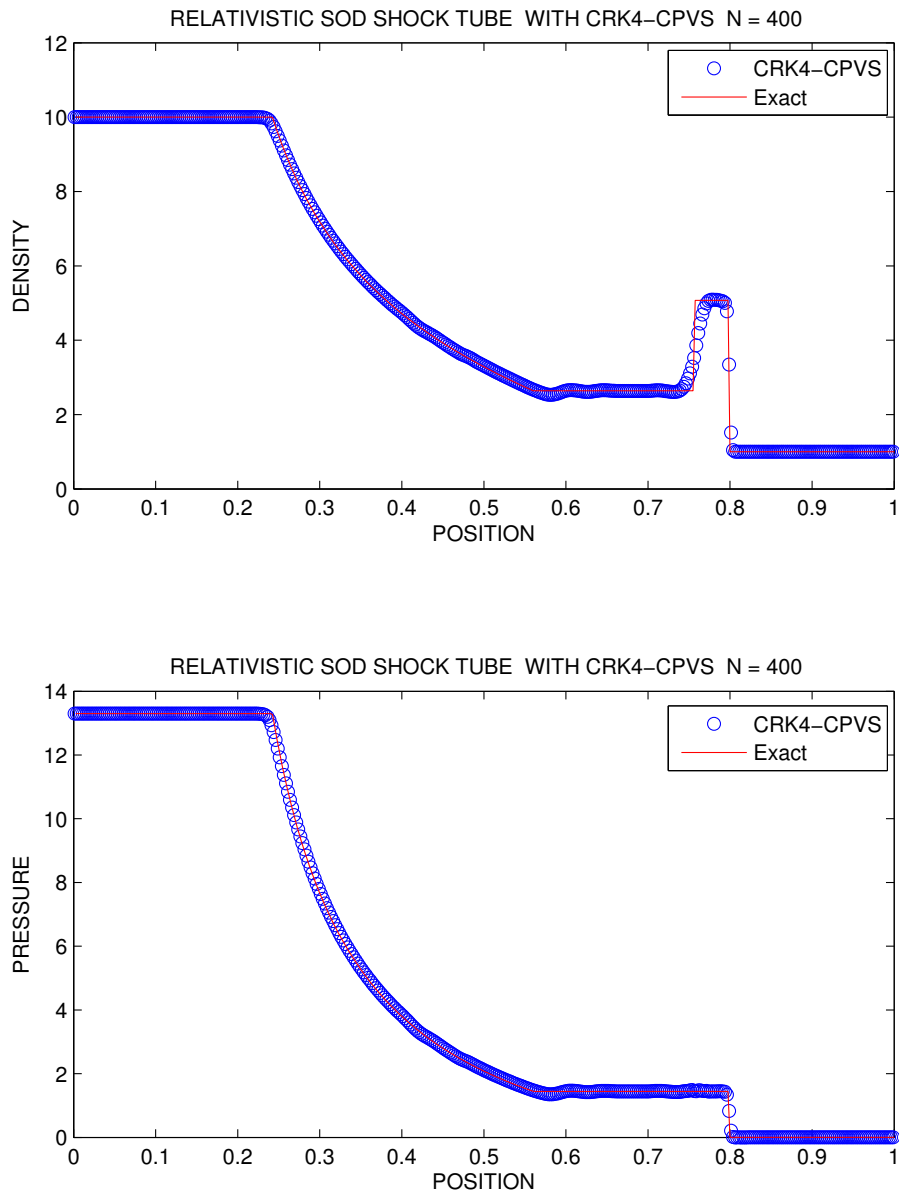


Figure 3.4: Exact and numerical profiles of density (top) and pressure (bottom) of a relativistic shock-tube problem, performed at uniform grid of $N = 400$ cells.

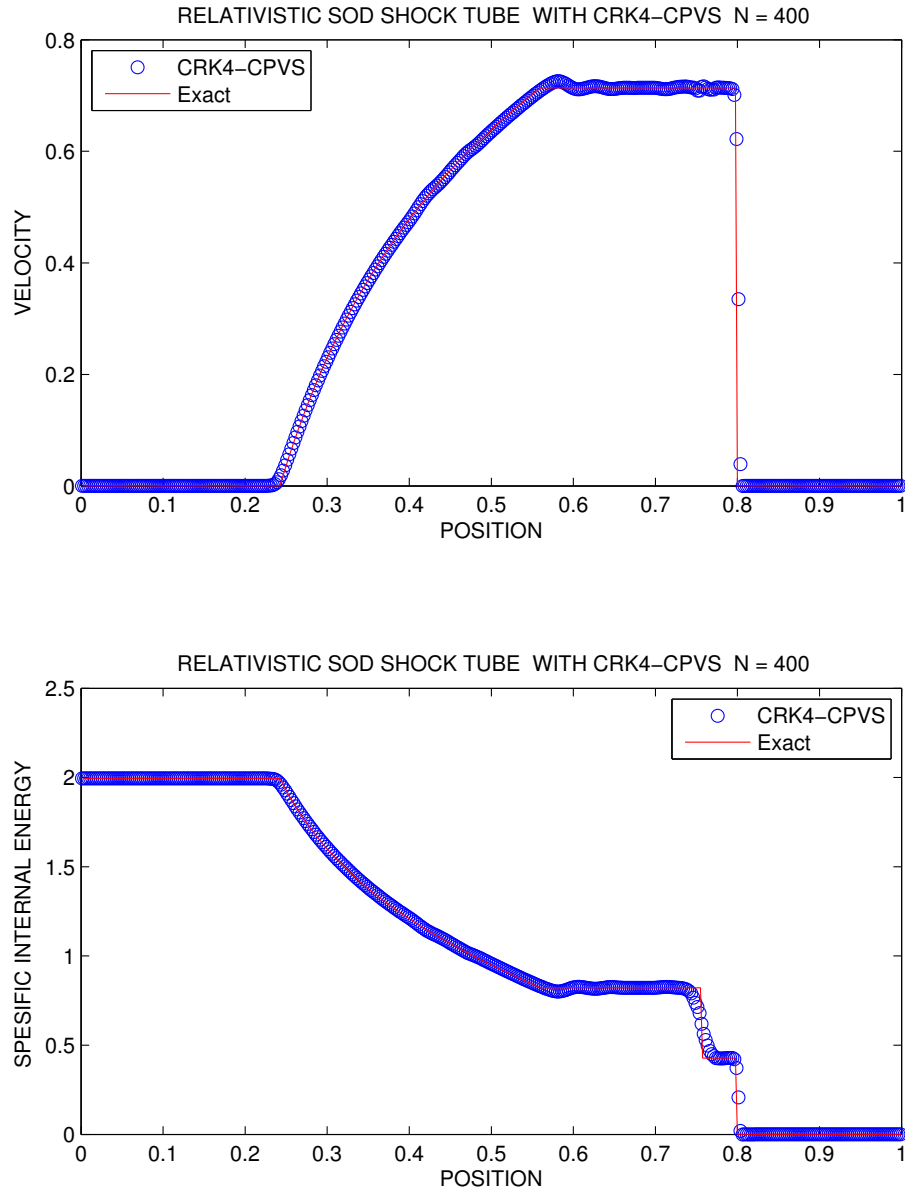


Figure 3.5: Exact and numerical profiles of flow velocity (top) and specific internal energy (bottom) of a relativistic shock-tube problem, performed at uniform grid of $N = 400$ cells.

3. RELATIVISTIC HYDRODYNAMICS WITH CWENO SCHEMES

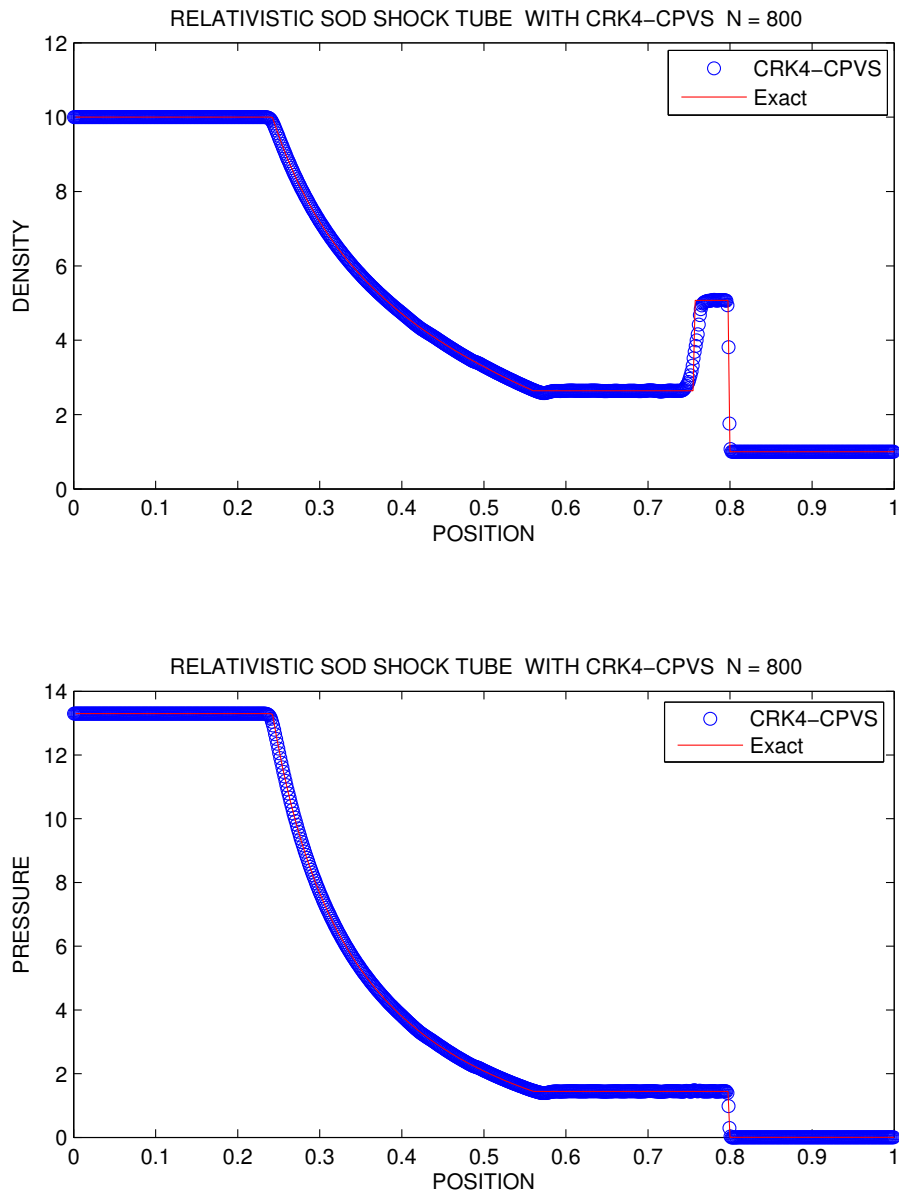


Figure 3.6: Exact and numerical profiles of density (top) and pressure (bottom) of a relativistic shock-tube problem, performed at uniform grid of $N = 800$ cells.

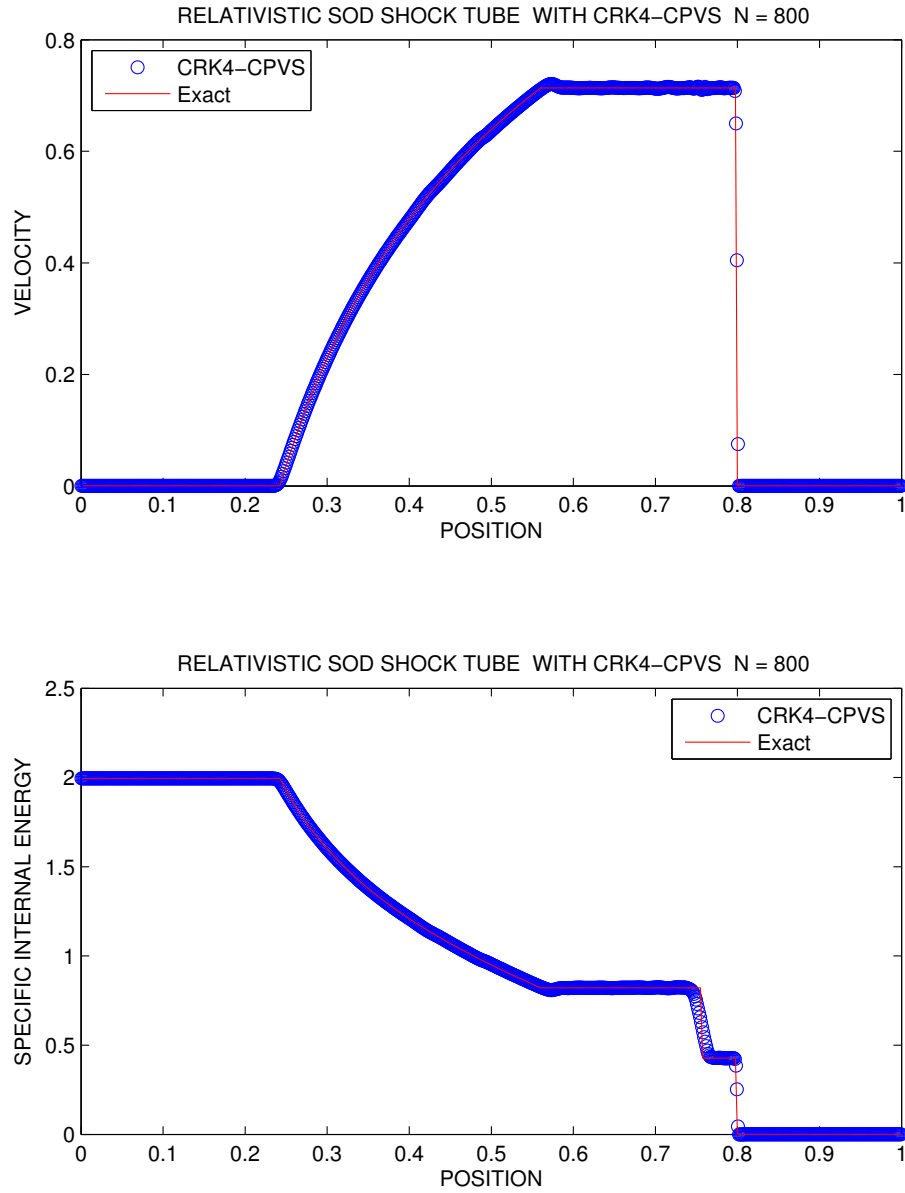


Figure 3.7: Exact and numerical profiles of flow velocity (top) and specific internal energy (bottom) of a relativistic shock-tube problem, performed at uniform grid of $N = 800$ cells.

3. RELATIVISTIC HYDRODYNAMICS WITH CWENO SCHEMES

written as a finite volume Lax-Friedrichs scheme for evolving cell averages, namely:

$$\begin{aligned}
 (1) \quad & u_j = \bar{u}_j \\
 (2) \quad & \bar{u}_{j+1/2} = \frac{u_j + u_{j+1}}{2} \\
 (3) \quad & \bar{u}_{j+1/2}^{n+1} = \frac{1}{2}(\bar{u}_j^n + \bar{u}_{j+1}^n) - \lambda(f(\bar{u}_{j+1}^n) - f(\bar{u}_j^n)),
 \end{aligned}$$

where \bar{u}_j are the cell averages and u_j are the pointwise values of the solution. Figure 3.2 - 3.3 show the density, velocity and the pressure profiles at a uniform grid of 400 cells. We have used the Riemann exact solver of Martí and Müller (2003) for computing the exact solution. One can observe the strong diffusivity of the first-order CRK scheme, but its robustness and oscillation-free approximate solution as well. In all the the relativistic numerical tests the adiabatic index is $\gamma = 5/3$, the the initial discontinuity is located at $x = 0.5$ and the results are plotted at time $T = 0.36$.

In the second and the third tests, we have applied the fourth- order CRK scheme with conservative-primitive variables strategy (CRK4-CPVS) to the relativistic hydrodynamics. The series of four figures in Figure 3.4 - 3.5 show the results of the density, pressure, velocity and the specific internal energy, respectively for eulerian mesh of 400 grid points. The decay of the initial discontinuity spreads out between a shock wave and a rarefaction wave. The new CRK4-CPVS methods compares well with those discussed in the literature, for example, see Martí and Müller (2003) and Dolezal and M.Wong (1995).The strong rarefaction wave has been captured accurately, and the sock wave in the velocity is captured within two grid cells. We observe small-amplitude oscillations in the profiles, more clearly registered in the velocity profile. In the consequent figures Figure 3.6 and 3.7 we repeat the numerical but with double number of grid cells, i.e. $N = 800$. Since the oscillations are dumped with increasing the resolution, i.e. ENO-type oscillations, successfully application of the projection along the charactereristic directions strategy, introduced in Section 2.6.2 make the evolution of the numerical solutions in relativistic hydrodynamics oscillation-free. The strong shock capturing of the specific internal energy attract special interest due to the evolving of a very close located rarefaction (*left*), discontinuity (*middle*) and the shock (*right*) wave. Our numerical results show better accuracy than, for example, those obtained by recent modern relativistic code WHAM Tchekhovskoy et al. (2007).

3.5 Conclusions

We have applied the new method combining the high-order CWENO Runge-Kutta scheme with the conservative-primitive variables strategy to obtain numerical solutions to the equations of relativistic hydrodynamics of a perfect fluid. The CRK-CPVS algorithm is applicable to any number of space dimensions and arbitrary equation of state. The Riemann-solver-free approach of the CRK-CPVS scheme is essential for the multidimensional problems of relativistic hydrodynamics. Multidimensional finite volume Godunov-type algorithms rely on the solution of one dimensional Riemann problems normal to each grid interface. For the classical Eulerian equations such suggestion works fine due to the fact that the Riemann solution is completely determined by the fundamental variables density, pressure and normal velocity. The transverse velocity is constant through all normal shock and rarefaction waves. In the case of RHD the coupling between the normal and the transverse directions is conditioned by the presence of the Lorentz factor W . The transverse velocities are not constant through the shock and rarefaction waves in the relativistic one-dimensional Riemann problems (see Balsara (1994)). Then the central approach seems very adequate to be applied to RHD. In addition, CRK4-CPVS is higher-order and diffusive, which in multidimensional applications has a key role for the robustness and stability of used numerical scheme. We made numerical test with CRK4-CPVS and found consistently good results. Because of the high resolution, the CRK4-CPVS scheme provide an effective approach for numerical simulations of relativistic shock blast waves and relativistic nuclear collisions.

3. RELATIVISTIC HYDRODYNAMICS WITH CWENO SCHEMES

Chapter 4

Non-linear 3D simulations of current-driven instabilities in jets

4.1 Introduction

Magnetic fields are an essential ingredient to understand the physics of jets. While polarization observations provide information on the orientation and degree of the order of the magnetic field which seems to be highly organized in many jets (see, e.g., Cawthorne et al. (1993), Leppanen et al. (1995), Gabuzda (1999), Gabuzda et al. (2004), Kharb et al. (2008)) recent observations of a radio jet in the galaxy CGCG 049-033 also reveal the presence of a predominantly toroidal magnetic field Bagchi et al. (2007). It appears that this interpretation offers a more natural explanation because the observed field structure is transverse all along the jet, remaining transverse even while the jet bends.

A variety of MHD instabilities can occur in magnetized astrophysical bodies where they play an important role in enhancing transport processes and in the evolving of various structures obtained by the interaction in the poloidal-toroidal magnetic field configurations, typically encountered in any astrophysical phenomena. Some important MHD instabilities are recognizable in the astrophysical context of jet formation from active galactic nuclei (AGN) and young stellar object (YSO). The MHD Kelvin Helmholtz instability, likewise its hydrodynamical counterpart, has for a driving agent, the velocity gradient at the interface between the jet and the external medium. The instability comes from the fact that the largest source of free energy in a jet is its bulk motion (Ferrari (1998)). Conversely, the presence of magnetic field provides source of in-

4. 3D SIMULATIONS OF MHD INSTABILITIES IN JETS

stability even in the lack of bulk velocity. Ideal MHD instabilities are typically divided into current- and pressure- driven ones. The driving factor in the current-driven case is an equilibrium parallel current, while in the pressure-driven case is gas pressure versus field-line curvature. Radiative instabilities are result of the coupling of the radiation field and of the plasma dynamical quantities. Here, we investigate one of these most prominent MHD instability, namely, the current-driven (pinch-type) instability of a purely toroidal field which typically proceeds through almost horizontal displacements. In fact, ever since the paper by Tayler (1973), it has been known that toroidal fields can be unstable close to the axis of symmetry, if there is a non-zero electric current density on the axis. The growth rate of this instability is expected to be of the order of the time taken for an Alfvén wave to travel around the star on a toroidal field line. The onset of instabilities can be caused both by stretching hydrodynamic motions or properties of the magnetic configurations. Tayler instability remain the dominant one even in the physical situations where, for example, the inclusion of differential rotation (Rüdiger et al. (2007), Gellert et al. (2008)), or of a relatively weak poloidal field (Howard and Gupta (1962), Knobloch (1992), Bonanno and Urpin (2008)), alters the stability properties of the system substantially. In these cases, the Alfvén frequency in the azimuthal direction $\omega_{A\phi}$ is greater than the inverse characteristic timescale of differential rotation. Then the relevant question is to understand what stable-field configuration can be realized in such context.

The structure of jets is not precisely known and most stability analyzes assume that the jets can be described as a cylindrical magnetic column in motion, with the azimuthal component of the magnetic field dominating over the vertical one in the outer jet regions, since the magnetic tension is the confining force ensuring self-collimation. Colour composite image of Centaurus A, revealing the lobes and jets emanating from the active galaxy's central black hole is shown in Figure 4.1. A cartoon image of formation of extragalactic jet is presented in Figure 5.1. While in astrophysical jets the non-linear development of the current-driven instability has been analyzed by Lery et al. (2000) who found that this instability can modify the magnetic structure of a jet mainly redistributing the current density in the inner part, recent works by Bonanno and Urpin (2008) suggests that in the presence of vertical field the spectrum of the unstable modes can be very complicated, and only a sufficiently strong vertical field can stabilize the system.

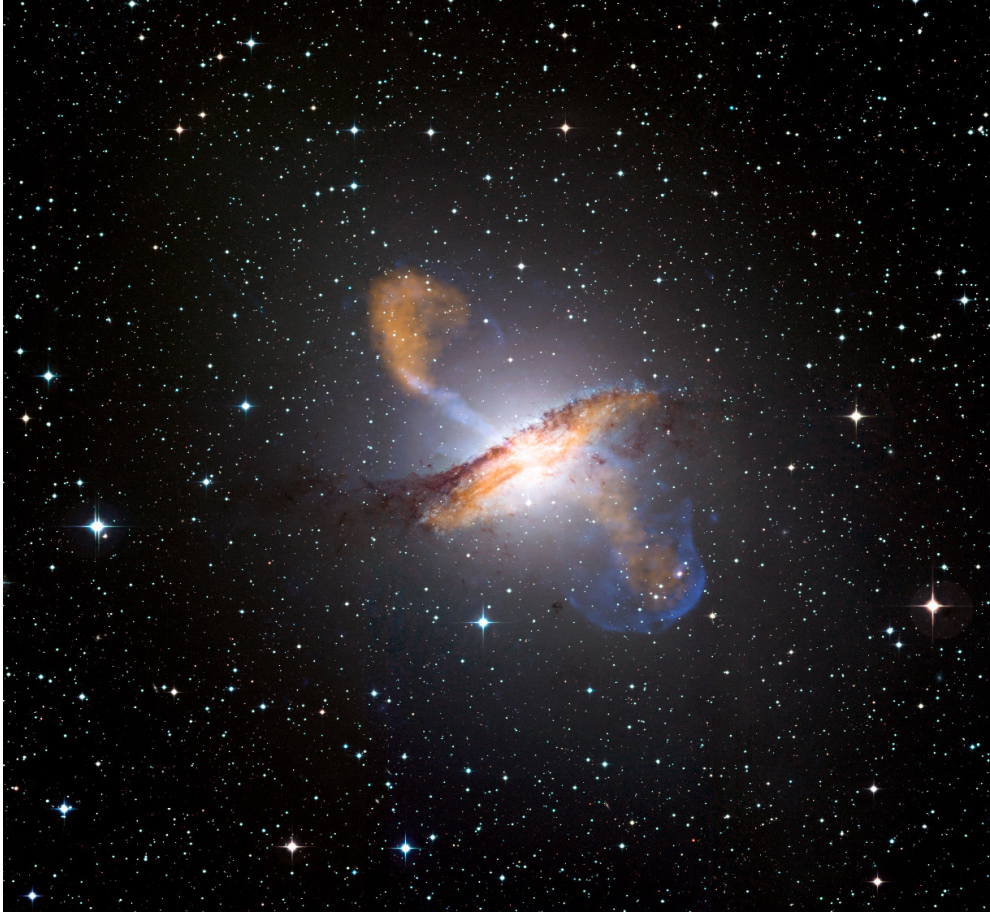


Figure 4.1: This image of Centaurus A shows a spectacular new view of a supermassive black hole's power. Jets and lobes powered by the central black hole in this nearby galaxy are shown by submillimeter data (colored orange) from the Atacama Pathfinder Experiment (APEX) telescope in Chile and X-ray data (colored blue) from the Chandra X-ray Observatory. Visible light data from the Wide Field Imager on the Max-Planck/ESO 2.2 m telescope, also located in Chile, shows the dust lane in the galaxy and background stars. The X-ray jet in the upper left extends for about 13,000 light years away from the black hole. The APEX data shows that material in the jet is travelling at about half the speed of light. Credit: ESO/WFI (Optical); MPIfR/ESO/APEX/A.Weiss et al. (Submillimetre); NASA/CXC/CfA/R.Kraft et al. (X-ray)

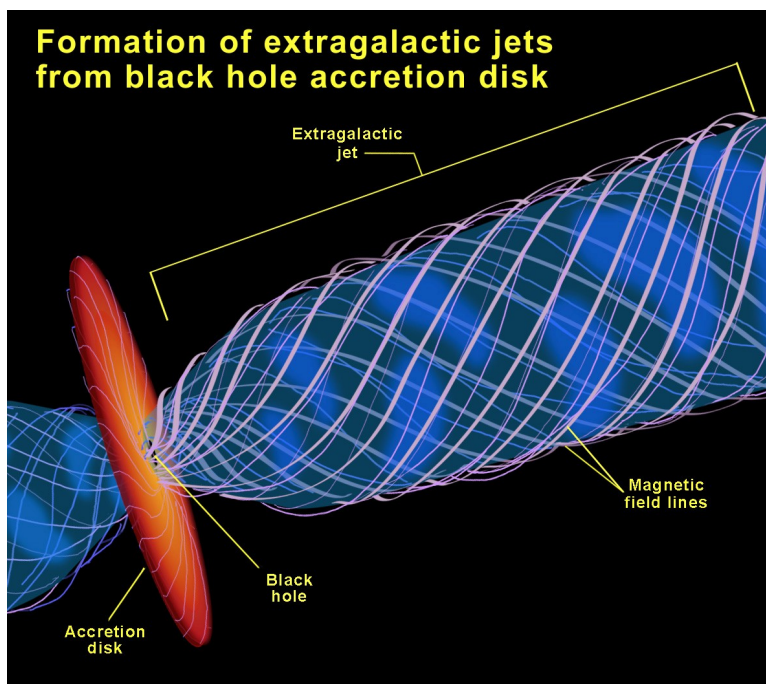


Figure 4.2: Qualitative representation of formation of extragalactic jet

The main subject of this chapter is a study on the stabilizing effect of the poloidal field by means of global 3D simulations of the MHD equations. The chapter is organized as follows. Review on the necessary and sufficient Tayler stability conditions and the main results of the linear analysis of non-axisymmetric instability of axisymmetric field (Bonanno and Urpin (2008)) are presented in Section 4.2. The next section 4.3 is devoted to the model description and the basic equations. Further, in Section 4.4, the numerical results of the non-linear three dimensional simulations of current-driven instability are presented. Finally, the conclusions are drawn in Section 4.5. The present research has been published in Ivanovski and Bonanno (2009)

4.2 The Tayler instability. Linear analysis

Tayler instability is MHD instability of toroidal fields in stably-stratified medium. Tayler (1973) used the energy method of Bernstein et al. (1958) to obtain necessary and sufficient stability conditions, showing that any purely toroidal magnetic field is unstable at least somewhere in the star. The stability conditions are local in merid-

4.2 The Tayler instability. Linear analysis

ional plane and global in azimuthal direction. The qualitative conditions of onset of instability are illustrated on Figure 4.3. If the magnetic field line rotates more than certain number of times around a cylinder column with characteristic height L , onset of instability can be triggered. The exact number of rotations required for instability is dependent on the considered equilibrium configuration. In the case of pressure-driven instability, the latter is arisen once the pressure force has pushed the plasma outwards from interior of the field line curvature. Basically it is a difficult task to determine the type of instability in actual plasma. Exceptions are some special cases as the cold plasma (no pressure force), where the instability is necessarily current-driven and the growth rates of current-driven modes are known to decrease with spatial order, i.e. they decay with increasing of the azimuthal wavenumber m . Another specific example is when the most unstable pressure-driven modes have a growth rate which is nearly independent on the wavenumber and hence, the instability is pressure-driven in a static, ideal MHD column. Besides these two limiting cases, an MHD instability always exhibit in a coupled mixture between the current- and pressure-driven types. The origin and the location of evolving of the unstable modes is of great importance for recognizing which type of instability is exhibited. If the most unstable modes are external. i.e. have substantial displacement on the plasma surface (here, the jet surface), then most likely in the fusion context, the unstable external modes disrupt the plasma and cause kink-type current-driven instability with the $m = 1$ ("kink") mode.

A magnetic field exerts a positive pressure perpendicular to its direction. In a toroidal field, this creates a situation like that in a compressed spinal column and therefore any purely toroidal field is subject to instability on or near the magnetic axis. The dominant mode is $m = 1$. In the following we review the stability conditions for onset of non-axisymmetric instability of axisymmetric magnetic fields (Bonanno and Urpin (2008) and the reference therein). A discussion on a purely toroidal magnetic configuration has been initiated since the paper by Tayler (1957), where stability properties of the toroidal field B_ϕ are determined by the parameter

$$\alpha = \frac{d \ln B_\phi}{d \ln r} \quad (4.1)$$

where r is the cylindrical radius. There are essentially two types of current-driven instability: (1) axisymmetric $m = 0$ and (2) non-axisymmetric $m = 1, 2, 3, \dots$ etc. The

4. 3D SIMULATIONS OF MHD INSTABILITIES IN JETS

sufficient condition for stability for a non-stratified medium to axisymmetric perturbations is $\alpha < 1$ while the sufficient (and also necessary) conditions for stability to non-axisymmetric perturbations is $\alpha < -1/2$. However, even a purely toroidal field can be stable in the region where it decreases rapidly with the radius r . A purely toroidal field cannot be stable through the whole star because the stability condition for axisymmetric modes ($\alpha < 1$) is incompatible with the condition that the electric current in the vertical direction has no singularity at $r \rightarrow 0$, which implies $\alpha < 1$.

The stability of the toroidal field changes substantially if even a relatively weak poloidal field is added to the magnetic configuration. For example, if the poloidal field is uniform and relatively weak, the instability necessary condition of axisymmetric modes for a non stratified medium reads $\alpha > -1$, which is weaker condition than the one for the purely toroidal field, which predicts that an unstable toroidal field configuration has $\alpha > -1/2$. Therefore, a weak poloidal field has a destabilizing effect. However, a strong enough poloidal field can suppress the instability of the toroidal field. Indeed, configurations containing comparable toroidal and poloidal fields are more stable than purely toroidal and poloidal ones (Prendergast (1956); Tayler (1980)). Bonanno and Urpin (2008) have investigated the stability properties of magnetic configurations containing the toroidal and poloidal magnetic fields with respect to non-axisymmetric perturbations via linear analysis. They found a wide range of the azimuthal wavenumber m , and that the growth rate is typically higher for higher m . Unstable modes with large m have a very short vertical length scale and hence, it is hard to resolve them in numerical calculations. Nevertheless, our results of the nonlinear MHD simulations confirm the main findings of the linear analysis. Depending on the profile $B_\phi(r)$ and the ratio B_z/B_ϕ , where B_z denotes the vertical magnetic field, the instability can occur in two regimes that have substantially different growth rates. Considering incompressible ideal MHD equations and with the assumption the gas to be in hydrostatic equilibrium the linear analysis reads that in case of non-axisymmetric perturbations the modes $m = 1, 2, 3, \dots$ can have even stronger growth rate than the axisymmetric ones. Moreover the pure toroidal field excites only $m = 1$ mode, while in the case of poloidal field all modes are excited. Then a relevant key question arise of the stabilizing effect of the poloidal field in the magnetic configurations, which involve toroidal and axial magnetic fields. We address the finding of this answer to a nonlinear approach using three- dimensional ideal MHD simulations.

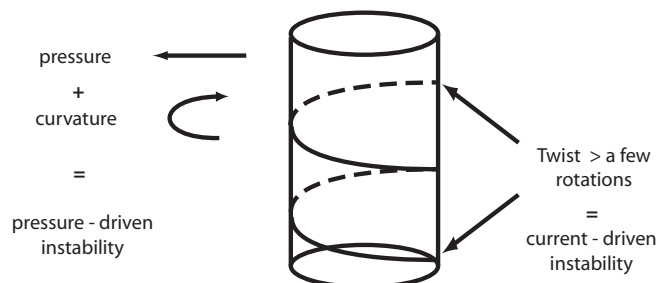


Figure 4.3: Qualitative description of the conditions of onset of MHD instabilities. Taken from Longaretti (2008)

4.3 Model and Basic Equations

For the purpose of this research we approximate the MHD jet by an infinitely long stationary isothermal cylindrical outflow of a perfectly conducting plasma. We suppose that the jet possesses constant velocity, as well as negligible thermal pressure and rotation. This excludes pressure-driven instabilities and then the equilibrium is described by a force-free field in the rest frame of the jet. The magnetic field is assumed to be axisymmetric with non-vanishing z - and φ - component. We consider as a basic state MHD equilibrium with azimuthal field balanced by the pressure gradient of non uniform radial density distribution with no vertical stratification. Initially small random density perturbations have been applied to the system. We use dimensionless units normalized with the height of the cylinder $h = 12$. We have a radial extent from $r_{in} = 0.1$ to $r_{out} = 1$ and time normalized with 10 sound crossing times $t_s = 10 * h/c_s$. The magnetic field is normalized to the Alfvén speed with the density normalization $d_0 = 4$. A qualitative image of the model is presented in Figure 4.4. We solve the time dependent ideal MHD equations

$$\frac{\partial \rho}{\partial t} + \nabla \cdot (\rho \mathbf{u}) = 0, \quad (4.2)$$

$$\frac{\partial \mathbf{u}}{\partial t} + (\mathbf{u} \cdot \nabla) \mathbf{u} = -\frac{\nabla p}{\rho} + \frac{1}{4\pi\rho} (\nabla \times \mathbf{B}) \times \mathbf{B}, \quad (4.3)$$

$$\frac{\partial \mathbf{B}}{\partial t} = \nabla \times (\mathbf{u} \times \mathbf{B}), \quad (4.4)$$

4. 3D SIMULATIONS OF MHD INSTABILITIES IN JETS

$$\nabla \cdot \mathbf{B} = 0, \quad p = c_s^2 \rho, \quad (4.5)$$

with periodic boundary conditions in z and reflection in r and φ . Our boundary conditions give magnetic flux conservation for the field. The z and φ averaged radial magnetic field has to be zero because of our boundary conditions. We explore the ZEUS-MP/2 code (discussed in Section 2.8) in cylindrical coordinates (r, φ, z) . We varied the grid resolution for closer representation of cylindrical jet structure, namely, from $80 \times 80 \times 80$ (results are summarized in Table 4.1) up to $240 \times 80 \times 80$ (Table 4.2).

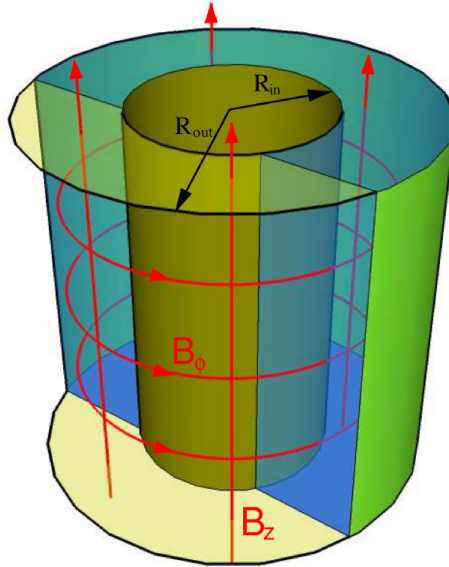


Figure 4.4: Schematical view of the model. Courtesy: J. Szklarski

4.4 3D Simulations of current-driven instabilities

We made different simulations with respect to the magnetic configuration which was considered, namely, purely toroidal field and configurations with toroidal and different magnitude of poloidal field. In all the tests we have chosen constant toroidal magnetic field with $v_a = 10$. We find a growth time of 0.15 times already shown by Elstner et al. (2008) for resolution of 160^3 grid points, which is consistent with the inverse of the Alfvén frequency $\pi r/v$ roughly at the inner boundary $r=1$. The growth rate is determined by the maximum growth rate of the radial magnetic energy during the

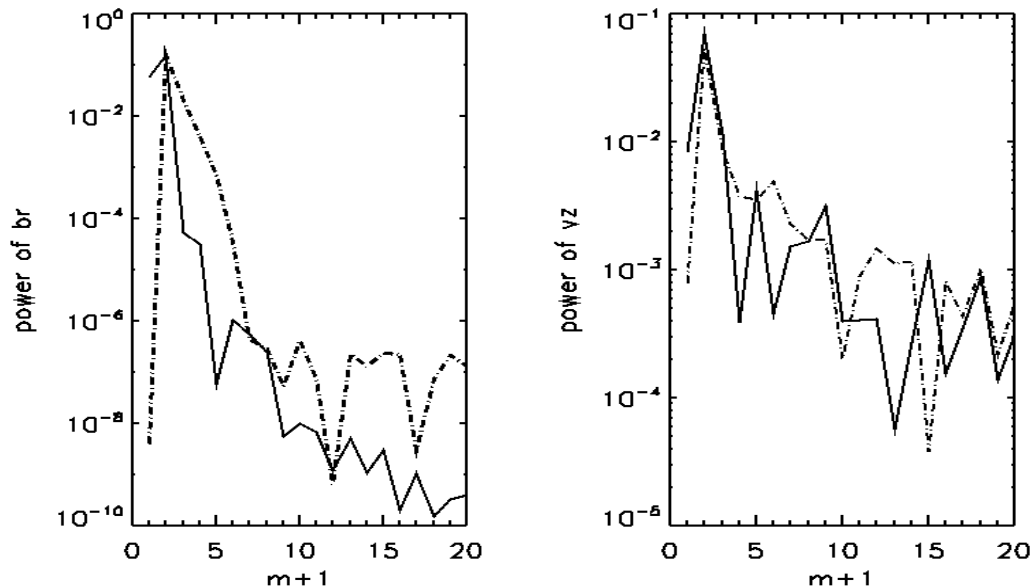


Figure 4.5: The spectrum power of the radial magnetic field B_r (*left*) and the vertical velocity v_z (*right*). The dotted line denotes the case without axial field, the solid line denotes the case with the strength of the axial field $\varepsilon = 1$. The sound speed $c_s = 10$, the resolution is $80 \times 80 \times 80$, the height of the cylinder is 12.

exponential growth phase. We define the Alfvén time as $t_a = r_{out}/\max(v_a)$. The configuration is unstable and the initial growth is dominated by an azimuthal wave number $m = 1$ as it is shown in Figure 4.5. Axisymmetric and higher m -modes are excited and grow in the nonlinear coupling phase. After $0.4t_a$ the magnetic field strength of the radial and vertical component is at the maximum and then decays. A new final equilibrium state is reached after $2t_a$. The density is redistributed to an uniform one and the toroidal magnetic field - to a current free state (Fig.4.6). It means that the radial profile of the magnetic field is proportional to $1/r$ that is not the marginal stable solution. The first column of Table 4.1 denotes the strength of the axial field, measured via $\varepsilon = B_z/B_\varphi$, the rest columns, respectively, the growth time of the azimuthal and radial velocity and magnetic field. There is no growth of the vertical magnetic field B_z . For all simulations we have the normalized growth time $T_g = t_{growth}v_a/r_{out}$. With increasing the strength of the axial field, the growth time of all presented components in Table 4.1 increase as well. Consequently, the growth

4. 3D SIMULATIONS OF MHD INSTABILITIES IN JETS

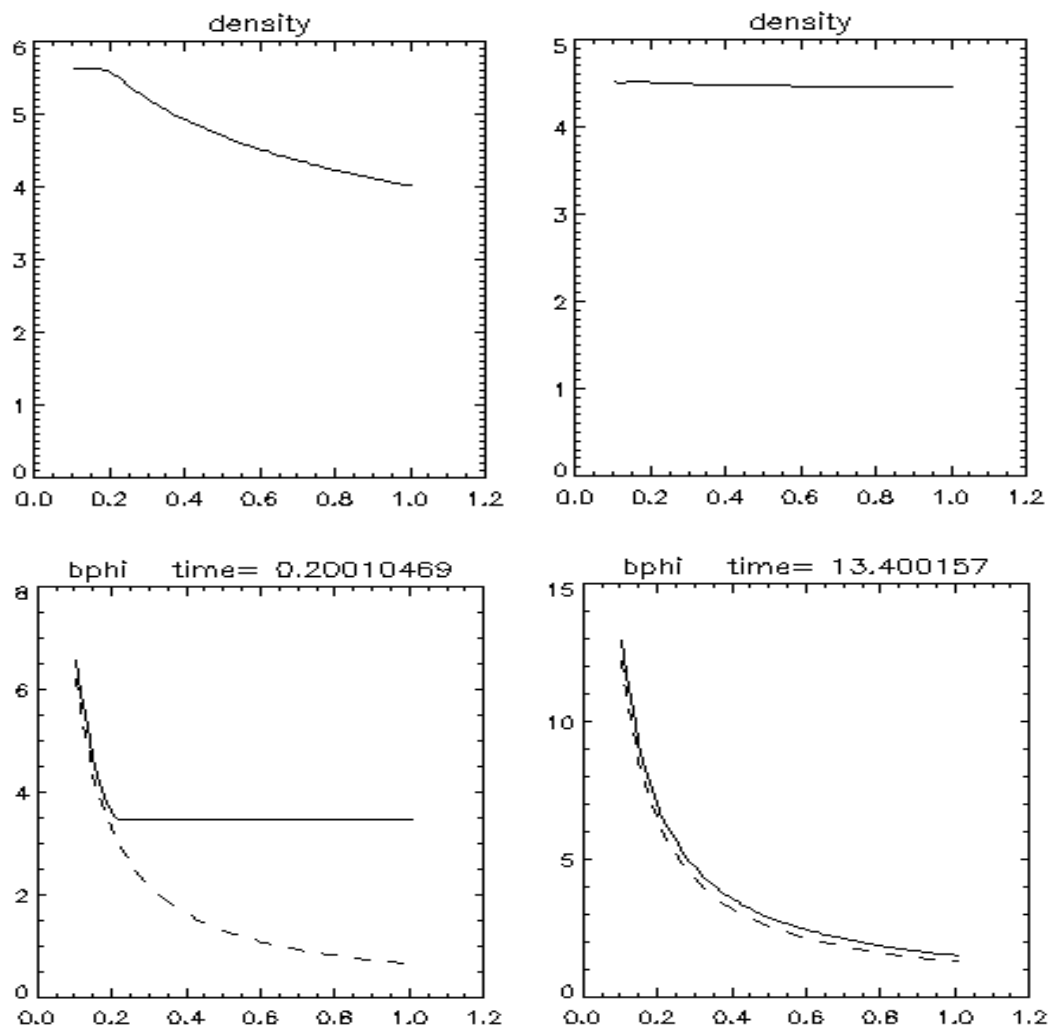


Figure 4.6: Azimuthal and vertical averaged density and toroidal field in radial profiles for initial (*left*) and final (*right*) state. The dashed line in the panel of B_φ ('bphi' on the plot) shows the profile $1/r$.

4.4 3D Simulations of current-driven instabilities

| ε | u_φ | u_r | u_z | B_φ | B_r |
|---------------|-------------|-------|-------|-------------|-------|
| 0 | 0.29 | 0.32 | 0.33 | 0.34 | 0.34 |
| 0.1 | 0.32 | 0.34 | 0.35 | 0.75 | 0.34 |
| 0.5 | 0.35 | 0.36 | 0.37 | 1.50 | 0.37 |
| 1 | 0.38 | 0.38 | 0.39 | 2.20 | 0.38 |
| 2 | 0.41 | 0.41 | 0.40 | 2.90 | 0.41 |

Table 4.1: The growth time values for the azimuthal and radial velocity and magnetic field, varying the vertical field strength (see the text for the details).

| ε | c_s | u_φ | u_r | u_z | B_r |
|---------------|-------|-------------|-------|-------|-------|
| -1 | 10 | 0.27 | 0.28 | 0.28 | 0.27 |
| -1 | 50 | 0.34 | 0.36 | 0.37 | 0.38 |
| -5 | 10 | 0.47 | 0.50 | 0.39 | 0.40 |
| -5 | 50 | 0.53 | 0.46 | 0.48 | 0.48 |
| -10 | 10 | 1.53 | 1.30 | 1.14 | 1.10 |
| -10 | 50 | 1.37 | 0.95 | 1.05 | 0.88 |

Table 4.2: The growth time values for the azimuthal and radial velocity and magnetic field, varying the vertical field strength and the sound speed (see the text for the details).

rate, as an inversed value of the growth time is decreasing along the stronger poloidal magnetic field. Figure 4.7 shows the quenching behaviour of growth rate of the radial components in dependance on the strength of the axial magnetic field, which gives clear message of stabilizing effect by strong axial magnetic field. Figure 4.8 and Figure 4.9 show radial and azimuthal snapshots of the toroidal magnetic field and density in the case of pure toroidal field. The resolution is $480 \times 80 \times 80$ grid points. The height of the domain is 12, $\varphi = 0; 2\pi$ and the sound speed c_s is 10. During the nonlinear evolution, the system develops large scale structures in radial and azimuthal direction. The horizontal displacements series evolved from the inner boundary and are distributed almost regularly in whole domain. The typical Tayler instabilities structures decay into uniform density distribution. In azimuthal direction is clearly developed

4. 3D SIMULATIONS OF MHD INSTABILITIES IN JETS

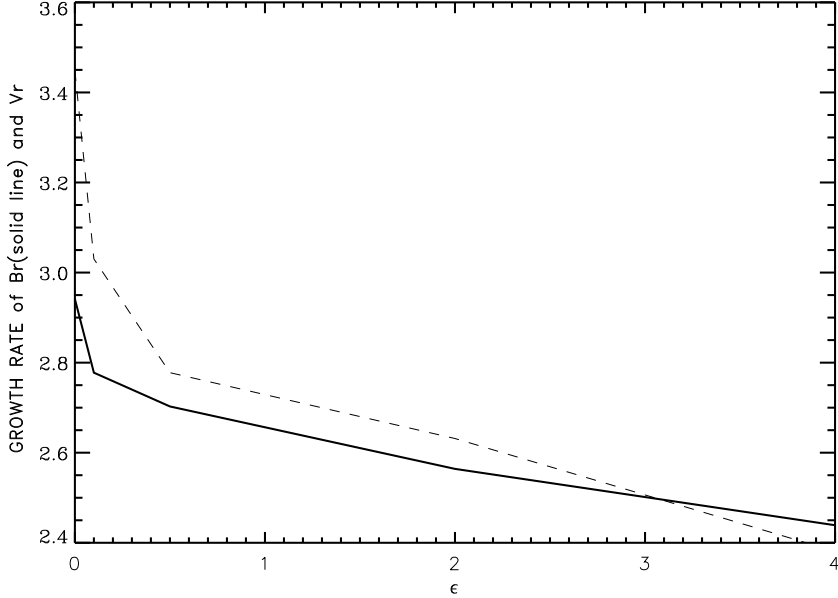


Figure 4.7: The growth rate of the radial components of velocity (*dashed line*) and magnetic field (*solid line*) versus the strength of the axial field. The stronger axial magnetic field, the stronger suppression of the instability.

$m = 1$ mode which is still excited in the saturation phase. When a weak poloidal field is included in the magnetic configuration, the system remains unstable longer and the number of horizontal displacements become smaller but more intensive. The instability diminishes slower than the pure toroidal case. Very large scale "kink" mode instability is developed as can be seen in Figure 4.10 and Figure 4.11. The height of the domain is 12, the sound speed $c_s = 10$, the strength of the axial magnetic field is $\epsilon = -0.1$, $\varphi = 0; 2\pi$. Magnetic configurations containing the toroidal and axial magnetic fields with respect to non-axisymmetric perturbations may develop a wide range of excited azimuthal modes and the growth rate is typically higher for higher m Bonanno and Urpin (2008). If we increase the strength of the axial field, the value of the maximum growth rate decreases, as it is shown by Bonanno and Urpin (2008). In the the analysis performed by Bonanno and Urpin we know that the relation of the azimuthal wave number m and the vertical wave number k satisfy

$$k\mathbf{B}_z + \frac{m\mathbf{B}_\varphi}{r} = 0 \quad (4.6)$$

On the other hand it is difficult to excite higher m in our simulations, most probably

4.4 3D Simulations of current-driven instabilities

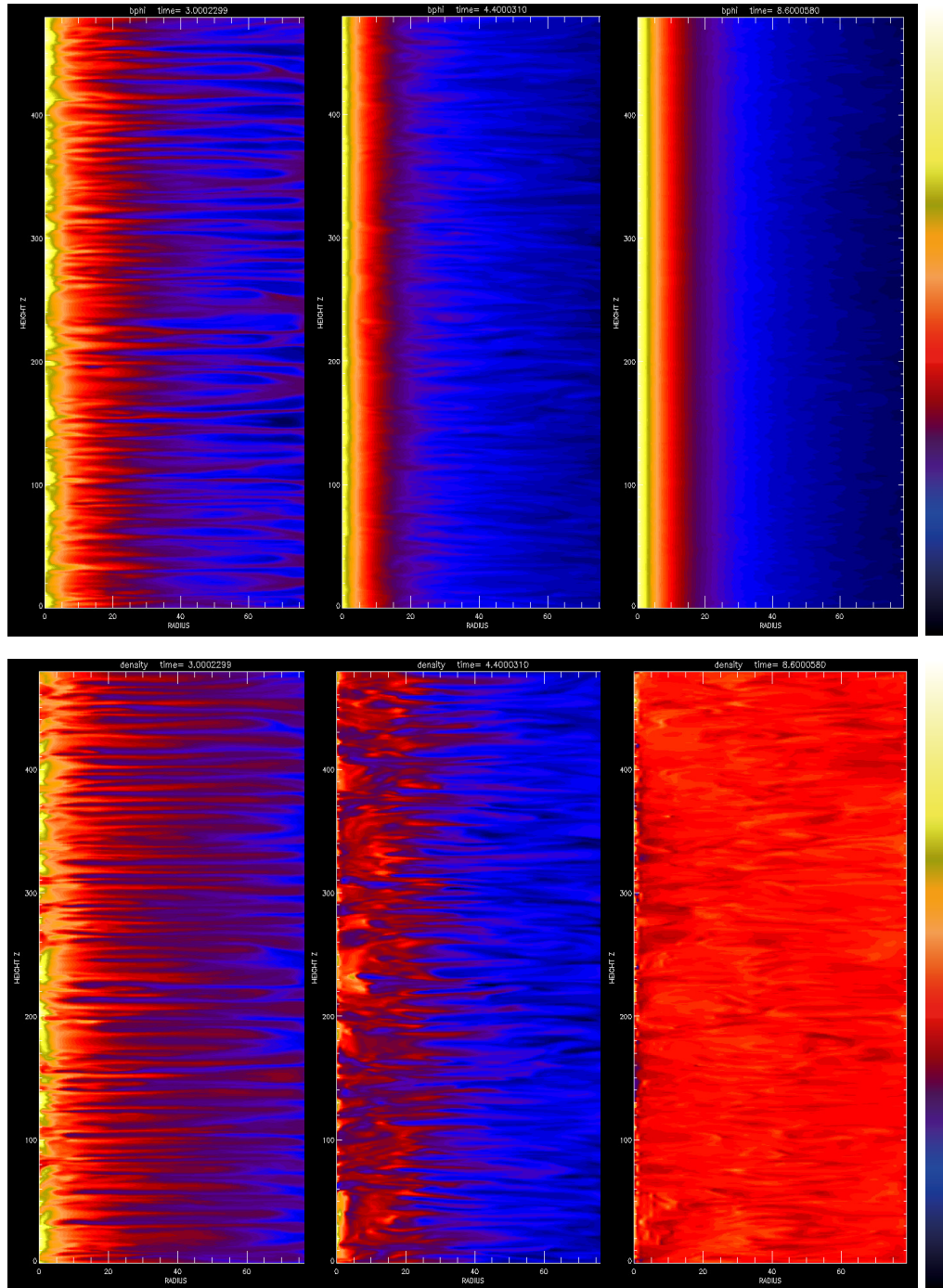


Figure 4.8: In the horizontal direction: two series of three snapshots of the pure toroidal magnetic field configuration profiles ($\varepsilon = 0$). The first sequence (*top*) shows vertical cut along the radius for the radial magnetic field, while the second sequence (*bottom*) shows vertical cut along the radius for the density. The time sequences (in the horizontal direction) for both sets of results are taken at $t = 3; 4.4; 8.6$. The resolution is $480 \times 80 \times 80$.

4. 3D SIMULATIONS OF MHD INSTABILITIES IN JETS

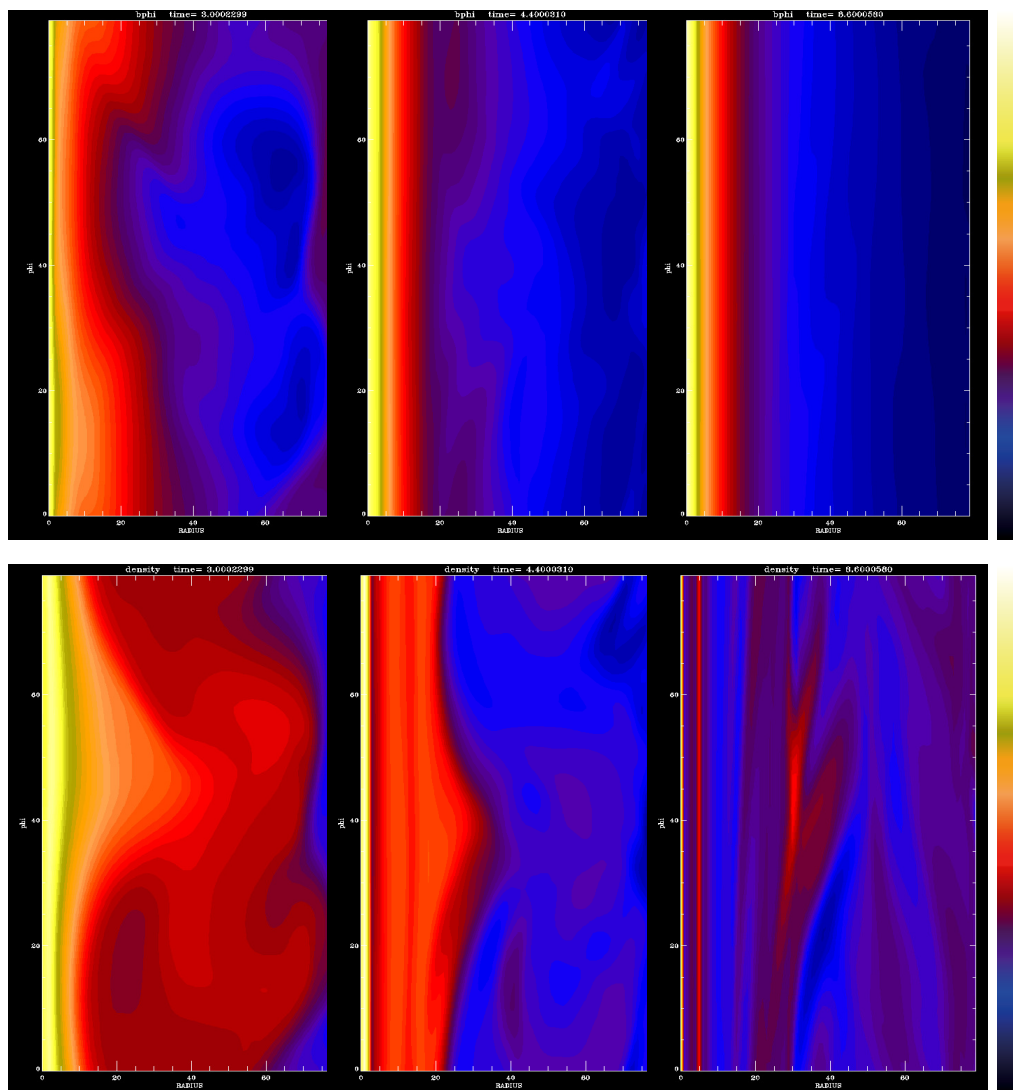


Figure 4.9: In the horizontal direction: two series of three snapshots of the pure toroidal magnetic field configuration profiles ($\varepsilon = 0$). The first sequence (*top*) shows a cut in azimuthal direction along the radius for the radial magnetic field, while the second sequence (*bottom*) shows a cut in azimuthal direction along the radius for the density. The time sequences (in the horizontal direction) for both sets of results are taken at $t = 3; 4.4; 8.6$. The resolution is $480 \times 80 \times 80$.

4.4 3D Simulations of current-driven instabilities

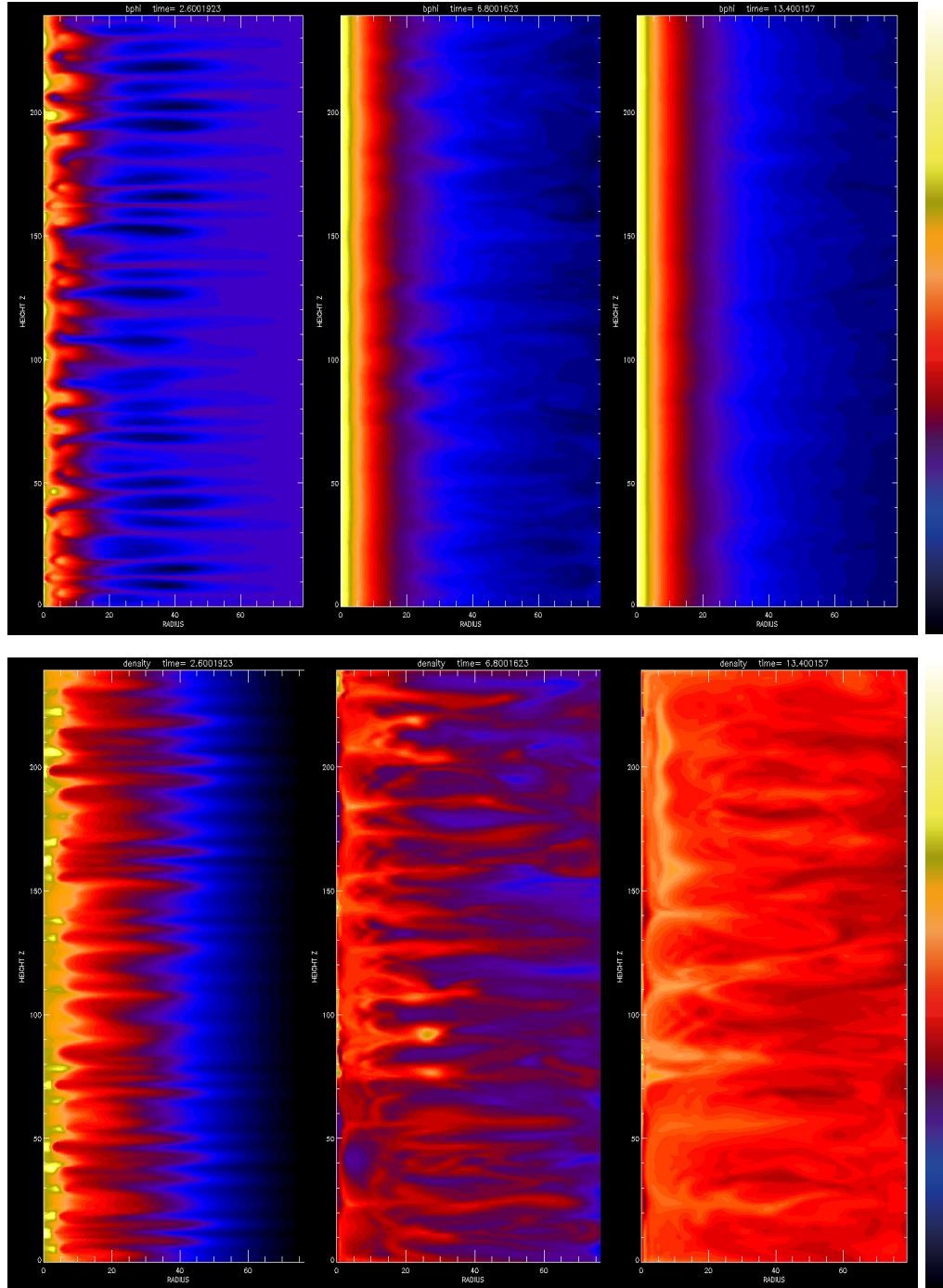


Figure 4.10: The same as in Figure 4.8 but for axial and toroidal magnetic field configuration with strength of the axial field $\varepsilon = -0.1$. The resolution is $240 \times 80 \times 80$ and the time sequence is for $t = 2, 6, 6, 8, 13.4$.

4. 3D SIMULATIONS OF MHD INSTABILITIES IN JETS

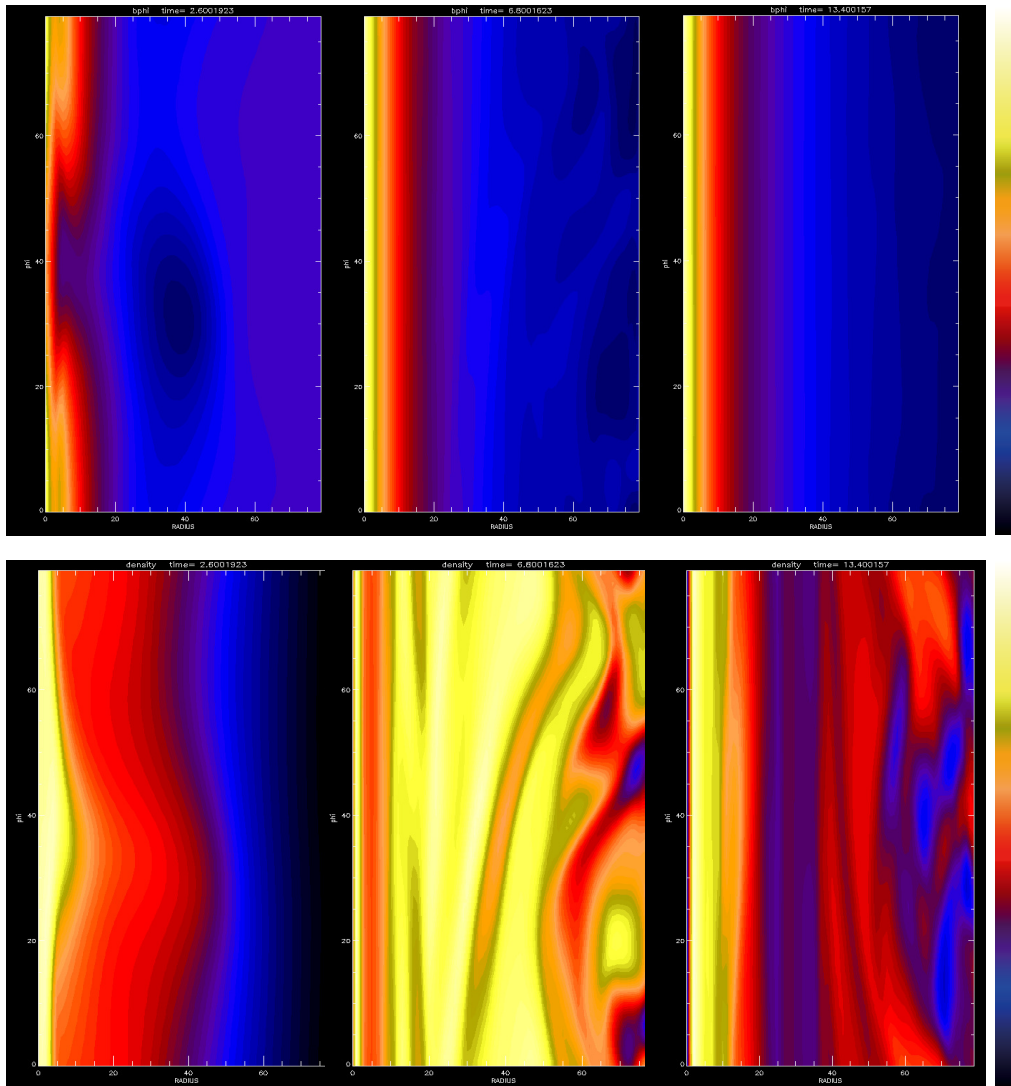


Figure 4.11: The same as in Figure 4.9 but for axial and toroidal magnetic field configuration with strength of the axial field $\varepsilon = -0.1$. The resolution is $240 \times 80 \times 80$ and the time sequence is for $t = 2, 6; 6, 8; 13.4$.

4.4 3D Simulations of current-driven instabilities

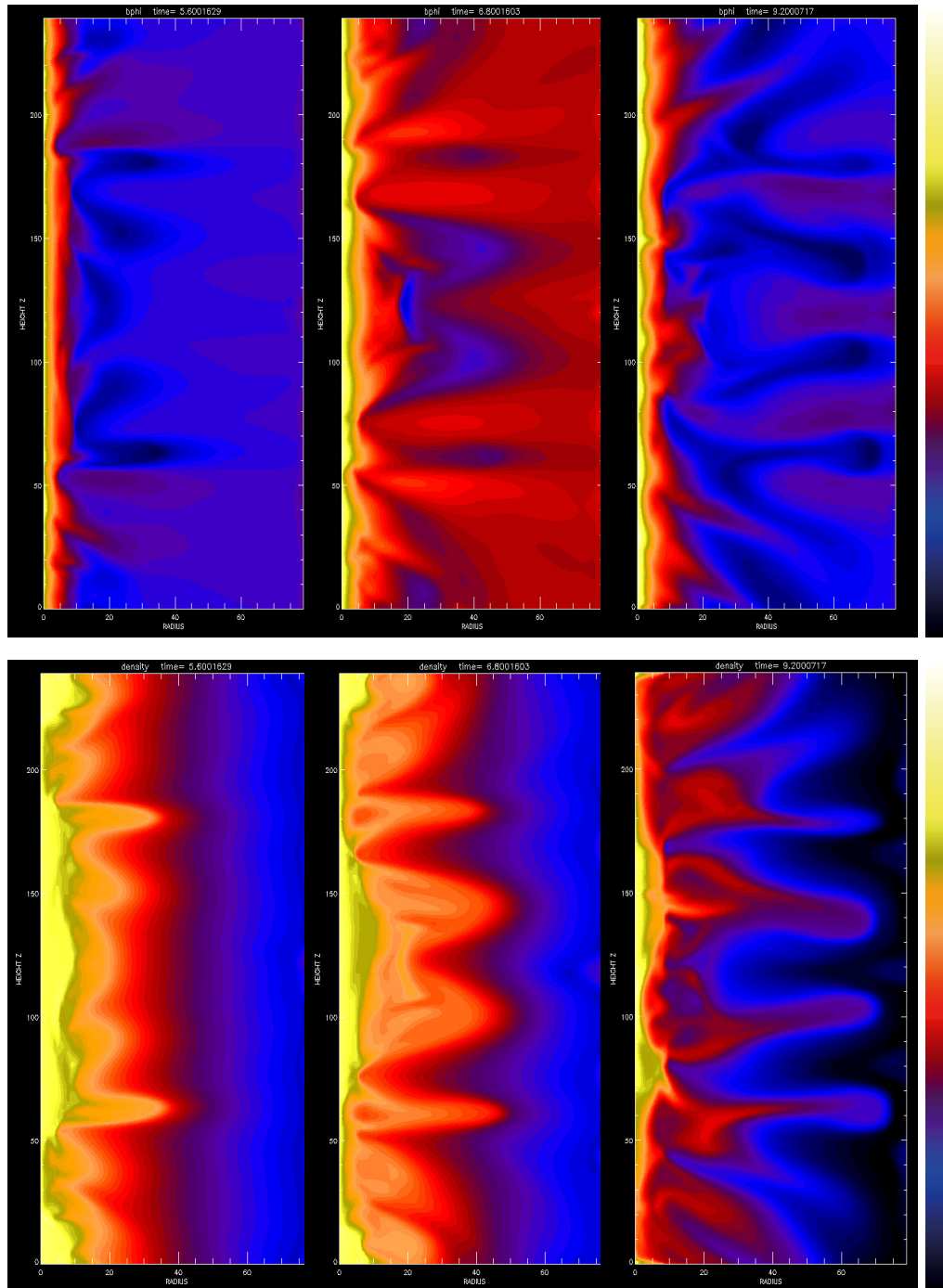


Figure 4.12: The same as in Figure 4.10 but for stronger axial magnetic field ($\varepsilon = -1$). The time sequence is for $t = 5; 6.8, 9.2$. The resolution is $240 \times 80 \times 80$.

4. 3D SIMULATIONS OF MHD INSTABILITIES IN JETS

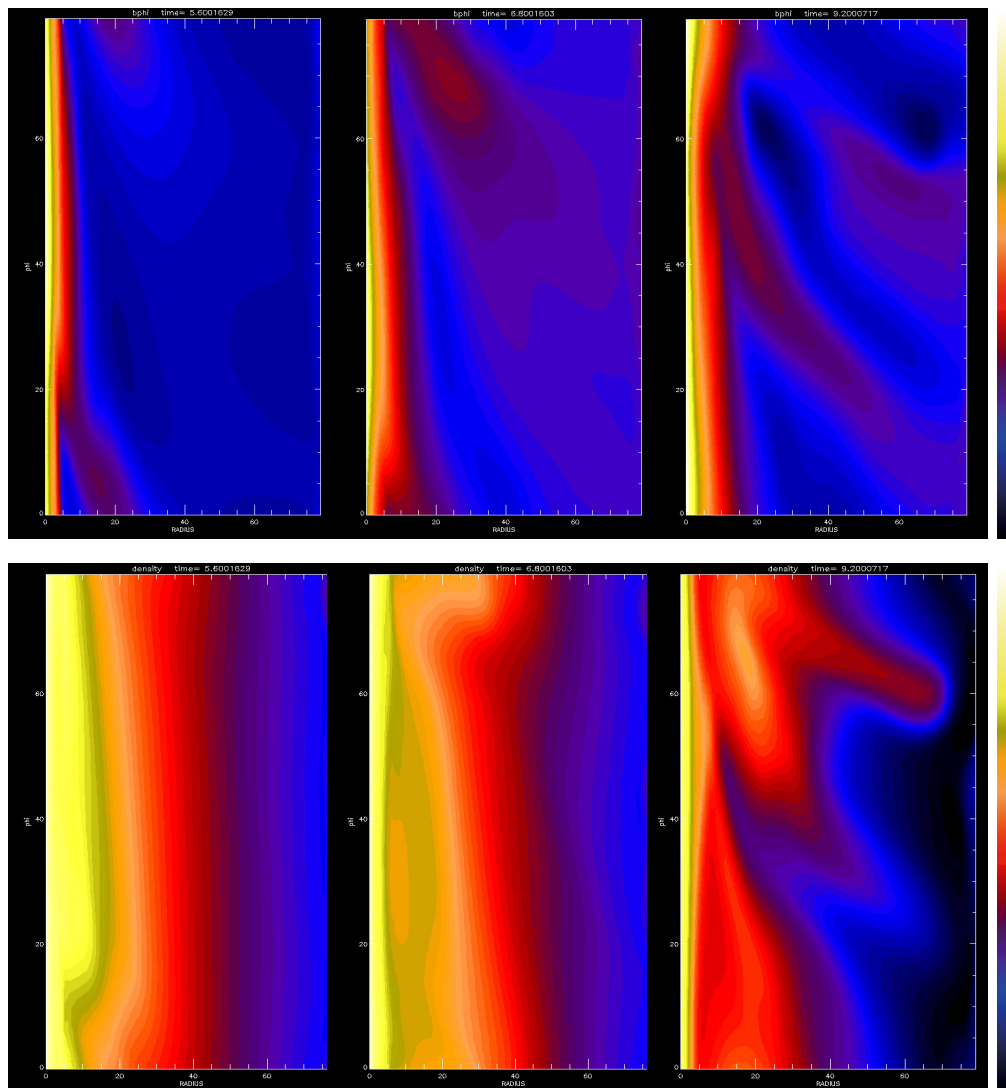


Figure 4.13: The same as in Figure 4.11 but for stronger axial magnetic field ($\varepsilon = -1$). The time sequence is for $t = 5; 6.8, 9.2$. The resolution is $240 \times 80 \times 80$.

because of the lack of the proper resolution. The stronger the axial magnetic field, the smaller the growth rate. Large horizontal displacements can be seen in Figure 4.12 and Figure 4.13, where the height of the domain is 12, the sound speed $c_s = 10$ and the strength of the axial magnetic field is $\varepsilon = -1$.

4.5 Conclusions

We have performed global 3D simulations of the Tayler instability in the presence of vertical fields. We have shown that, unless the strength of the imposed field is comparable to the azimuthal field the Tayler instability is not suppressed. The initial configuration is in equilibrium, which is achieved by a pressure gradient or an external potential force. We have used cylindrical geometry with perfect conductor boundary conditions in the radial and vertical direction. The MHD equilibrium with constant toroidal field, was balanced with pressure and there was no rotation and no stratification in the MHD model. We have assumed isothermal equation of state.

The non linear evolution of the system leads to a stable equilibrium with a current free toroidal field. The final state is a force free field, but this can be a consequence of the flux conservations imposed as boundary conditions. We hope to extend our investigations to the case of rotating magnetically supported jets, by including also the effect of a thermal equation of state.

4. 3D SIMULATIONS OF MHD INSTABILITIES IN JETS

Chapter 5

Plasma Astrophysics and Laser Experiments: Hydrodynamical Simulation of Colliding Plasmas

5.1 Introduction

The interaction of pulsed laser ablation plumes with a background gas has been investigated for years due to its various application and importance in laser deposition, cluster production, nanoparticle formation and growth, chemical analysis, etc. A key application has also been discussed in connection with modeling of various processes in space physics, plasma material science, and hydrodynamics. Expansion of plasma has been investigated via various theoretical models (Arnold et al., 1999; Chen et al., 1995; Mora, 2003; Strehlow, 2001) and several diagnostic techniques have been proposed including mass and optical emission spectroscopy, photothermal beam deflection, laser interferometry. Fast photography using intensified charge coupled device (ICCD), shadowgraphy, and Schlieren photography have been utilized to study the plume dynamics of the expanding plasma in vacuum and ambient atmosphere (Sharma and Thareja, 2005; Ventzek et al., 1992; Wong et al., 1998). The plume activity in ambient gas is a far more complex gas dynamic interaction in comparison with the expansion into the vacuum and implies diffusion, formation of shock waves, clustering, plume splitting and bifurcation, onset of instability and turbulence. The problem of the expansion of a single plume in ambient gas is usually associated with distinct propagation regimes,

5. HYDRODYNAMICAL SIMULATION OF COLLIDING PLASMAS

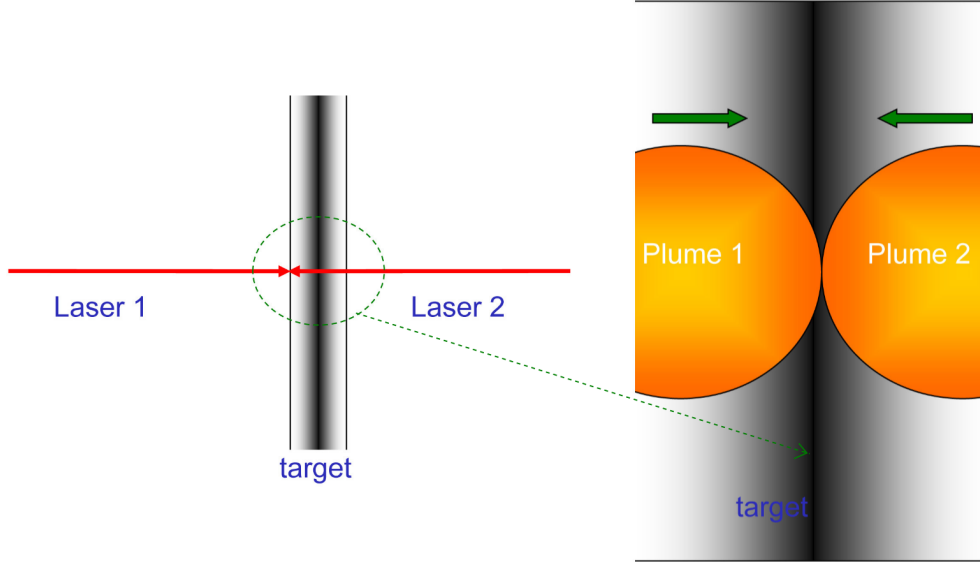


Figure 5.1: Qualitative representation of the model

strongly dependent on the pressure of the gas. Experimental analysis of the laser ablation of an aluminum target is reported by (Harilal et al., 2003). The authors discussed the expansion of a single plume in a gas at different pressure levels: the plasma expands freely in a vacuum or low background pressure (about 10^{-6} Torr), but at moderate pressures of about 1.3 Torr shock front is formed, accompanied by an explosive release of energy and results in slowing of the expansion, i.e., dragging the plume, which eventually come to rest due to the resistance from the collisions with the background gas. In addition, in the case of moderate background pressure, the plume splitting occurs and while the expansion of the fast component is characterized by interpenetration within the gas, the slow one could exhibit instabilities such as RT instability near the contact boundary with the gas.

(Sharma and Thareja, 2007) also addressed the perturbations at the plasma-gas interface of the expanding plasma in gas to the RT instability. Considering a single plume, formed by pulsed laser ablation of aluminum in ambient pressure of nitrogen, the authors confirm instability at pressure ≥ 1 Torr and comment on a stability condition (Harilal et al., 2003) of the onset of Rayleigh-Taylor instability. (Baranov et al., 1993) also claimed that due to the RT instability, the expanding plasma front tends to be unstable, which made the ambient gas be perturbed.

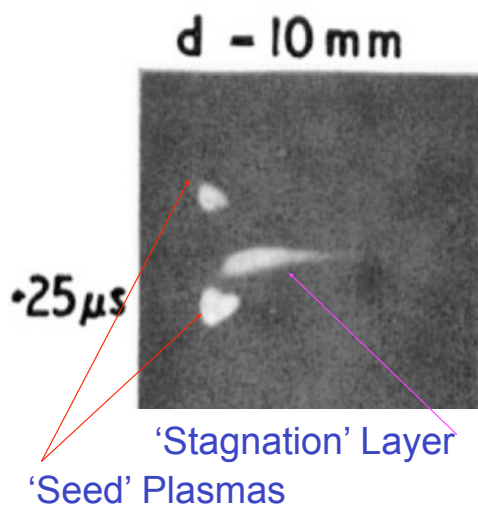


Figure 5.2: Seed plasmas and the stagnation layer

The idea of colliding plasmas is not new. In 1974, (Rumsby et al., 1974) discussed interactions between two colliding laser produced plumes. They argued that two extreme scenarios are possible when two plasmas collide: interpenetration due to interactions mostly invoked by binary collisions and stagnation, characterized by plumes deceleration at collision plane, rapid accumulation of material, kinetic energy conversion into excitation energy (glow), rapid growth of dense (stagnated) layer, etc. Their work implies that the slow moving and dense plumes are likely to stagnate and by varying the geometry and laser-target interaction physics one can engineer the stagnation layer. Image of stagnation layer and 'seed' plumes are shown in Figure 5.2 In this chapter we suggest that the RT instability can be generated through the collisions of two plumes in the stagnation limit described in (Rumsby et al., 1974). In fact, if two plumes are colliding in this limit, the conversion of the kinetic energy into the thermal energy ionizes further the gas and raises its local temperature. As a result we notice that the RT onset instability is enhanced in such a configuration, which also shows a jet-like structure during the collision. We report numerical investigation of interaction between two plumes, expanding in a gas, via simulations of gas-dynamic equations.

5. HYDRODYNAMICAL SIMULATION OF COLLIDING PLASMAS

The present research has been published in two papers, namely, (Ivanovski et al., 2010) and (Mascali et al., 2010).

5.2 The Rayleigh-Taylor instability

An instability as we consider it here is a phenomenon in which a smooth stationary state becomes unstable for small amplitude perturbations. With time, these seed perturbations start growing. At first the growth rate can be determined from the linearized equations, because the perturbations are small. At a later stage, the instability is saturated or stopped by the nonlinear processes. These processes make the instability be gradually removed, unless some external process can maintain it. Generally, such processes can not be subject of quantitative analyze using linearized equations. The original Rayleigh- Taylor instability appear when a heavier fluid is placed above a lighter one in a gravitational field. The interface between the fluids will be unstable for small perturbations. The Rayleigh- Taylor type instabilities are very common in physical situations where we have lighter fluid below a heavier (colder) one. Further, if a warming is set on, it must be fats enough so that the expansion overwhelms the background exponential decrease of the density with the hight. This situation, although intuitively understood physically, is rather complicated from analytical viewpoint because the background density and temperature profiles must be considered. In a plasma the Rayleigh- Taylor instability can arise even in a larger variety of ways than in neutral hydrodynamics. The role of the gravitational field can be taken by a background electric field. An important aspect of instability worth mentioning. The onset of instability requires some external energy input. In the case of interaction between two plasma plumes, the collisions speed up the conversion of the kinetic energy into thermal one which ionizes further the gas and raises the local temperature. The high temperature itself warm up the fluid and hence, favors the set of physical situations of interaction between a light fluid with a heavier in the ambient medium. In the following sections we discuss the onset of such instability as a result of collision processes between the interacting high-dense plasmas.

5.3 Model of Colliding Plumes

The onset of colliding plasmas phenomena in a lab experiment usually is initialized with laser beam pulse reaction on the target surface, which ends up with a vapor-plasma plumes time evolution interaction. The expansion of the plasma plume can be described by the hydrodynamic equations

$$\frac{D\rho}{Dt} + \rho \nabla \cdot \mathbf{u} = 0, \quad (5.1)$$

$$\frac{D\mathbf{u}}{Dt} = -\frac{\nabla p}{\rho}, \quad (5.2)$$

$$\frac{D}{Dt} \left(\frac{e}{\rho} \right) = -\frac{p}{\rho} \nabla \cdot \mathbf{u}. \quad (5.3)$$

Here, the dependent variables are the mass density ρ , the velocity \mathbf{u} , and the internal energy density e . The $D/Dt \equiv \partial/\partial t + \mathbf{u} \cdot \nabla$ denotes the Lagrangean or comoving derivative. The fluid equations are closed with the equation of state of ideal gases with $\gamma = 5/3$. The applied boundary conditions are axis of symmetry boundary conditions. These conditions are identical to reflecting ones, except that the velocity is set equal to the negative of the value of velocity in the corresponding active zones, forcing it to vanish on the boundary. We used ZEUS-MP/2 code (Stone and Norman, 1992)(see also Chapter 2, Section 2.8) in our simulations. The domain is a Cartesian cube, which side length and grid resolution are varied in the different simulations.

Two identical elliptical regions representing the two plumes, standing each of the other at a varied distance D of initial radius r expand into a gas with much lower density, creating plasma plumes interaction. Over-density and overpressure factors, d_ratio and p_ratio , representing the ratio of the initial plume density and pressure values with the initial density and pressure values of ambient gas, respectively, are used like control parameters in the simulations. Two selected simulations of the onset of instability, with different resolutions are given in Table 5.1.

5. HYDRODYNAMICAL SIMULATION OF COLLIDING PLASMAS

| Simulations | d_ratio | p_ratio | r | D | $resolution$ | $domain\ size$ |
|-------------|-------------------|----------------------|------|-----|--------------|----------------|
| A | 1.0×10^2 | 1.0×10^{18} | 0.04 | 0.2 | 64^3 | $4cm$ |
| B | 1.0×10^2 | 1.0×10^{18} | 0.2 | 0.3 | 128^3 | $4cm$ |

Table 5.1: Numerical simulations of colliding plumes

5.4 Results

The Rayleigh-Taylor instability is associated with the interface interaction between the fluids with different density and it could be recognized usually by the perturbation structures at the contact boundary. Since this instability could appear in the plume-gas interaction of a single plume, suggested by authors mentioned above, an interesting question is whether it exhibits when two plumes colliding and if yes, how the two-plumes configuration responds to the strength of the background gas pressure. After the collision the instability growth is more likely to happen in the region of maximum acceleration and can be derived from the derivative of momentum conservation equation

$$\frac{d}{dt} \left[\left(M_0 + \frac{4}{3} \pi R^3 \rho_g \right) \mathbf{u} \right] = 0, \quad (5.4)$$

where M_0 is the total mass after the collision, R the distance of the shock front from the target surface, ρ_g the gas density, and u is the plasma front velocity, respectively. The solution gives

$$\rho_g = \frac{6M_0}{28\pi R^3} \quad (5.5)$$

The instability occurrence in a narrow interface formed by plumes and the gas depend on the acceleration direction, i.e., whether the acceleration is from low density to high density region or vice versa. The growth rate of RT instability is governed by

$$\alpha^2 = -Ka \frac{\rho_p - \rho_g}{\rho_p + \rho_g}, \quad (5.6)$$

with ρ_p and ρ_g being the plasma and background densities, K as the wave number, and a as the acceleration of the plasma front, respectively (Abhilasha et al., 1993). The plasma boundary is stable when $\alpha^2 > 0$ ($\rho_p < \rho_g$) and unstable vice versa. Our simulations in which we obtained RT instability are in agreement with this stability condition.

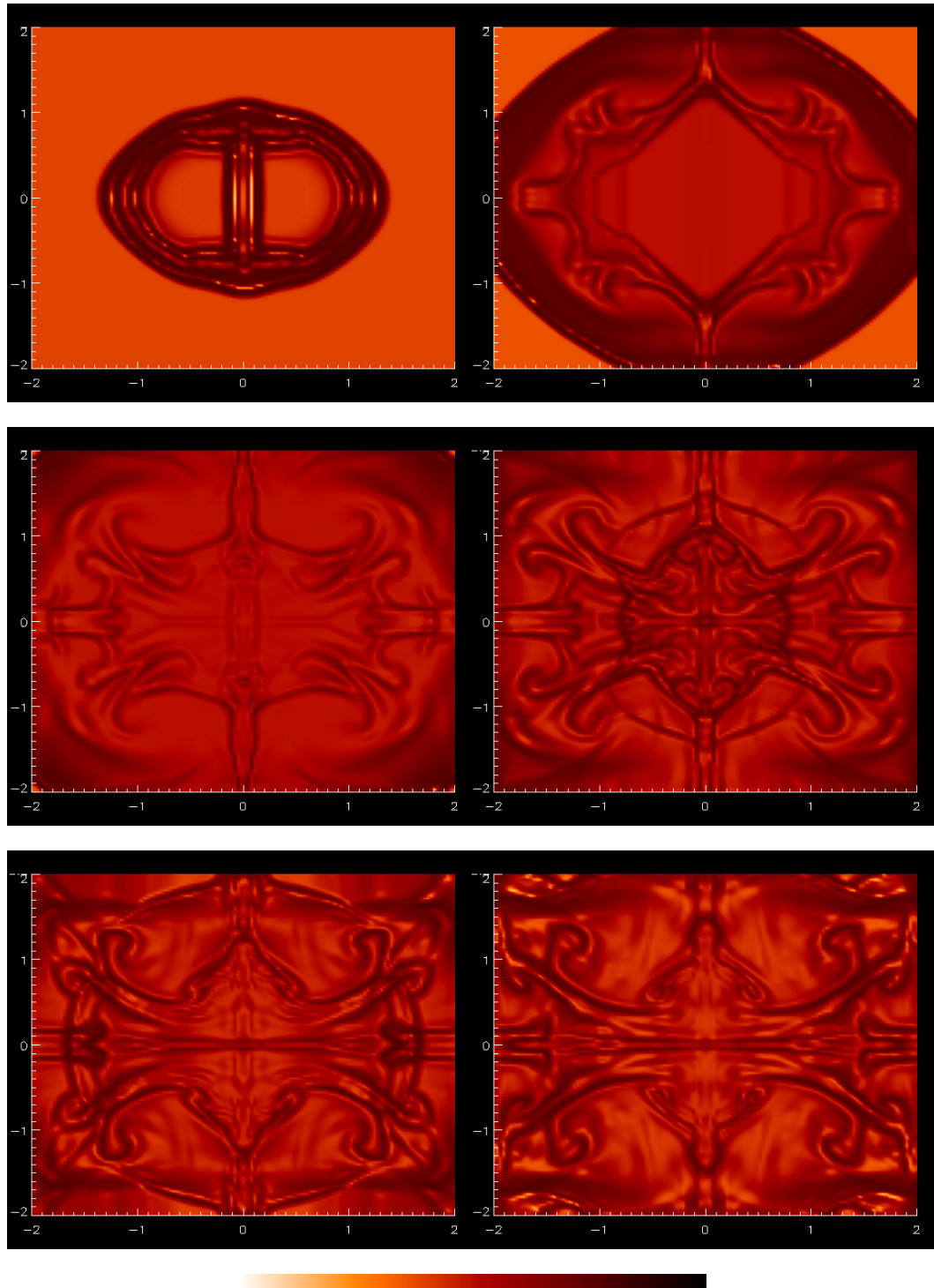


Figure 5.3: Rayleigh-Taylor instability patterns of colliding plumes representing density. The time evolution is 6; 20; 40; 60; 80; 100 ns. The setup is given in Table 5.1 (Sim. B).

5. HYDRODYNAMICAL SIMULATION OF COLLIDING PLASMAS

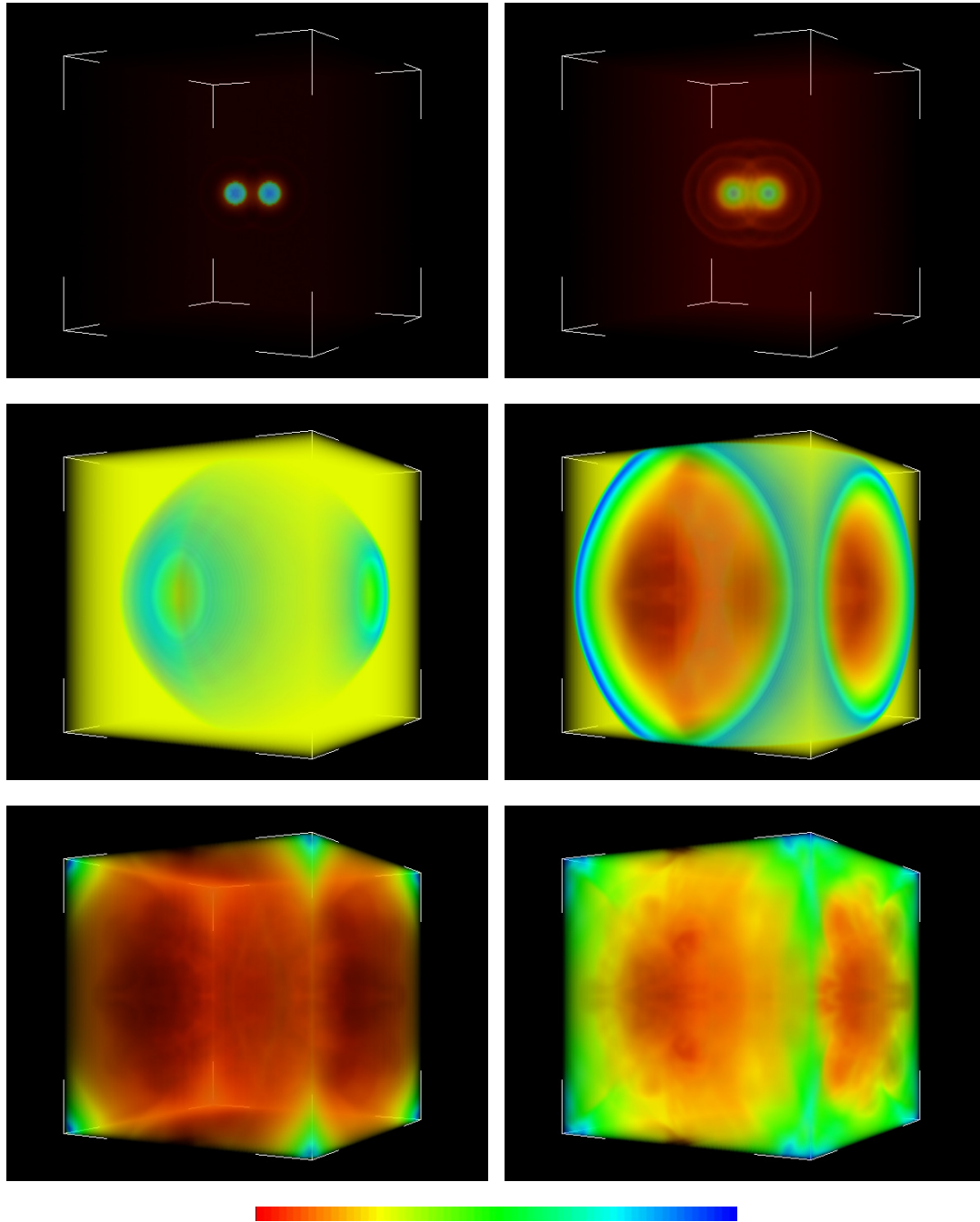


Figure 5.4: Volume rendering of the density of two colliding plumes in an ambient gas. The complete setup parameters is given in Table 5.1 (Sim. A). The time sequence is approximately at 5; 10; 20; 40; 80; 120 ns

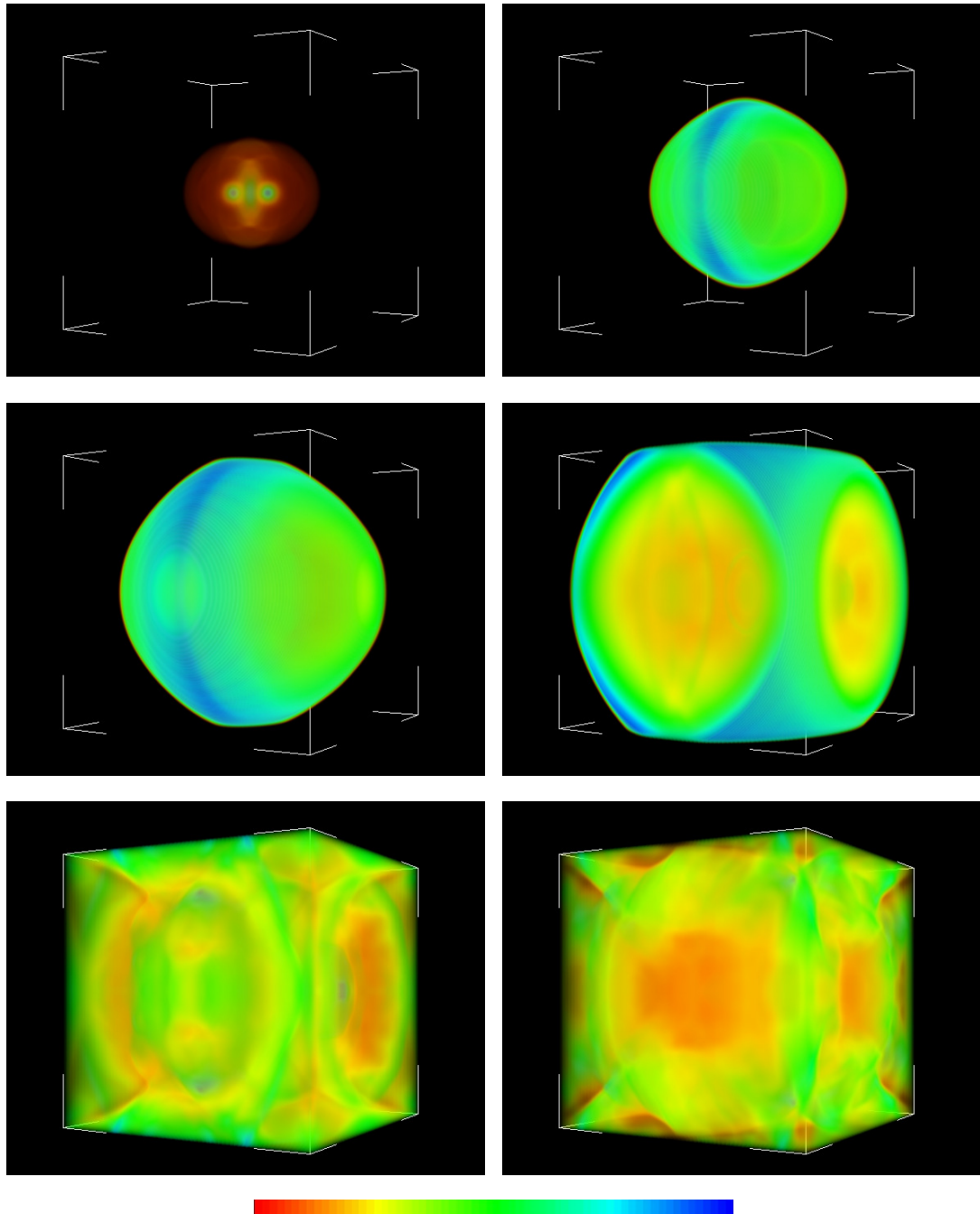


Figure 5.5: The volume rendering of the energy of two colliding plumes in an ambient gas. The complete setup parameters is the same as in Figure 5.4.

5. HYDRODYNAMICAL SIMULATION OF COLLIDING PLASMAS

The experimental setup of (Harilal et al., 2003) clearly shows that only in the high-background pressure regime it is possible to observe the characteristic "fingers" of the RT instability in the intensity measurements. On the contrary, no instability is observed in the low density regime. Our numerical simulations, instead, shows that the collision of two plumes produces a shock front at the collision with a lower density region inside.

The central, low density region has higher temperature and local speed which are greater than ones in the shock front, and thus generate the conditions for the RT instability to act. The main result is that, provided the dynamics of the colliding plumes fast enough, it is possible to produce the RT instability in *vacuum* in these conditions.

In (Harilal et al., 2003) case, the ICCD imaging of visible emission from laser-produced aluminum plasma at 1.3 Torr shows RT instability which develops in time interval of a thousand of nanoseconds. Our result of two colliding plumes in low background pressure shows that it is possible to take a time interval of about a hundred of nanoseconds for the RT instability to be fully developed. The snapshots of the instability patterns of two colliding plumes are presented in Figure 5.3. The complete set of the parameters are given in Table 5.1 (Simulation B).

The interacting plumes generate jet-like structure expansion, which could be seen in the earlier times. The volume rendering of density and energy in the colliding expansion of two symmetric plumes are given in Figure 5.4 and Figure 5.5, respectively. The initial setup parameters are given in Table 5.1 (Simulation A).

The collisions of two plumes in ideal gas show highly intense instability plasma-gas front configuration. A high energy peak in plasma happens in the collision region between the two plumes. The higher temperature in the center region of the colliding plumes leads to high energy, on the contrary, the density in the same region keeps low levels. Snapshots of energy and density at time $\sim 50ns$ of two colliding plumes are given in Figure 5.6 showing a predictable relation between the energy and the density in the RT instability region.

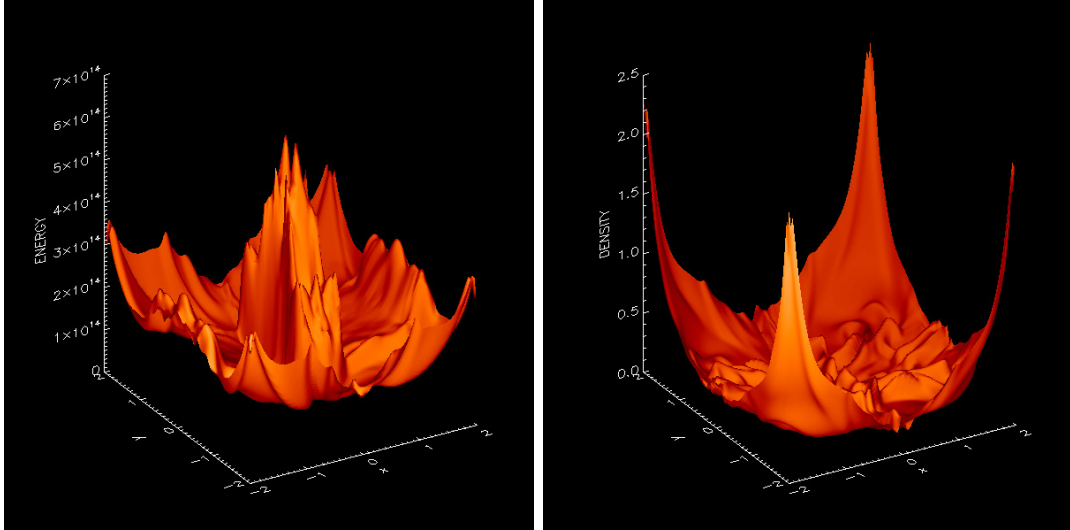


Figure 5.6: Volume representation of energy (left) and density (right) in xy -plane of two colliding plumes at time 50 ns. The full setup of parameters is given in Table 5.1 (Sim. B).

5.5 Conclusions

Hydrodynamical simulations of two colliding plumes in the stagnation limit show an onset of RT instability. In the case of a single plume interacting with low background pressure gas, the plume propagates freely following sedov similarity solution of blast wave expansion. In the case of two colliding plumes in the same physical situation, shock front is formed and the onset of Rayleigh-Taylor instability appears. The evolution time of the expansion of the two colliding plumes is about a hundred of nanoseconds, which is very fast in comparison with a single-plume propagation which takes about a thousand of nanoseconds in higher pressure gas. It would be interesting to have an experimental test of our numerical results.

5. HYDRODYNAMICAL SIMULATION OF COLLIDING PLASMAS

Chapter 6

Summary

In the present thesis a modern central WENO high-resolution method is introduced. It successfully resolves shock waves in hydrodynamics and relativistic hydrodynamics. The key idea is based on calculating the intermediate stages in Runge-Kutta predictor step in primitive variables. The inversion between conservative and primitive variables in relativistic hydrodynamics requires solving a nonlinear quartic equation of one of the primitive variables on the staggered grid. With the new idea implemented in the CRK schemes, the requirement for the mapping between the primitive and the conservative variables is not needed. This new approach we have named *conservative-primitive variables strategy (CPVS)*. Furthermore, the new approach is implemented in central framework (CRK schemes) which leads to numerical method for which a solution of a Riemann problem is not needed. In addition the diffusivity of the central schemes could be looked as an advantage in higher dimensions problem, where numerical dissipation is needed. The algorithm 2.7.1 gives a new idea integrated in the CRK schemes proposed by Pareschi et al. (2005). We presented the numerical benchmark tests of hydrodynamics and relativistic hydrodynamics with the fourth-order central Runge-Kutta scheme with conservative-primitive variables strategy integrated (CRK4-CPVS). All the results show excellent shock capturing and non-oscillatory solutions. Meanwhile, An operator splitting and CWENO concepts have been compared. The widely used astrophysical ideal MHD code ZEUS has been used as an example of the operator splitting approaches. ZEUS family of codes use operator splitting method for solving the equations, higher- order upwind methods for the advection terms, centered-differencing for the remaining terms and artificial viscosity for shock capturing. The

6. SUMMARY

shock tube numerical test revealed the advantage of the CWENO approach, namely, accurate shock-capturing and high-resolution treatment of the discontinuities by full conservative updates of the hydrodynamical variables. On the other hand, the numerical tests with ATHENA demonstrated spurious oscillation in the solution in the case of slow-moving shocks. Our CRK4-CPVS scheme shows oscillations-free solution in this case, which we consider as a high quality of our approach over the piecewise parabolic high-order Godunov algorithm implemented in ATHENA. In addition, the identical performance of both schemes in the case of two rarefaction waves, moving outward of the origin implies that CRK4-CPVS scheme would be the preferable choice for solving such problems because it is less expensive than the finite volume schemes and shows high accuracy and convergence speed.

The main objective of constructing CRK with a conservative-primitive variables strategy is to apply this new scheme to relativistic hydrodynamics. The reason for that is the fact that the relativistic shocks are very fast and sharp and thus are difficult to be captured by the operator splitting numerical algorithms and updating their solution by standard finite volume schemes it is necessary to solve a quartic nonlinear equation for one of the primitive variables. The CPVS strategy avoids the inversions between the conservative and the primitive variables in the Runge-Kutta steps and thus makes the approach cheap, fast and robust. Resolving the relativistic shock tube showed that our method is successfully applicable for capturing strong relativistic shocks. The Riemann-solver-free approach of the CRK-CPVS scheme is essential for the multidimensional problems of relativistic hydrodynamics since in the RHD the coupling between the normal and the transverse directions is conditioned by the presence of the Lorentz factor W . The transverse velocities are not constant through the shock and rarefaction waves in the relativistic one-dimensional Riemann problems (see Balsara (1994)). The standard multidimensional finite volume Godunov-type algorithms rely on the solution of one dimensional Riemann problems normal to each grid interface, which in the case of Euler equations is fully determined by the primitive variables - density, pressure and normal velocity. The transverse velocity is constant through all normal shock and rarefaction waves. The later is not valid in RHD. Therefore, one of the main advantages of CRK4-CPVS, Riemann-solver-free approach is a fundamental for relativistic hydrodynamics in multi dimensions. Our numerical test with CRK4-CPVS found consistent results with those in the literature. Moreover, because of the high resolution,

the CRK4-CPVS scheme provides an effective approach for numerical simulations of relativistic shock blast waves and relativistic nuclear collisions.

In the second part of the thesis we are concerned with the problem of nonlinear three-dimensional simulations of MHD instabilities. They are likely to arise in particular magnetic configurations and are subject to different evolution regimes. In the thesis are reviewed global 3D simulations of the Tayler instability in the presence of vertical fields. We showed that Tayler instability is triggered and when the azimuthal field is comparable to the imposed axial field. We used initial configuration in equilibrium by balancing the Lorentz force with the pressure gradient in the momentum equation. No stratification, no rotation and isothermal equation of state were considered. We used as a model cylindrical geometry with perfect conductor boundary conditions in the radial and vertical direction. The non linear evolution of the system leads to a stable equilibrium with a current free toroidal field. The final state is force free field, but this can be a consequence of the flux conservations imposed as boundary conditions. We plan to extend our investigations to the case of rotating magnetically supported jets, by including also the effect of a thermal equation of state.

Another group of three-dimensional simulations have been done in the field of plasma physics. Hydrodynamical simulations of two colliding plumes in the stagnation limit show that can trigger RT instability. A single plume interacting with low background pressure gas, i.e. the plume propagates freely following sedov similarity solution of blast wave expansion. In the case of two colliding plumes in the same physical situation, shock front is formed and onset of Rayleigh-Taylor instability can be seen. The evolution time of the expansion of two colliding plumes is about a hundred of nanoseconds, which is extremely fast in comparison with a single-plume propagation which takes about a thousand of nanoseconds in higher pressure gas. An experimental test of our numerical results with two colliding plumes would be interesting and important report on the plasma physics in the laboratory conditions.

In brief, a new promising CWENO-type approach has been developed which allows numerical resolving sharp discontinuities and very strong shocks. It was tested against one- dimensional relativistic shock tube problems. Two groups of three dimensional simulations of (M)HD instabilities were adopted with operator-splitting ideal MHD ZEUS-MP/2 code. The first results shows the conditions under which the Tayler instability is suppressed in dependance on the strength of poloidal field in coupled

6. SUMMARY

toroidal-poloidal magnetic configuration. The second group of simulation results shows the onset and its characteristics of Rayleigh-Taylor instability in collision between two plasma plumes.

CRK4-CPVS scheme is a reliable candidate for building a new CWENO-type modern astrophysical code in the future. Three-dimensional fully conservative CWENO code for investigating not only non linear MHD instabilities and shock phenomena in hydrodynamic or relativistic hydrodynamic limits but also phenomena of relativistic jets and supernovae seems to be a relevant outstanding topic in the current efforts in the computational astrophysics community.

References

- Abhilasha, P. S. R. Prasad, and R. K. Thareja. Laser-produced carbon plasma in an ambient gas. *Phys. Rev. E*, 48:2929–2933, October 1993. doi: 10.1103/PhysRevE.48.2929. 106
- M. Abramowitz and I. A. Stegun. *Handbook of Mathematical Functions*. New York: Dover, 1972. 68
- M. A. Aloy, J. M. Ibáñez, J. M. Martí, and E. Müller. GENESIS: A High-Resolution Code for Three-dimensional Relativistic Hydrodynamics. *ApJS*, 122:151–166, May 1999. doi: 10.1086/313214. 62
- N. Arnold, J. Gruber, and J. Heitz. Spherical expansion of the vapor plume into ambient gas: an analytical model. *Applied Physics A: Materials Science & Processing*, 69: 87–93, 1999. 101
- J. Bagchi, Gopal-Krishna, M. Krause, and S. Joshi. A Giant Radio Jet Ejected by an Ultramassive Black Hole in a Single-lobed Radio Galaxy. *ApJ*, 670:L85–L88, December 2007. doi: 10.1086/524220. 81
- D. S. Balsara. Divergence-Free Adaptive Mesh Refinement for Magnetohydrodynamics. *Journal of Computational Physics*, 174:614–648, December 2001. doi: 10.1006/jcph.2001.6917. 50
- Dinshaw S. Balsara. Riemann solver for relativistic hydrodynamics. *Journal of Computational Physics*, 114:284–297, 1994. 79, 114
- V. Y. Baranov, O. N. Derkach, V. G. Grishina, M. F. Kanevskii, and A. Y. Sebrant. Dynamics and stability of an expanding laser-induced plasma in a low-density gas. *Phys. Rev. E*, 48:1324–1330, August 1993. doi: 10.1103/PhysRevE.48.1324. 102

REFERENCES

- J. Bernstein, T. D. Lee, C. N. Yang, and H. Primakoff. Effect of the hyperfine splitting of a μ -mesonic atom on its lifetime. *Phys. Rev.*, 111(1):313–315, Jul 1958. doi: 10.1103/PhysRev.111.313. 84
- A. Bonanno and V. Urpin. Non-axisymmetric instability of axisymmetric magnetic fields. *A&A*, 488:1–7, September 2008. doi: 10.1051/0004-6361:200809435. 82, 84, 85, 86, 92
- T. V. Cawthorne, J. F. C. Wardle, D. H. Roberts, and D. C. Gabuzda. Milliarcsecond Polarization Structure of 24 Objects from the Pearson-Readhead Sample of Bright Extragalactic Radio Sources. II. Discussion. *ApJ*, 416:519–+, October 1993. doi: 10.1086/173254. 81
- K. R. Chen, J. N. Leboeuf, R. F. Wood, D. B. Geohegan, J. M. Donato, C. L. Liu, and A. A. Puretzky. Accelerated expansion of laser-ablated materials near a solid surface. *Phys. Rev. Lett.*, 75(25):4706–4709, Dec 1995. doi: 10.1103/PhysRevLett.75.4706. 101
- E. Choi and D. Ryu. Numerical relativistic hydrodynamics based on the total variation diminishing scheme. *New Astronomy*, 11:116–129, November 2005. doi: 10.1016/j.newast.2005.06.010. 62
- D. A. Clarke. On the Reliability of ZEUS-3D. *ApJS*, 187:119–134, March 2010. doi: 10.1088/0067-0049/187/1/119. 50
- P. Colella and P. R. Woodward. The Piecewise Parabolic Method (PPM) for Gas-Dynamical Simulations. *Journal of Computational Physics*, 54:174–201, September 1984. doi: 10.1016/0021-9991(84)90143-8. 62
- L. Del Zanna and N. Bucciantini. An efficient shock-capturing central-type scheme for multidimensional relativistic flows. I. Hydrodynamics. *A&A*, 390:1177–1186, August 2002. doi: 10.1051/0004-6361:20020776. 62
- A. Dolezal and S. S. M. Wong. Relativistic Hydrodynamics and Essentially Non-oscillatory Shock Capturing Schemes. *Journal of Computational Physics*, 120:266–277, September 1995. doi: 10.1006/jcph.1995.1164. 62, 70, 78

-
- R. Donat. A Flux-Split Algorithm Applied to Relativistic Flows. *Journal of Computational Physics*, 146:58–81, October 1998. doi: 10.1006/jcph.1998.5955. 62
- E. Godlewski and P.-A. Raviart. *Numerical Approximation of Hyperbolic Systems of Conservation Laws*. Springer, New York, 1996. 8
- B. Einfeldt, C.D. Munz, P.L. Roe, and B. Sjogreen. On godunov-type methods near low densities. *Journal of Computational Physics*, 92:273–295, 1991. 56
- D. Elstner, A. Bonanno, and G. Rüdiger. Nonlinear evolution of Tayler unstable equilibrium states. *Astronomische Nachrichten*, 329:717–721, 2008. doi: 10.1002/asna.200811029. 88
- S. A. E. G. Falle. Rarefaction Shocks, Shock Errors, and Low Order of Accuracy in ZEUS. *ApJ*, 577:L123–L126, October 2002. doi: 10.1086/344336. 50
- S. A. E. G. Falle and S. S. Komissarov. An upwind numerical scheme for relativistic hydrodynamics with a general equation of state. *MNRAS*, 278:586–602, January 1996. 62
- A. Ferrari. Modeling Extragalactic Jets. *ARA&A*, 36:539–598, 1998. doi: 10.1146/annurev.astro.36.1.539. 81
- J. A. Font. An introduction to relativistic hydrodynamics. *Journal of Physics Conference Series*, 91(1):012002–+, November 2007. doi: 10.1088/1742-6596/91/1/012002. 61
- K. O. Friedrichs and P. D. Lax. Systems of conservation equations with a convex extension. *Proc. Nat. Acad. Sci.*, 68:1686–1688, 1971. 10
- B. Fryxell, K. Olson, P. Ricker, F.X. Timmes, M. Zingale, D. Q. Lamb, P. MacNeice, R. Rosner, J.W. Truran, and H. Tufo. Flash: An adaptive mesh hydrodynamics code for modeling astrophysical thermonuclear flashes. *ApJS*, 131(203):273–334, 2000. 2, 49
- D. C. Gabuzda. The Magnetic Field Structures of Parsec-Scale Jets: Shocks Turbulence, and the Surrounding Medium. In M. Ostrowski & R. Schlickeiser, editor, *Plasma Turbulence and Energetic Particles in Astrophysics*, pages 301–310, December 1999. 81

REFERENCES

- D. C. Gabuzda, É. Murray, and P. Cronin. Helical magnetic fields associated with the relativistic jets of four BL Lac objects. *MNRAS*, 351:L89–L93, July 2004. doi: 10.1111/j.1365-2966.2004.08037.x. 81
- T. A. Gardiner and J. M. Stone. An unsplit Godunov method for ideal MHD via constrained transport. *Journal of Computational Physics*, 205:509–539, May 2005. doi: 10.1016/j.jcp.2004.11.016. 55
- T. A. Gardiner and J. M. Stone. An unsplit Godunov method for ideal MHD via constrained transport in three dimensions. *Journal of Computational Physics*, 227:4123–4141, April 2008. doi: 10.1016/j.jcp.2007.12.017. 55
- M. Gellert, G. Rüdiger, and D. Elstner. Helicity generation and α -effect by Tayler instability with z-dependent differential rotation. *A&A*, 479:L33–L36, February 2008. doi: 10.1051/0004-6361:20077781. 82
- S. S. Harilal, C. V. Bindhu, M. S. Tillack, F. Najmabadi, and A. C. Gaeris. Internal structure and expansion dynamics of laser ablation plumes into ambient gases. *Journal of Applied Physics*, 93:2380–2388, March 2003. doi: 10.1063/1.1544070. 102, 110
- A. Harten, B. Engquist, S. Osher, and S. Chakravarthy. Uniformly high order accurate essentially non-oscillatory schemes iii. *JCP*, 71:231–303, 1987. 9, 17
- Charles Hirsch. *Numerical computation of internal and external flows*, volume 2. John Wiley and Sons Ltd, 1998. 43, 47
- L. Howard and A. Gupta. On the hydrodynamic and hydromagnetic stability of swirling flows. *Journal of Fluid Mechanics*, 14(3):463–476, 1962. 82
- S. Ivanovski and A. Bonanno. Non-linear 3D simulations of current-driven instabilities in jets. *Nuclear Physics B Proceedings Supplements*, 190:88–93, May 2009. doi: 10.1016/j.nuclphysbps.2009.03.072. IV, 84
- S. L. Ivanovski, A. Bonanno, S. Tudisco, N. Gambino, and D. Mascali. Plasma astrophysics and laser experiments: hydrodynamical simulation of colliding plasmas. *Radiation Effects and Defects in Solids*, 165(6):457–462, 2010. IV, 104

REFERENCES

- G.-S. Jiang and C.-W. Shu. Efficient implementation of weighted eno schemes. *JCP*, 126:pp.202–228, 1996. 10, 22, 25
- G. S. Jiang, D. Levy, C. T. Lin, S. Osher, and E. Tadmor. High-resolution nonoscillatory central schemes with nonstaggered grids for hyperbolic conservation laws. *SIAM J. Numer. Anal.*, 35:pp.2147–2168, 1998. 10
- P. Kharb, D. Gabuzda, and P. Shastri. Parsec-scale magnetic field structures in HEAO-1 BL Lacs. *MNRAS*, 384:230–250, February 2008. doi: 10.1111/j.1365-2966.2007.12690.x. 81
- E. Knobloch. On the stability of magnetized accretion discs. *MNRAS*, 255:25P–28P, April 1992. 82
- A. Kurganov and E. Tadmor. New high-resolution central schemes for nonlinear conservation laws and convection-diffusion equations. *Journal of Computational Physics*, 160:214–282, 2000. 10
- P. Lax and B. Wendroff. Systems of conservation laws. *Comm. Pure Appl. Math.*, 13:217–237, 1960. 7
- P. D. Lax. Weak solutions of nonlinear hyperbolic equations and their numerical computation. *Comm. Pure Appl. Math.*, 7:159–193, 1954. 33
- K. J. Leppanen, J. A. Zensus, and P. J. Diamond. Linear Polarization Imaging with Very Long Baseline Interferometry at High Frequencies. *AJ*, 110:2479–+, November 1995. doi: 10.1086/117706. 81
- T. Lery, H. Baty, and S. Appl. Current-driven instabilities in astrophysical jets. Non linear development. *A&A*, 355:1201–1208, March 2000. 82
- R. J. LeVeque. *Numerical Methods for Conservation Laws*. Lecture in Mathematics, Birkhauser Verlag, Basel, 1992. 8
- R. J. LeVeque. *Finite Volume Methods for Hyperbolic Problems*. Cambridge University Press, 2002. 55

REFERENCES

- D. Levy, G. Puppo, and G. Russo. Central weno schemes for hyperbolic systems of conservation laws. *Mathematical Modeling and Numerical analysis*, 33(3):547–571, 1999. 6, 11, 12, 20, 21, 24, 25, 26, 29, 30, 34, 37, 59
- X.-D. Liu, S. Osher, and T. Chan. Weighted essentially non-oscillatory schemes. *JCP*, 115:200–212, 1994. 9
- P. -Y. Longaretti. Pressure-Driven Instabilities in Astrophysical Jets. In S. Massaglia, G. Bodo, A. Mignone, & P. Rossi, editor, *Jets From Young Stars III*, volume 754 of *Lecture Notes in Physics, Berlin Springer Verlag*, pages 131–151, 2008. doi: 10.1007/978-3-540-76967-5_4. 87
- J. Martí and E. Müller. Extension of the Piecewise Parabolic Method to One-Dimensional Relativistic Hydrodynamics. *Journal of Computational Physics*, 123: 1–14, January 1996. doi: 10.1006/jcph.1996.0001. 62, 67, 70
- J. M. Martí and E. Müller. Numerical Hydrodynamics in Special Relativity. *Living Reviews in Relativity*, 6:7–+, December 2003. 61, 62, 78
- D. Mascali, S. Tudisco, A. Bonanno, N. Gambino, S. Ivanovski, A. Anzalone, S. Gammino, R. Miracoli, and F. Musumeci. Colliding laser-produced plasmas: a new tool for nuclear astrophysics studies. *Radiation Effects and Defects in Solids*, 165(6): 730–736, 2010. 104
- P. Mészáros. Theories of Gamma-Ray Bursts. *ARA&A*, 40:137–169, 2002. doi: 10.1146/annurev.astro.40.060401.093821. 61
- A. Mignone and G. Bodo. An HLLC Riemann solver for relativistic flows - I. Hydrodynamics. *MNRAS*, 364:126–136, November 2005. doi: 10.1111/j.1365-2966.2005.09546.x. 62
- A. Mignone, T. Plewa, and G. Bodo. The Piecewise Parabolic Method for Multidimensional Relativistic Fluid Dynamics. *ApJS*, 160:199–219, September 2005. doi: 10.1086/430905. 62
- A. Mignone, G. Bodo, S. Massaglia, T. Matsakos O. Tesileanu and C. Zanni, and A. Ferrari. Pluto: A numerical code for computational astrophysics. *The Astrophysical Journal Supplement Series*, 170(1):228–242, May 2007. 2, 49

REFERENCES

- I. F. Mirabel and L. F. Rodríguez. Sources of Relativistic Jets in the Galaxy. *ARA&A*, 37:409–443, 1999. doi: 10.1146/annurev.astro.37.1.409. 61
- P. Mora. Plasma expansion into a vacuum. *Phys. Rev. Lett.*, 90(18):185002, May 2003. doi: 10.1103/PhysRevLett.90.185002. 101
- H. Nessyahu and E. Tadmor. Non-oscillatory central differencing for hyperbolic conservation laws. *Journal of Computational Physics*, 87(2):408–463, 1990. 10
- M. L. Norman and K.-H. Winkler. Astrophysical radiation hydrodynamics. *Winkler, K.-H. and Norman, M.L., Editors, Astrophysical Radiation Hydrodynamics, Reidel, Dordrecht*, page 187, 1986. 62
- L. Pareschi, G. Puppo, and G. Russo. Central runge-kutta schemes for conservation laws. *SIAM J. Sci. Comput.*, 26(3):979–999, 2005. III, 6, 11, 18, 19, 21, 24, 27, 28, 29, 30, 31, 34, 39, 40, 59, 113
- Kenneth G. Powell, Philip L. Roe, Timur J. Linde, Tamas I. Gombosi, and Darren L. De Zeeuw. A solution-adaptive upwind scheme for ideal magnetohydrodynamics. *Journal of Computational Physics*, 154(2):284–309, September 1999. 2, 49
- K. H. Prendergast. The Equilibrium of a Self-Gravitating Incompressible Fluid Sphere with a Magnetic Field. I. *ApJ*, 123:498–+, May 1956. doi: 10.1086/146186. 86
- Jianxian Qui and Chi-Wang Shu. On the construction, comparison, and local characteristic decomposition for high-order central weno schemes. *Journal of Computational Physics*, 183:187–209, 2002. 34
- T. Rahman and R. B. Moore. A New Multidimensional Relativistic Hydrodynamics code based on Semidiscrete Central and WENO schemes. *ArXiv Astrophysics e-prints*, December 2005. 62
- G. Rüdiger, R. Hollerbach, M. Schultz, and D. Elstner. Destabilization of hydrodynamically stable rotation laws by azimuthal magnetic fields. *MNRAS*, 377:1481–1487, June 2007. doi: 10.1111/j.1365-2966.2007.11682.x. 82
- P. T. Rumsby, J. W. M. Paul, and M. M. Masoud. Interactions between two colliding laser produced plasmas. *Plasma Physics*, 16:969–975, October 1974. doi: 10.1088/0032-1028/16/10/009. 103

REFERENCES

- Giovanni Russo. High order shock capturing schemes for balance laws. 2008. 8
- D. Ryu, I. Chattopadhyay, and E. Choi. Equation of State in Numerical Relativistic Hydrodynamics. *ApJS*, 166:410–420, September 2006. doi: 10.1086/505937. 68
- R. Sanders and A. Weiser. A high resolution staggered mesh approach for nonlinear hyperbolic systems of conservation laws. *Journal of Computational Physics*, 10101 (314-329), 1992. 10
- V. Schneider, U. Katscher, D. H. Rischke, B. Waldhauser, J. A. Maruhn, and C.-D. Munz. New Algorithms for Ultra-relativistic Numerical Hydrodynamics. *Journal of Computational Physics*, 105:92–107, March 1993. 68
- A. K. Sharma and R.K. Thareja. Plume dynamics of laser-produced aluminum plasma in ambient nitrogen. *Applied Surface Science*, 243(1-4):68–75, April 2005. 101
- A. K. Sharma and R.K. Thareja. Anisotropic emission in laser-produced aluminum plasma in ambient nitrogen. *Applied Surface Science*, 253(6):3113–3121, 2007. 102
- J. Shi, C. Hu, and C.-W. Shu. A technique of treating negative weights in weno schemes. *Journal of Computational Physics*, 175:108–127, 2002. 24
- C.-W. Shu. Essentially non-oscillatory and weighted essentially non-oscillatory schemes for hyperbolic conservation laws. *Lecture Notes in Mathematics, Springer, Advanced Numerical Approximation of Nonlinear Hyperbolic Equations*, 1998. 9, 14
- L. Di G. Sigalotti, H. Lopez, A. Donoso, E. Sira, and J. Klapp. A shock-capturing sph scheme based on adaptive kernel estimation. *Journal of Computational Physics*, (212):124–149, 2006. 56
- G. Sod. A survey of several finite difference methods for systems of nonlinear hyperbolic conservation laws. *Journal of Computational Physics*, 22:1–31, 1978. 33
- I. V. Sokolov, H.-M. Zhang, and J. I. Sakai. Simple and Efficient Godunov Scheme for Computational Relativistic Gas Dynamics. *Journal of Computational Physics*, 172: 209–234, September 2001. doi: 10.1006/jcph.2001.6821. 62

REFERENCES

- J. M. Stone and M. L. Norman. ZEUS-2D: A radiation magnetohydrodynamics code for astrophysical flows in two space dimensions. I - The hydrodynamic algorithms and tests. *ApJS*, 80:753–790, June 1992a. doi: 10.1086/191680. 2, 49, 53
- J. M. Stone and M. L. Norman. ZEUS-2D: A Radiation Magnetohydrodynamics Code for Astrophysical Flows in Two Space Dimensions. II. The Magnetohydrodynamic Algorithms and Tests. *ApJS*, 80:791–+, June 1992b. doi: 10.1086/191681. 49
- J. M. Stone and M. L. Norman, 1992. URL <http://lca.ucsd.edu/portal/codes/zeusmp2>. IV, 2, 13, 49, 105
- J. M. Stone, D. Mihalas, and M. L. Norman. ZEUS-2D: A radiation magnetohydrodynamics code for astrophysical flows in two space dimensions. III - The radiation hydrodynamic algorithms and tests. *ApJS*, 80:819–845, June 1992. doi: 10.1086/191682. 49
- J. M. Stone, T. A. Gardiner, P. Teuben, J. F. Hawley, and J. B. Simon. Athena: A new code for astrophysical mhd. *The Astrophysical Journal Supplement Series*, 178(1):137–177, September 2008. IV, 2, 13, 49, 55
- H. Strehlow. Shock waves in laser-pulse-irradiated metals. *Applied Physics A: Materials Science & Processing*, 72:45–52, March 2001. 101
- E. Tadmor. Approximate solutions of nonlinear conservation laws. *CIME Lecture notes*, UCLA CAM Report(97-51), 1997. 8, 40
- E. J. Tasker, R. Brunino, N. L. Mitchell, D. Michielsen, S. Hopton, F. R. Pearce, G. L. Bryan, and T. Theuns. A test suite for quantitative comparison of hydrodynamic codes in astrophysics. *MNRAS*, 390:1267–1281, November 2008. doi: 10.1111/j.1365-2966.2008.13836.x. 50
- R. J. Tayler. Hydromagnetic Instabilities of an Ideally Conducting Fluid. *Proceedings of the Physical Society B*, 70:31–48, January 1957. doi: 10.1088/0370-1301/70/1/306. 85
- R. J. Tayler. The adiabatic stability of stars containing magnetic fields-I. Toroidal fields. *MNRAS*, 161:365–+, 1973. 82, 84

REFERENCES

- R. J. Tayler. The adiabatic stability of stars containing magnetic fields. IV - Mixed poloidal and toroidal fields. *MNRAS*, 191:151–163, April 1980. 86
- A. Tchekhovskoy, J. C. McKinney, and R. Narayan. WHAM: a WENO-based general relativistic numerical scheme - I. Hydrodynamics. *MNRAS*, 379:469–497, August 2007. doi: 10.1111/j.1365-2966.2007.11876.x. 61, 78
- Gabor Toth. General code for modeling mhd flows on parallel computers: Versatile advection code. *Astrophysical Letters and Communications*, 34:245–250, 1996. 2, 49
- P. L. G. Ventzek, R. M. Gilgenbach, C. H. Ching, and R. A. Lindley. Schlieren and dye laser resonance absorption photographic investigations of KrF excimer laser-ablated atoms and molecules from polyimide, polyethyleneterephthalate, and aluminum. *Journal of Applied Physics*, 72:1696–1706, September 1992. doi: 10.1063/1.351693. 101
- J. von Neumann and R. D. Richtmyer. A method for the numerical calculation of hydrodynamic shocks. *J. Appl. Phys.*, 21:232–237, 1950. 50, 51
- J. R. Wilson and G. J. Mathews. *Relativistic Numerical Hydrodynamics*. December 2003. 62
- J.R. Wilson. Numerical study of fluid flow in akerr space. *Astropysical Journal*, 173: 431–438, 04 1972. 62
- K. H. Wong, T. Y. Tou, and K. S. Low. Pulsed CO₂ laser ablation of graphite and polymers. *Journal of Applied Physics*, 83:2286–2290, February 1998. doi: 10.1063/1.366970. 101
- J. A. Zensus. Parsec-Scale Jets in Extragalactic Radio Sources. *ARA&A*, 35:607–636, 1997. doi: 10.1146/annurev.astro.35.1.607. 61
- U. Ziegler. A central-constrained transport scheme for ideal magnetohydrodynamics. *Journal of Computational Physics*, 196(2):393–416, May 2004. 2, 49